Mathematical Modeling and Analysis of *in vitro* Actin Filament Dynamics and Cell Blebbing

A DISSERTATION

SUBMITTED TO THE FACULTY OF THE GRADUATE SCHOOL

OF THE UNIVERSITY OF MINNESOTA

BY

Jifeng Hu

IN PARTIAL FULFILLMENT OF THE REQUIREMENTS

FOR THE DEGREE OF

DOCTOR OF PHILOSOPHY

Dr. Hans G. Othmer, Advisers

December, 2009

Acknowledgements

I would like to express sincere thanks and gratitude to my thesis adviser Hans G. Othmer for the encouragement and guidance through these years of my PhD study. I would like to thank Tasos Matzavinos for his valuable discussion and help on the numerical simulations. I would like to thank all the members of Hans Othmer's group for their comments and support.

Dedication

Dedicated to my wife and my parents.

Abstract

The dynamics of the actin cytoskeleton are vital for cell motility observed in many biological processes, such as morphogenetic movements during embryotic development, fibroblast migration during wound healing, and chemotactic movements of immune cells. To fulfill specific tasks, motile cells manipulate various actin structures within regions such as the lamellipodium, filopodia and stress fibers. A large pool of regulatory proteins and motor molecules coordinate the dynamic change of these structures to generate mechanical forces.

In this thesis, we first investigate the temporal evolution of filament length distribution in a deterministic approach. The change of filament lengths is described by ordinary differential equations, and effects of diverse regulatory mechanisms are explored. We predict that the endwise polymerization alone produces a long-lived Gaussian-like distribution of filament lengths, which eventually evolves to an exponential distribution. The introduction of fragmentation drastically leads to a Bessel-type equilibrium distribution. Our model confirms that profilin proteins slow filament growth, decreases the extent of polymerization, and promote filament treadmilling. Actin monomers are associated with nucleotide ATP. In a filament, ATP can hydrolyze randomly into ADP-Pi, and subsequently release the phoshpate becoming ADP. Random ATP hydrolysis complicates the filament dynamics. The effect is analyzed in a stochastic model where each subunit within a filament is distinguished by associated nucleotide types. We theoretically predict a large length fluctuation occurring around the critical concentration of ATP-actin where the filament tip is bound intermittently by nucleotides ADP and ATP. By implementing an efficient stochastic simulation algorithm, we are able to track the evolution of

length and nucleotide profile of single filament.

We also investigate the phenomenon of cell blebbing, a typical membrane protrusion driven by actin dynamics and acto-myosin contraction. The major components of blebbing cells are recognized, and models for each component and their interaction are individually considered. Our analysis shows that a simple constraint on the membrane expansion rate relates the dynamic bleb size with the ring constricting the bleb. The properties of equilibrium state of blebbing are probed in a mechanical model whereby a uniform hydrostatic pressure is established by the balance of membrane tension in the contracting and expanding cell domains. We recognize that a potential membrane flow is important in establishing the blebbing equilibrium, and the influence of various flow types is compared.

Contents

List of Tables

List of Figures

Chapter 1

Introduction

1.1 Outline of the thesis

This thesis consists of four parts. The first part is Chapter 1, and includes the biological background and literature reviews on actin filament dynamics. The second part deals mainly with actin dynamics using a deterministic approach . In Chapter 2, the basic nucleation-elongation model of filament polymerization is formulated and analyzed. The effect of fragmentation imposed on the basic model is probed in Chapter 3. In Chapter 4, the profilin interaction with actin monomers and filaments are modelled. Variants of this model are compared by varying the parameters. The third part focuses on the features of actin filaments in the light of a stochastic model by differentiating each subunit by its bound nucleotide type. In Chapter 5, the pure actin dynamics and the dynamics of filament polymerization with profilin based on the stochastic model are analyzed. In Chapter 6, the length changes of filaments are investigated in the single filament method. The large length fluctuation are predicted for a filament intermittently capped by ADP and ATP. In Chapter 7 of the last part, we present preliminary results for a mechanical model of the actin-driven cell blebbing. In Chapter 8, we point out the future work on the actin dynamics and actin-related cell motility.

1.2 Biological background

1.2.1 Cell motility

1.2.1.1 Cell biology and cell motility

The discovery of biological cells is one of the greatest in human history. In 1655, an English scientist made an observation that would change basic biological theory and research forever. While examining a dried piece of cork tree under his crude light microscope, Robert Hooke discovered many tiny compartments in it, and gave them the name—cell. It is from then on that cell theory was vastly developed in scope and depth. Knowledge of the cell has grown explosively, especially with the aid of advanced microscopic imaging and labelling techniques in the last century.

Despite the progress made toward the understanding of cells, many interesting phenomena about cells are not understood yet. Cell motility is among these of interest to many scientists from diverse areas. The ability to move is a fundamental characteristic of living cells, and their movement is critical for many biological processes, including morphogenetic movements during embryonic development, fibroblast migration during wound healing, and chemotactic movements of immune cells. For example, during the early stages of cancers, cancerous cells grow explosively at the primary site of tumor growth. With uncontrolled growth, cancer cells rapidly consume and eventually exhaust the oxygen and nutrition in the infected tissues. They then develop a vascular system and eventually spread to new sites, which is mortal to the host body. This migration and spread of cancerous cells is known as metastasis, and this entire process is highly dependent on cell movement. A complete understanding of cell motility is desired not only for the satisfaction of our curiosity about the cell nature, but also for the practical benefit of exploring new treatments to many diseases.

1.2.1.2 Characteristics of actin-driven cell movement

In vivo cells exhibit a variety of locomotion patterns, manifesting diverse underlying mechanisms. *Paramecium*, a unicellular ciliate protozoa, propels itself through its aquatic habitat by beating multiple rows of cilia at its surface in a synchronized way, whereas a sperm cell exhibits a wavelike locomotion by the beating of its flagellum [1].

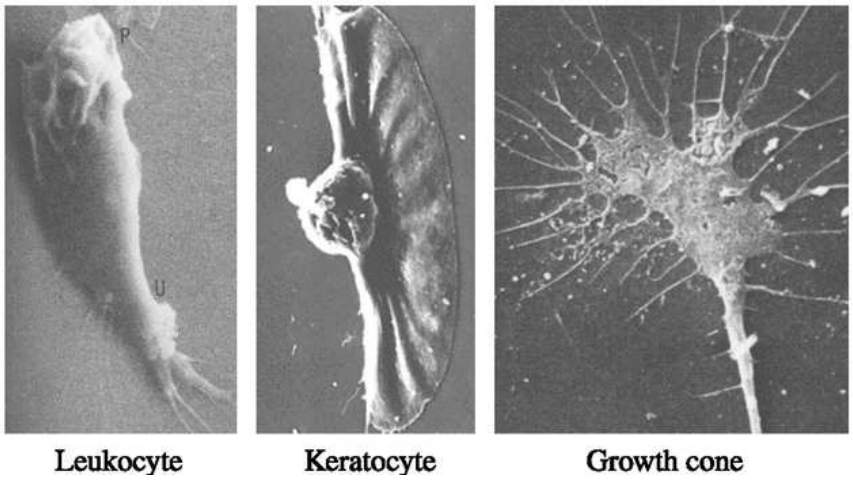

Figure 1.1: Actin-driven movement of different types of cells (from [2]).

Another common mechanism is to apply the machinery of rapid polymerization of a filamentous structure. In cells, the structure grows when the monomeric form of the proteins are continuously supplied to the filament ends. The elongating filaments in a confined cellular space then push against the cell membrane and drive the translocation of the whole body. This mechanism is responsible for movement in most migrating cells. Many eukaryotic cells translocate by extending pseudopodia as shown in Figure 1.1. Depending on their morphology and cellular context, the pseudopodia are often called lamellipodia, filopodia, or ruffles as depicted in Figure 1.2. It is also found that some intracellular bacteria, such as *Listeria*, can propel themselves within and between eukaryotic cells by hijacking the motility machinery in host cells. In particular, they recruit the actin monomers from the host cell to their cell surface, form an actin comet tail, and push themselves forward by the continuous growth of the tail. Some viruses,

endogenous vesicles and endosomes employ this machinery for intracellular motility as well.

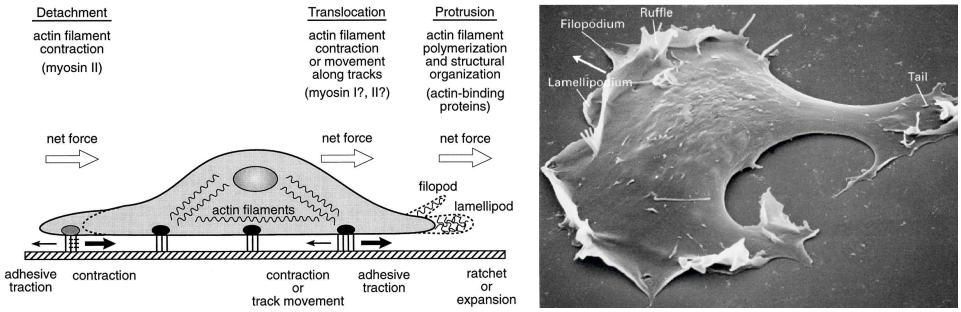

Figure 1.2: A schematic of the major steps featured in the migration of eukaryotic cells (left, from [3]), and an electron microscopy of the leading edge of a human fibroblast moving toward the upper left corner (right, by Julian Heath, MRC Cell Biophysics Unit, Kings College, London).

Among the diverse cell types, *Dictyostelium discoidium* (*Dd*) and neutrophils are widely-used model systems for studying signal transduction, chemotaxis, and actin-based cellular motility. *Dd* motility exhibits many characteristics of eukaryotic cell locomotion. The latter can be characterized by four different stages: protrusion of the leading edge, attachment to the substrate, translocation of the cell body, and final detachment of the rear and adhesion. A schematic of these four major steps as shown in Figure 1.2 can be described as follows:

1. Localized protrusions are first extended at the leading edge. The surface receptor proteins integrate the signals from the extracellular stimuli, and subsequently transduce the information downstream to the effectors, which induces the assembly and disassembly of the filamentous structures.

2. Then adhesive complexes are expressed to anchor the cells onto the substrate. The formation of these adhesive complexes not only stabilize the protrusions formed in Step 1, but also serve as sites for molecular signaling, and transmit mechanical force to the substrate.

3. Next, in fibroblast cells acto-myosin filaments contract at the front of the cell and pull the

cell body toward the protrusion, whereas in *Dd* contraction is at the rear and the cytoplasm is squeezed forward.

4. Finally, cells detach the adhesive contacts at the rear, allowing the tail of the cell to follow the cell body.

1.2.1.3 Signaling and dynamics of actin cytoskeleton assembly

The leading edge of migrating cells contains a highly dynamic actin network. Electron microscopy of the leading edge unveils a dense network composed of highly cross-linked actin filaments. A careful examination reveals a remarkable degree of order in the dense structure as displayed in Figure 1.3. The filament network is especially dense near the inner surface of the membrane, and the actin filaments are connected in a highly cross-linked, branching arbor with short filaments growing from the side of the longer filaments. Most filaments grow toward the membrane, whereas the ones growing away from the membrane get capped.

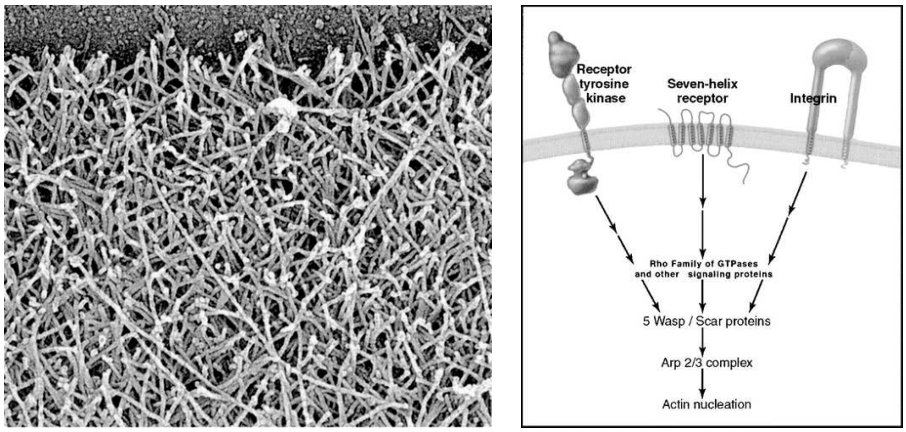

Figure 1.3: The electron micrograph of the dense actin network (left), and signal transduction at the leading edge of migrating cells (right) [4].

In the last three decades, people learned much about the molecular mechanism for the assembly of actin filament networks at the leading edge. The external stimuli, acting through receptors and multiple signal transduction pathways, several of which converge on members of the WASP/Scar family of proteins, dictate the assembly of the actin filament network in the

cell cortex, the region immediately interior to the cell membrane, as seen in Figure 1.3. The molecular pathway from receptors to WASP/Scar has not been completely mapped, and biologists postulate that WASP/Scar proteins integrate diverse signals, including those carried by the Rho family GTPase, Rac and Cdc42 signalling molecules. Downstream, active WASP/Scar stimulate actin filament nucleation by Arp2/3 complexes. The first family member discovered, WASP, is named for Wiskott-Aldrich syndrome, a fatal immune disease in humans that results from mutations in the gene encoding WASP. Every eukaryotic cell examined contains one or more WASP/Scar proteins. They consist of multiple domains that interact with signal molecules, actin monomers and the Arp2/3 complex. Thus WASP/Scar proteins act as intermediate coordinators in signal transduction between external stimuli and intracellular actin assembly. Some non-eukaryotic cells, however, produce their own activators of Arp2/3 proteins, such as ActA in *Listeria* and Fungi Myosins I in yeast.

Identifying a nucleator of actin filaments has been a long search until the discovery of the Arp2/3 complex [4]. The latter is an essential component responsible for the formation of the cross-linked actin network. This complex is a stable assembly of seven highly conserved polypeptides. In addition to five unique polypeptides, it contains the actin-related subunits, Arp2 and Arp3. When Arp2/3 are activated, these two subunits can attach one actin monomer and form a trimer. In turn, the activation of Arp2/3 can be greatly stimulated by direct interaction with proteins of the WASP/Scar family.

An influential model that illustrates how the actin network evolves at the leading edge is the so-called *dendritic nucleation treadmilling model* [4] as illustrated in Figure 1.4. The model proposes that, in the absence of extracellular stimuli, cytoskeleton components are held in a metastable state when the free barbed ends are unavailable (step 1). In the presence of stimuli, the signal is transduced downstream through a complicate pathway (step 2), and activates the WASP/Scar family proteins (step 3), which in turn trigger the activation of the Arp2/3 complex to generate new barbed ends (step 4). The nucleated filaments anchor at the side of pre-existing ones and grow rapidly in a large pool of polymerizable subunits (step 5) and push the membrane forward (step 6). However, the growth of the barbed ends is soon terminated by capping proteins

(step 7). Simultaneously, intrinsic ATP hydrolysis within actin filaments and subsequent Pi release (step 8) triggers severing and depolymerization of older filaments by ADF/cofilins (step 9). Nucleotide exchange catalyzed by profilin (step 10) recycles ADP-actin subunits back to the ATP-actin monomer pool. This network-treadmilling process establishes the growth of the network just beneath the cell membrane that generates the mechanical force required for the formation and advance of the lamellipodium.

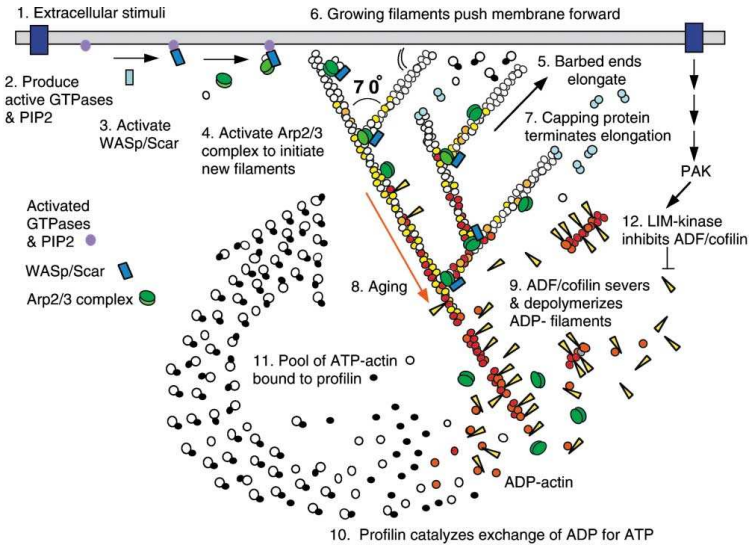

Figure 1.4: A dendritic nucleation treadmilling model of actin filament network [4].

1.2.2 Biochemistry of actin and actin-binding proteins

1.2.2.1 Molecular structure of actin proteins

Actin proteins were first isolated by Straub (1942) as part of the acto-myosin complex from the skeletal muscle. It is one of the most abundant proteins in a cell, and is present in species from yeast to mammals. Actin is also highly conserved in amino acid sequence in species ranging from primitive unicellular organisms to plants and animals. Human skeletal muscle actin is identical in sequence to muscle actin in mice, rabbits, rats, chickens, and cattle. There are totally six copies of genes coding for actin proteins and they vary only in a small number of

residues.

Actin is a single peptide chain of 375 amino acids with a molecular mass of 43 kDa. Monomeric actin (G-actin) typically exists in an asymmetric globular structure with a large and small domain, each in turn containing two subdomains. These subdomains provide potential binding-sites for various actin-associated proteins as will be discussed later. The adenosine triphosphate (ATP) and diphosphate nucleotides (ADP), together with cations Mg^{2+} and Ca^{2+}, can bind at a cleft between the two subdomains.

G-actin can self-organize into a two-stranded helical filament as depicted in Figure 1.5. The asymmetric nature of the monomeric actin subunit itself creates the basis for the helical nature and structural polarity of a single polymeric actin filament. The polarity of actin filaments may be visualized by decorating the filaments with heavy meromyosin. G-actin is measured to be 7 nm in diameter and 5.4 nm long. Each actin subunit contributes an average of 2.7 nm increment to the total length of filaments. Thus a filament of 1 μm long consists of about 370 monomers.

1.2.2.2 Spontaneous filament nucleation

Under normal physiological conditions, actin monomers in a pure solution spontaneously form filament seeds of short length. However, the nucleation step is highly unfavorable energetically, and a large monomer pool is required for the formation of few filaments. *In vivo*, nucleation factor proteins are required to facilitate the filament formation at specific locations. These include Arp2/3 complex, formin family proteins, gelsolin and spectrin proteins. Experimental data shows that the spontaneous nucleation rate is proportional to the third or fourth power of the G-actin concentrations, suggesting that actin seeds are composed of $3-4$ monomers. Molecular dynamics simulations [5] identified actin trimers as the critical nuclei or seeds. However, the kinetic rate constants for dimer and trimer formation cannot be obtained directly due to the extreme instability of these entities. They are only derived from kinetic simulations, which reproduce the correct time course of polymerization over a limited range of actin monomer concentrations as in experiments.

1.2.2.3 Endwise polymerization and depolymerization

In a suitable physiological environment, G-actin binds reversibly onto both ends of actin filament. The kinetics differ remarkably at both ends due to the structural polarity of the filament. In particular, the dynamics of polymerization at one end, namely the barbed or plus end, is faster than at the other end, often called the pointed or minus end.

At each end, the addition and deletion of action monomers can be represented as follows

$$\mathcal{A}_1 + \mathcal{A}_{n-1} \quad \underset{k^-}{\overset{k^+}{\rightleftarrows}} \quad \mathcal{A}_n$$

where A_n is the filament with n subunits. Polymer theory shows that the filament will elongate at a rate of [6]

$$d\mathrm{n}/dt = k^+c - k^- \tag{1.1}$$

where c stands for the actin monomer concentration. At each end of the filament, there exists a critical concentration, $c_{crit} = k^-/k^+$, such that the monomer addition is balanced by its detachment. Without energy input, a perfect filament would have the same c_{crit} for both ends. At thermodynamic equilibrium, the filament exhibits no net elongation at either end. However, F-actin is a well-known ATPase. The nucleotide ATP hydrolyzes shortly after polymerization and subsequently release its γ-phosphate. The free energy derived from ATP hydrolysis is coupled to the filament polymerization. The ATP-associated actin monomer (G-ATP) has a much higher on-rate at the plus end than at the minus end, and therefore the critical concentration c_+ is lower than the critical concentration c_- for the minus end. The equilibrium constants are the same at both ends for ADP-associated actin monomer (G-ADP), and hence the critical concentrations are the same. Since G-ATP is the dominant form of the monomer *in vivo*, its kinetics dominate the growth or decay of the filament. Between the critical concentrations of both ends there is a unique monomer concentration, at which the polymerization at the barbed end is balanced by the depolymerization of the pointed end as shown in Figure 1.6. At this concentration the filament is undergoing a dynamic process called treadmilling, whereby a filament with a constant length grows at the plus end and shrinks at the minus end.

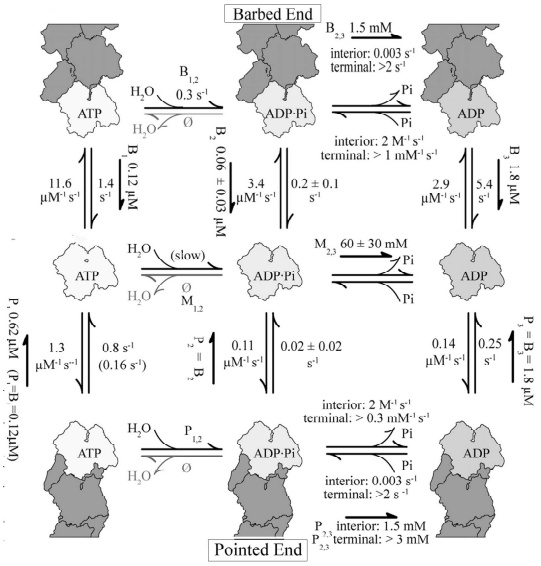

Figure 1.5: The kinetic rate constants of actin monomers associated with the ADP-, ADP-Pi- and ATP-nucleotide at both ends [8].

The differential actin states depending on the associated nucleotides are important for actin dynamics. A complete set of nucleotide-involved polymerization reactions and the rate constants at both filament ends are exemplified in Figure 1.5. The ATP hydrolysis provides the polymerization cycle with free energy input, and powers the filament treadmilling. For a treadmilling filament, G-ATP polymerizes at the barbed end, and subsequently hydrolyzes the ATP to ADP-Pi, which eventually release its weakly attached phosphate when it treadmills towards the pointed end. ADP-actin then detaches from the pointed end. The hydrolyzed monomers is refreshed in the solution by nucleotide exchanges. However, nucleotide exchange is prohibited for F-actin. The varying nucleotide types also creates structural basis for the binding of a variety of regulatory proteins.

1.2.2.4 Actin binding proteins

Motile cells require fine control of changes in actin filament structures in response to the external stimuli. *In vivo*, it is fulfilled by the concerted regulation of a large number of actin-binding

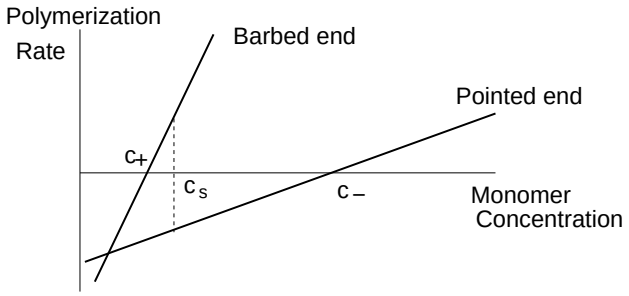

Figure 1.6: The filament polymerization at the barbed end and pointed end. The critical concentrations at the two ends are c_+ and c_-, respectively. The treadmilling concentration c_s lies between the two critical concentrations.

proteins (ABPs) as exemplified in Figure 1.7. Biomimetic experiments revealed that a minimal set of five proteins are sufficient to reconstitute sustained movement of *Listeria* and *Shigella* or persistent propulsion of polystyrene microspheres in actin solutions [9, 10, 11]. The required protein agents include filament nucleator, capping proteins and actin depolymerization factors. At present, more than 60 families of ABPs have been discovered [4], and these control proteins can be grouped by their function as follows

1. Sequestering proteins: these sequester actin monomers to prevent spontaneous nucleation and endwise polymerization of filaments (thymosin-$\beta 4$) or interact with actin monomers to control nucleotide exchange (profilin, cofilin, twinfilin, etc.).

2. Crosslinking proteins: these cross-link the actin filaments and can induce a sol-to-gel transition. An example is α-actinin. Others such as vinculin, talin, and zyxin link the actin cortex to the plasma membrane.

3. Severing proteins: these sever F-actin to generate filament ends for assembly or disassembly, such as the ADF/cofilin family of proteins and gelsolin.

4. Other proteins function to cap filament ends to regulate addition or loss of actin subunits (capping protein, Arp2/3 complex), to nucleate filament growth (Arp2/3 complex, formin), or to enhance subunit dissociation (cofilin).

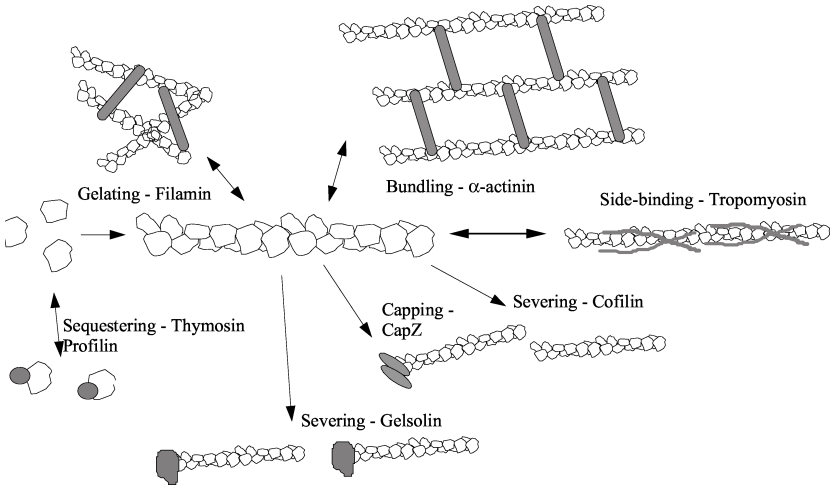

Figure 1.7: Some examples of the diverse actin-binding proteins [12].

There is control of monomeric actin pools via sequestration in a number of states, control of filament growth by capping of filament ends with gelsolin and other capping proteins, and breakage of filaments via ADF/cofilin, and annealing filaments. The interplay between these factors and others could produce a dynamically-varying distribution of actin filament lengths which has crucial implications for cellular motility.

1.3 Review of the previous models

1.3.1 Filament nucleation and elongation

The pioneering work by Oosawa and Asakura [13] analyzed the kinetics of size distribution of actin filaments in pure actin solution. The filament polymerization was proposed to take place through two sequential stages: the self-formation of filament nuclei via interaction of i_0 monomers (i_0=3-4) followed by continuous actin polymerization. The nucleation step is simplified as single reaction of reversible formation into i_0-mer, whereas actin addition/deletion to a polymer end at rates independent of the polymer length. The true equilibrium of filament length distribution was predicted to be an exponentially decreasing one based on the total interaction free energy of monomers in a polymer. The entire course of filament polymerization is

described in a sequence of steps: nucleation, growth, monomer/polymer equilibrium and length redistribution.

The dynamics of the bulk polymerization was analyzed in a special case where nucleation is artificially blocked and constant polymer number is maintained. The relaxation time for the establishment of monomer-polymer equilibrium was estimated to be of the order of

$$\tau_1 \sim 1/(k^+ m) \tag{1.2}$$

where m is the filament concentration, k^+ is on-rate of actin monomers. The profile of filament lengths resembles the Poisson distribution. As the monomer pool equilibrates with polymers at the critical concentration, the filaments are undertaking a slow process of length redistribution, which is completed in time of order of

$$\tau_2 \sim \bar{l}^2/(2k^-) \tag{1.3}$$

where $\bar{l}$ stands for the mean length, and k^- is the depolymerization rate. During this length redistribution phase, the monomers randomly walk among filament ends, which is characterized by a diffusion process of a rate of k^-. The nucleation-elongation model of filament polymerization is corroborated by the experimental observation by Kawamura *et al.* [14], where, when Mg^{2+}-polymer is polymerized in a large pool of G-actin, a Poisson-type distribution emerged and then evolved to the simple exponential one in about 25 hours.

1.3.2 Fragmentation and annealing

Wegner [15] was the first to introduce the effect of fragmentation into actin dynamics when he tried to fit the mathematical model with the polymerization curves of *in vitro* data. The filament severing models can be classified as two types: nucleotide-nonspecific fragmentation with a uniform rate, such as spontaneous breakage and gelsolin-caused severing; and the nucleotide-specific severing like ADF/cofilin. Erickson [16] conducted thermodynamic analysis on the subunit-subunit chemical bonds, and estimated the spontaneous fragmentation rate of order of 10^{-7}-10^{-8} s^{-1}.

Olesen *et al.* [17] explored the dynamics of polymer lengths in the case where the polymers are driven by a combination of diffusive growth and uniform fragmentation. The time evolution of filament lengths is analytically solved as the sum of orthogonal modes, whose magnitudes all decay exponentially in time except for the steady-state component. The equilibrium length profile is a size distribution of Bessel type as will be explained in Chapter 3. The mean length is proportional to $(D/k_f)^{1/3}$, where D denotes the diffusion coefficient in filament lengths, k_f means the uniform fragmentation rate. Importantly, this distribution is a global attractor for all initial length profiles. The relaxation time is proportional to $(Dk_f^2)^{-1/3}$.

The nucleotide-specific filament severing is theoretically investigated in the context of cofilin by Roland *et al.* [18]. There the barbed end is under a constant ATP-G-actin polymerization while the tail is severed by ADF/cofilin. ADF/cofilin cooperatively binds to ADP-F-actin, and promotes the Pi release from ADP-Pi-subunits. Severing is proposed to occur only between two adjacent cofilin-bounded F-actin, a potential severing state coded as as F-ADP-$(ADF)_2$. The severed fragment containing the pointed end of mother filaments are discarded, and only the 'live' filaments with a barbed end are counted in the data analysis. The number of 'live' filaments of length L at time t, $F(L,t)$, is regulated by the constant growth at the barbed end and stochastic fragmentation along the tail. The fragmentation rate along a length is proportional to the probability of two adjacent subunits being in the potential severing state. The latter probability distribution in the filament is in a ODE system which only account for the polymerization, ATP hydrolysis and Pi release. The resulting steady-state length distribution is then simply expressed as:

$$F(L) = C_1 \frac{L^5}{v^5} \exp\left(-C_2 \frac{L^6}{v^5}\right) \tag{1.4}$$

where C_1 and C_2 absorbed all relevant kinetic constants and L is the filament length. The equilibrium distribution is bell-shaped, with a marked peak, sharper than in a Gaussian distribution. In addition, the ratio of the standard-deviation to the average length is around 20% and is independent of all the kinetic parameters. Stochastic simulation of single filament length reveals the emergence of a dynamic treadmilling regime. In particular, after an initial stage of elongation

for $150 - 300$ seconds, filaments enter a regime where sustained growth is concurrent with sudden shrinkage. The polymerization at barbed end is, on average, balanced by the dissociation of the fragment severed by ADF/cofilin.

Sept *et al.* [19] measured the lengths of actin filaments formed by spontaneous polymerization of purified actin monomers and found that the steady-state length distributions are exponential with a mean of about 7μm independent of the initial actin monomer concentration. This is inconsistent with the original nucleation-elongation mechanism proposed by Oosawa [13]. Thus Sept *et al.* [19] formulated a deterministic model that incorporates nucleation but lumps all filaments of length greater than four monomers into one pool, and investigated the mechanisms underlying their experimental result. They proposed that incorporation of filament fragmentation and annealing is necessary to reproduce the observed average length. The annealing and fragmentation is regarded as a reversible second-order reaction between two filaments. Based on the assumption that the filaments are reacting in a reptative tube, the authors proposed the effective annealing rate is inversely proportional to the filament mean length. The fragmentation includes the spontaneous fragmentation uniformly occurs along the body and the fragmentation due to the filament-filament interaction. They showed that this successfully fits experimental data for the time course of polymerization *and* mean length observations, and they suggest that although the simple elongation-nucleation mechanism is able to describe the time course of polymerization, it seriously underestimates the average length. They concluded that the additional steps of filament fragmentation and annealing represent a minimal extension to the basic nucleation-elongation theory necessary to explain both the observed time course of polymerization and the mean length.

However, the model only predicts the first moment of the equilibrium length distribution. Lumping filament of various lengths in one group excludes the examination of higher moments of the steady-state distribution. In addition, as the authors pointed out, this model is applicable only to an intermediate concentration of actin molecules where the underlying reptation idea still holds. For low actin concentration ($< 25\ \mu$M), their model failed to fit the experimental data. Based on the frequency and strength of these filament interactions, the filament solution

are classified as dilute, semi-dilute and glass-like or nematic liquid crystalline [20]. In the dilute state, filaments rarely interact with others, and the impact of such inter-filament reactions might be negligible. In higher concentrations, however, the high frequency of polymer-polymer interactions greatly affect the time evolution of filament lengths. How the reacting environment influences filament annealing has been studied in the presence of crowding agents [21, 22]. Phalloidin-stabilized filaments were sheared into a population of many small fragments. The subsequent change of filament length is considered exclusively due to annealing, as phalloidin precludes the possibility of filament depolymerization and nucleation. In test tubes, it is observed that the growth of sheared actin fragments is initially rapid, and gradually slows down as filament lengths increase [21]. The annealing rate is estimated to be inversely proportional to the mean length. On the other hand, the filaments display a nearly constant annealing when the filaments are placed near a crowding hydrophilic surface [22]. On the contrast, the distribution of F-actin observed in [21] is exponential during the entire process, where it is Gaussian distributed in the experimental setting of [22]. It is thus suggested that the intracellular filament fragments may display a distinct annealing process at a location close to the crowded cell membrane, compared to that deep in the cell. The physical basis underlying the distinguished annealing kinetics near the surface and in solution remains unclear.

The equilibrium distribution of filament lengths has been investigated using the free energy argument by Biron *et al.* [23]. It was proposed that an exponential final distribution is typical of the system where entropy dominates interaction energies. The Gaussian-like distribution, however, is typical for a system when the interaction energies dominate. These interactions can be direct consequences of crosslinker proteins, polyvalent counterions or depletion-induced attraction. Therefore, the dynamics of filament lengths is complicated in the presence of varying reaction conditions and molecular agents.

1.3.3 Large filament length fluctuations

The studies on the actin filament dynamics have been done mostly in bulk solution, and the detailed examination of dynamics of single filament has just begun. By using actin directly

labelled with a fluorescent dye, Fujiwara *et al.* [24] recorded the length change of each end of a single filament. They noted that at the steady state a treadmilling filament displays a large length fluctuation, which is quantified as D, the rate of change of the variance of the length fluctuations. Based on the stochastic process of actin association and dissociation at both ends, the diffusion rate is predicted to be

$$D = \frac{1}{2}\delta^2(k^+c + k^-) \tag{1.5}$$

where δ is the length increment per monomer, c is the equilibrium concentration of actin monomer, and $k^{\pm}$ stand for total on- and off-rates at both ends, respectively. Strikingly, the measured data is 30-45 times higher than the prediction. A similar large fluctuation was observed by Kuhn *et al.* [25].

Vavylonis *et al.* [26] studied the potential influence of nucleotide caps on the length fluctuation in a stochastic model. Long ADP-associated filaments with blocked pointed ends are initially exposed to a buffer of fixed G-ATP pool. Monte Carlo simulations reveal that a mixed capping state of the barbed end by ATP, ADP-Pi and ADP at monomer pool slightly below G-ATP critical concentration generates a large length fluctuation. A tooth-shaped behavior of length diffusion around the critical concentration was theoretically predicted for an ideal case where the conversion of ATP to ADP is extremely slow. The jump of diffusion rate at the critical concentration is determined by the off-rate of G-ADP and G-ATP as

$$\lambda = D^-(c_{crit})/D^+(c_{crit}) = (k_D^-/k_T^-)^2. \tag{1.6}$$

The depolymerization rate of ADP-actin is typically 5 fold larger than that of ATP-actin, thus the dispersion of filament tip can be elevated about 35 fold below the critical concentration than above. However, according to this model, the large fluctuation occurs at concentrations slightly below the critical concentration of G-ATP at the barbed end, whereas in the experiment the large fluctuation is observed at the treadmilling concentration, which is higher than the critical concentration.

Later, Stukalin *et al.* [27] investigated the tip fluctuation near the critical concentration by considering a vectorial or sequential ATP hydrolysis mechanism. In particular, a typical filament

is characterized by $(l_1, k_1; l_2, k_2)$, where l_i is the length in monomers of the i-th protofilament, while k_i specifies the number of ATP-subunits in the corresponding protofilaments. The growth dynamics of single filament at each end can be obtained by solving the master equations for all possible polymer configurations. It turns out that a large length fluctuation takes place at a transition concentration

$$c_{tran} = (k_T^- + r_h)/k_T^+ \tag{1.7}$$

where r_h is the conversion rate of ATP to ADP. Above the transition concentration, the barbed end is definitely capped by ATP. The diffusion rate has a jump at the transition concentration

$$\lambda = \frac{D^-(c_{tran})}{D^+(c_{tran})} = 1 + \frac{2(k_D^- - k_T^-)(k_D^- + k_T^- + r_h)}{(k_T^- + r_h)(2k_T^- + r_h)} \tag{1.8}$$

which is similar to Vavylonis' prediction. However, this large fluctuation happens at the transition concentration, which is slightly higher than the treadmilling concentration.

The possibility that the filament annealing and fragmentation may induce large fluctuations was checked by stochastic simulations of actin filament dynamics [28]. The results indicate that the introduction of annealing/fragmentation does not reveal a high fluctuation at the steady state. The diffusivity-concentration curve in the presence of annealing/fragmentation is similar to that predicted by Vavylonis et al. [26]. To explore the possible effect of the experimental procedures, a detectability limit is introduced to represent a threshold length change such that either (i) an observer would have discarded in the length history or (ii) the event would have been prevented by cover-slip attachment. Accordingly, the high diffusivity was achieved at the steady state provided that fragmentation rate is 50-100 fold faster and concurrently a high frequency of annealing and fragmentation of filaments of length 1-2 μm is discarded. The improvement of microscopic resolution is required for understanding the large filament length fluctuation.

1.3.4 The nucleotide profile of filaments

A steady-state nucleotide profile within filaments was first solved by Bindschadler *et al.* [29]. A deterministic model of steady-state actin polymerization cycle was formulated in two sets of

equations: one set describes the steady state of F-actin and differentiated actin monomer pool, and the other governs the dynamics of nucleotide profile within filaments. They are coupled by the nucleotide type of filament tips and concentrations of actin monomers. The nucleotide profile is quantified as the fractional nucleotide content of i-th subunit within filaments. A hybrid solution was obtained, and the relationship between the nucleotide profile and various polymerization conditions were examined.

A characteristic nucleotide profile shows the following. Near the barbed end the probability of a subunit associated with ATP falls rapidly with a depth of only several subunits, where ADP-Pi has a prominent peak close to the barbed end and then decays exponentially to an ADP-rich interior. A low fraction of ADP at the barbed end was discovered, and disputed a previous simple assumption where the fraction of barbed-end-carrying ADP is the ratio of the association rate of ADP-actin to the total association rate of all actin types. A broad range of regulatory mechanisms is explored in this model by altering corresponding parameters. It predicted that a combination of enhancing Pi release from the ADP-Pi intermediate, elevating the pointed-end depolymerization of ADP-bound subunits and the functions of profilin boosts the filament treadmilling significantly.

In this model, the authors made an unjustified preaveraging assumption that the event of a filament has one nucleotide type at one place is completely independent of the nucleotide type at other positions. Furthermore, the inspected filament was fixed in length. In our work, we abandon these constrains, and conduct stochastic simulations to track the temporal evolution of the nucleotide profile within a filament. Contrastingly, we discover that the decaying ADP-Pi profile is induced by the length fluctuation of the barbed end, and it remains even with the pointed end blocked. Fass *et al.* [28] extended the exploration and examined potential changes on the nucleotide profile in the presence of annealing and fragmentation. Stochastic simulations revealed that fragmentation and annealing events produce qualitatively similar nucleotide profile as predicted by Bindschadler *et al.*.

1.4 Motivation of the current work

Filament lengths and dynamics are important for cell motility. To fulfill specific tasks, motile cells assemble various actin structures, such as lamellipodium, filopodia and stress fiber. The viscoelastic properties and mechanical strength of these structures is intrinsically determined by the length distribution of filament components [30]. An optimal filament length can be achieved *in vivo* via the fine coordination of filament-end-associated proteins, severing proteins, crosslinking proteins, etc.

Actin filament dynamics have been studied both analytically and computationally in the last three decades. One approach of these studies focuses on the evolution of individual actin filaments and their bulk length distribution, where filaments are polymerizing in the solution of purified actin monomers, or in the actin solution mixed with regulatory proteins of specific types. These *in vitro* experiments avoid the complex influence from the crowding *in vivo* environment.

A diverse shape of filament lengths are observed in experiments, and can be classified as three: Gaussian, Poisson and exponential distribution. Some models derived from thermodynamics theory predicted the steady state length profile, some kinetic models predict the steady state mean length and filament number. However, they failed to provide the temporal evolution of filament lengths. In our deterministic models, we differentiate filaments by their lengths, and track the length changes of all species. We thus examine the full dynamics of filament lengths in many processes, such as spontaneous polymerization, fragmentation and profilin-mediated polymerization. We pay special interest to the time scale of the dynamics, which is important in understanding how cells rapidly reorganize its actin structures in response to signals.

The nucleotide profile is important for filament polymerization, and lays the potential binding site for nucleotide-specific proteins. Due to the lack of efficient numerical algorithms, a systematic investigation on the temporal evolution of the nucleotides has not been done before. We implemented a recently developed simulation algorithm and successfully track the nucleotide history of single filament in various experimental settings.

Chapter 2

A deterministic model of pure actin polymerization

2.1 Introduction

The actin dynamics *in vivo* is extremely complicated due to the complex microenvironment and presence of many protein regulators. As a first step, we are to investigate the time-evolution of filament lengths in a rather simple reacting system, which consists of purified actin proteins alone. The processes involved include filament nucleation, endwise polymerization and depolymerization. The spontaneous growth of actin filaments thus is characterized by three distinct phases depending on the time scales. The actin filament is nucleated extremely fast in the nucleation phase. Subsequently, a formed filament seed elongates at a speed which is proportional to the available monomer pool. As the monomer pool approaches the critical concentration, the polymerization at filament ends is balanced by depolymerization, thus the filament lengths enter a diffusive process, which proves to be extremely slow. Consistent with *in vitro* experimental observations, the filament assembly trapped in the diffusive regime exhibits a Gaussian-like distribution[1] .

[1] The main result of this chapter is published in [31].

2.2 Formulation of the nucleation-elongation model

Let $\mathcal{M}_n$ denote a filament of length n, and let c_n be the corresponding concentration. We then propose a nuleaction-elongation model of actin dynamics as described in the following kinetic scheme [2]

$$\underbrace{\mathcal{M}_1 + \mathcal{M}_1 \underset{k_1^-}{\overset{k_1^+}{\rightleftarrows}} \mathcal{M}_2 \underset{k_2^-}{\overset{k_2^+ \mathcal{M}_1}{\rightleftarrows}} \mathcal{M}_3}_{\text{Nucleation}} \quad \underbrace{\underset{k_3^-}{\overset{k_3^+ \mathcal{M}_1}{\rightleftarrows}} \mathcal{M}_4 \quad \cdots \mathcal{M}_n \underset{k_n^-}{\overset{k_n^+ \mathcal{M}_1}{\rightleftarrows}} \mathcal{M}_{n+1} \cdots}_{\text{Propagation}}$$

The first two steps, which lead to formation of dimers and trimers, are distinguished in the above diagram by virtue of the fact that dissociation rates are extremely rapid for these steps, and thus it is difficult in a pure monomer solution to initiate filaments.

Assuming mass-action kinetics for the monomer addition and release, the above kinetic scheme leads to the system of ordinary differential equations

$$\begin{aligned}
\frac{dc_1}{dt} &= -2(k_1^+ c_1^2 - k_1^- c_2) - \sum_{n=3}^{N} (k_{n-1}^+ c_1 c_{n-1} - k_{n-1}^- c_n) = -2J_2 - \sum_{n=3}^{N} J_n \\
&\vdots \\
\frac{dc_n}{dt} &= (k_{n-1}^+ c_1 c_{n-1} - k_{n-1}^- c_n) - (k_n^+ c_1 c_n - k_n^- c_{n+1}) = \quad J_n - J_{n+1} \\
&\vdots \\
\frac{dc_N}{dt} &= (k_{N-1}^+ c_1 c_{N-1} - k_{N-1}^- c_N) = \quad J_N
\end{aligned} \tag{2.1}$$

Here the flux J_n from a filament of length $n-1$ into a filament of length n is defined as

$$J_n \equiv k_{n-1}^+ c_1 c_{n-1} - k_{n-1}^- c_n. \tag{2.2}$$

Note that these equations describe a discrete model of filament length dynamics. Since we only consider a closed system, we supplement (2.1) with the conservation condition

$$\sum_{n=1}^{N} n c_n = c_0, \tag{2.3}$$

[2] In the numerical computations described later we use kinetic constants reported by Sept *et al.* [19], which are $k_1^- = 10^6\ \text{s}^{-1}$, $k_2^- = 10^3\ \text{s}^{-1}$, and $k_n^- = 1\ \text{s}^{-1}$ for all $n \geq 3$ and $k_n^+ = 10\ \mu\text{M}^{-1}\text{s}^{-1}$, for all $n \leq N$.

where c_0 is the total concentration of actin in monomers and filaments.

To nondimensionalize (2.1) and (2.3), we define $u_n \equiv c_n/c_0$, and $\tau \equiv t/T$, where T will be chosen later to emphasize different aspects of the dynamics. Then (2.1) may be rewritten as

$$\begin{aligned}
\frac{du_1}{d\tau} &= -2(\kappa_1^+ u_1^2 - \kappa_1^- u_2) - \sum_{n=3}^{N}(\kappa_{n-1}^+ u_1 u_{n-1} - \kappa_{n-1}^- u_n) = -2j_2 - \sum_{n=3}^{N} j_n \\
&\vdots \\
\frac{du_n}{d\tau} &= (\kappa_{n-1}^+ u_1 u_{n-1} - \kappa_{n-1}^- u_n) - (\kappa_n^+ u_1 u_n - \kappa_n^- u_{n+1}) = \quad j_n - j_{n+1} \qquad (2.4) \\
&\vdots \\
\frac{du_N}{d\tau} &= (\kappa_{N-1}^+ u_1 u_{N-1} - \kappa_{N-1}^- u_N) = \quad j_N
\end{aligned}$$

where for all $n \leq N$,

$$\kappa_n^+ = k_n^+ c_0 T \;\text{ and }\; \kappa_n^- = k_n^- T \qquad (2.5)$$

It is clear that the set

$$\Omega \equiv \{u_n \,|\, 0 \leq u_n \leq 1, \quad \sum_{n=1}^{N} n u_n = 1\} \qquad (2.6)$$

is closed and bounded, and is invariant for all $t \geq 0$, and therefore the solution of (2.4) exists for all time.

2.3 Analysis of the dynamics and steady state

2.3.1 Existence, uniqueness and monotonicity of the steady state

At steady state the fluxes between filaments vanishes, which gives

$$u_n^s = K_{n-1} u_1^s u_{n-1}^s, \qquad \text{where } n = 2, 3, \ldots, N \qquad (2.7)$$

The conservation condition for the steady-state distribution then becomes

$$F(N, u_1) \equiv \sum_{n=1}^{N} n u_n = \sum_{n=1}^{N} n \Lambda_n (u_1^s)^n = 1 \qquad (2.8)$$

where $\Lambda_n = \prod_{i=1}^{n-1} K_i$, $K_i \equiv \kappa_i^+/\kappa_i^-$.

The left-hand side of (2.8) is monotone increasing with respect to u_1^s and vanishes at zero, which implies that the steady-state u_1^s exists and is unique. If in addition we assume that $\kappa_n^+ = \kappa^+$ for all $n < N$, $\kappa_n^- = \kappa^-$ for all $n \geq 3$, and define $K = \kappa^+/\kappa^-$, then $u_n^s/u_{n-1}^s = Ku_1$ for $n \geq 4$. It follows that the steady distribution is either exponentially increasing for $n \geq 4$ if $F(N, K^{-1}) < 1$, or exponentially decreasing otherwise. Thus $u_1 = K^{-1}$ defines a critical concentration that in dimensional form is given by $c_1 = k^-/k^+$.

2.3.2 Asymptotic convergence to the steady state

Next we show that the free energy defined below provides a Lyapunov function for the dynamics, and thus all solutions converge to the unique steady state asymptotically in time.

Consider the general monomer addition step

$$\mathcal{M}_1 + \mathcal{M}_{n-1} \underset{k_{n-1}^-}{\overset{k_{n-1}^+}{\rightleftarrows}} \mathcal{M}_n \qquad n = 2, \ldots, N$$

The affinity of this reaction is given by $A_n = \mu_1 + \mu_{n-1} - \mu_n$, where the chemical potentials are defined as

$$\mu_n = \mu_n^0(T, P) + RT \ln \frac{c_n}{c_T} = \mu_n^0(T, P) + RT \ln x_n. \tag{2.9}$$

Here x_n is the mole fraction of species n and c_T is the total concentration, including water. Ignoring the small changes in total concentration that accompany polymerization, we thus assume that c_T is constant at constant temperature and pressure.

The change in the Gibbs free energy (G) is given by

$$\frac{dG}{dt} = -\frac{\Phi}{c_T}, \tag{2.10}$$

where the dissipation function Φ is

$$\Phi = \sum_{n=2}^{N} A_n J_n = \sum_{n=2}^{N} \left(\Delta\mu_n^0 + RT \ln \frac{c_1 c_{n-1}}{c_T c_n} \right) (k_{n-1}^+ c_1 c_{n-1} - k_{n-1}^- c_n). \tag{2.11}$$

The Gibbs-Duhem relation has been used to eliminate one factor in deriving this. At thermodynamic equilibrium $A_n = 0$, and therefore

$$-\Delta\mu_n^0 = RT \ln \frac{c_1^s c_{n-1}^s}{c_T c_n^s}. \tag{2.12}$$

Define

$$\Lambda_n = \frac{c_1 c_{n-1}}{c_T c_n}, \quad \Lambda_n^* = \frac{c_T c_n^s}{c_1 c_{n-1}^s} \tag{2.13}$$

It follows that

$$\Phi = RT \sum_{n=2}^{N} \frac{k_{n-1}^+ c_n c_T}{\Lambda_n^*} \cdot (\Lambda_n \Lambda_n^* - 1) \cdot \ln(\Lambda_n \Lambda_n^*) \tag{2.14}$$

and this is of the form

$$\Phi = \sum a_n (z_n - 1) \ln z_n \tag{2.15}$$

where $a_n > 0, z_n > 0$. Since $(z_n - 1) \ln z_n \geq 0, \Phi \geq 0$ and vanishes only when $z_n = 1$, which corresponds to the equilibrium point.

2.3.3 The time evolution of the first and second moments

Next we derive the evolution equations for the first two moments of the length distribution under the assumption that $\kappa_n^+ = \kappa^+$ for all $n < N$ and $\kappa_n^- = \kappa^-$ for all $n \geq 3$.

Let $\mathcal{F}_2$ be the total concentration of filaments which has a length of at least two, and $\mathcal{P}$ be the dimensionless concentration of polymerized actin, then the time evolution of $\mathcal{F}_2$ and $\mathcal{P}$ is given by

$$\frac{d\mathcal{F}_2}{d\tau} = \frac{d}{d\tau}\left(\sum_{n=2}^{N} u_n\right) = j_2 = \kappa_1^+ u_1^2 - \kappa_1^- u_2 \tag{2.16}$$

and

$$\begin{aligned} \frac{d\mathcal{P}}{d\tau} &= \frac{d}{d\tau}\left(\sum_{n=2}^{N} n u_n\right) = 2j_2 + \sum_{n=3}^{N} j_n \\ &= 2\frac{d\mathcal{F}_2}{d\tau} + (\kappa^+ u_1 - \kappa^-)\mathcal{F}_2 - \underbrace{(\kappa_2^- - \kappa^-)u_3 + \kappa^- u_2 - \kappa^+ u_1 u_N}_{\text{boundary terms, or B.T.}} \end{aligned} \tag{2.17}$$

The terms labeled 'boundary terms' represent the contributions from the filament nuclei u_2 and u_3 and the terminal filament u_N.

If further we assume that $\kappa_1^+ = \kappa_1^- = 0$, and in effect, turn off the nucleation process, we fix the number of filaments and facilitate the analysis of the moment evolution. According to (2.16), $\mathcal{F}_2$ is constant and thus (2.17) can be rewritten as

$$\frac{d\mathcal{P}}{d\tau} \quad = \quad (\kappa^+ u_1 - \kappa^-)\mathcal{F}_2 + \text{B.T.} \tag{2.18}$$

Let X be a non-negative integer-valued random variable defined on the set of filaments and define the probability measure

$$P(X = n) = \frac{u_n}{\sum_{n=2}^{N} u_n}. \tag{2.19}$$

Under the above assumption, the expected value of X is given by $\mathbb{E}X = \mathcal{P}\mathcal{F}_2^{-1}$. Hence,

$$\frac{d\left(\mathbb{E}X\right)}{d\tau} = (\kappa^+ u_1 - \kappa^-) + \text{B.T.} \tag{2.20}$$

It is easy to see that

$$\sum_{n=2}^{N} \frac{d(n^2 u_n)}{d\tau} \quad = \quad 2(\kappa^+ u_1 - \kappa^-)\mathcal{P} + 2\kappa^+ u_1 \mathcal{F}_2 - \frac{d\mathcal{P}}{d\tau} + \text{B.T.} \tag{2.21}$$

and since $\mathcal{F}_2$ is constant, it follows that the second moment

$$\mathbb{E}\left(X^2\right) = \sum_{n=2}^{N} \frac{n^2 u_n}{\mathcal{F}_2} \tag{2.22}$$

satisfies the evolution equation

$$\frac{d}{d\tau}\left(\mathbb{E}(X^2)\right) = 2(\kappa^+ u_1 - \kappa^-)\frac{\mathcal{P}}{\mathcal{F}_2} + 2\kappa^+ u_1 - \frac{d(\mathbb{E}X)}{d\tau} + \text{B.T.} \tag{2.23}$$

By the combination of (2.20) and (2.23) one finds that if (i) the concentration of monomers is critical, and (ii) the boundary terms are negligible, then

$$\frac{d}{d\tau}\mathbb{E}X = 0, \frac{d}{d\tau}\text{Var}(X) = \text{ constant} \tag{2.24}$$

Therefore, under the stated conditions the first two moments of the length distribution evolve according to a diffusion process. As we will see in the next section, this provides an accurate description of the evolution on a long, intermediate time scale, but not early in the evolution from a pure monomer pool, nor in the late stages where boundary effects are important.

2.4 The time evolution of the filament length distribution

2.4.1 The phases of filament polymerization

Now we focus on understanding the different stages in the evolution of the length distribution. In order to illustrate what is to be understood, we show a computational result for the evolution in Figure 2.1. We state initial conditions as concentrations, but we present the results [3] in terms of the numbers of a given species [4] .

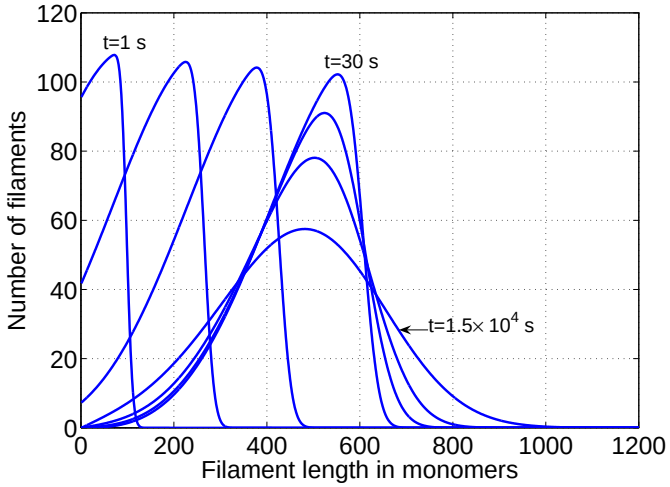

Figure 2.1: Time evolution of the filament length distribution. The initial concentration of G-actin is 10 μM. The depicted profiles correspond to 1, 3, 6, 30, 10^3, 3×10^3, and 1.5×10^4 secs, respectively.

There are three distinct regimes in this figure: the initial stage characterized by formation of the maximum peak height in the distribution, the subsequent polymerization-driven advective phase in which the mean length increases, and a slow final stage in which monomers are redistributed among filaments and the length distribution evolves to the steady-state distribution.

The large disparity between the off rates for filaments of length greater than three monomers and those for dimers and trimers leads to four well-defined time scales in the early dynamics,

[3] Throughout, the numerical computations were done using Gear's method, as implemented in the Livermore solver LSODE.

[4] Unless stated otherwise, the initial condition for the computational results is a pure monomer pool in a volume of 2000 μm^3, which is the volume of a typical cell.

which can be defined in reference to Figure 2.2. We lump the species into four pools, comprising monomers, dimers, trimers, and filaments of length four and longer, respectively. The four time scales in increasing order correspond to (i) equilibration of monomers and dimers ($T_1 \sim (k_1^- + 4k^+c_1(0))^{-1} \sim \mathcal{O}(10^{-6})$ sec.), (ii) the time at which the trimers reach their maximum ($T_2 \sim (k_2^- + 9 \cdot k_2^+ K_1 c_1(0)^2)^{-1} \sim \mathcal{O}(10^{-3})$ sec.), (iii) establishment of the total number of filaments (T_3), and (iv) equilibration of the monomer pool with the filaments (T_4).

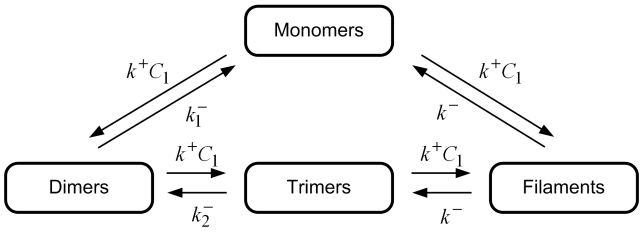

Figure 2.2: A schematic of the network for nucleation and filament growth.

2.4.2 The filament nucleation phase

On the time scale T_2 the trimer population peaks, and then dimers and trimers equilibrate with the monomer pool, whereas the slower formation of filaments can be neglected on this scale. Thus we can solve the steady-state version of the first three equations in (2.4) and obtain

$$u_2 = K_1 u_1^2 \qquad u_3 = K_1 K_2 u_1^3. \tag{2.25}$$

This gives an estimate of the trimers at any time, and in particular, an estimate of the maximum amount of trimers in the system, namely $u_3 = K_1 K_2 u_1^3(0)$. As can be seen in Figure 2.3(a) for $c_0 = 10\ \mu M$, (2.25) provides a very good estimate of the number of trimers except for an initial time interval of order T_2. For an initial concentration of 10 μM, the maximum estimated number of trimers is 120, whereas the computed maximum is approximately 110 (see Figure 2.3(a)). This approximation is acceptable as long as the initial concentration of monomer is not too high, but for an initial concentration of 100 μM the maximum estimated number of trimers is approximately 1.2×10^5, whereas the computed maximum is approximately 5.8×10^4. This

is predictable, since by increasing the monomer concentration the trimer-to-filament pathway in Figure 2.2 is enhanced and the corresponding dynamics are no longer slow on the time scale characterized by T_2.

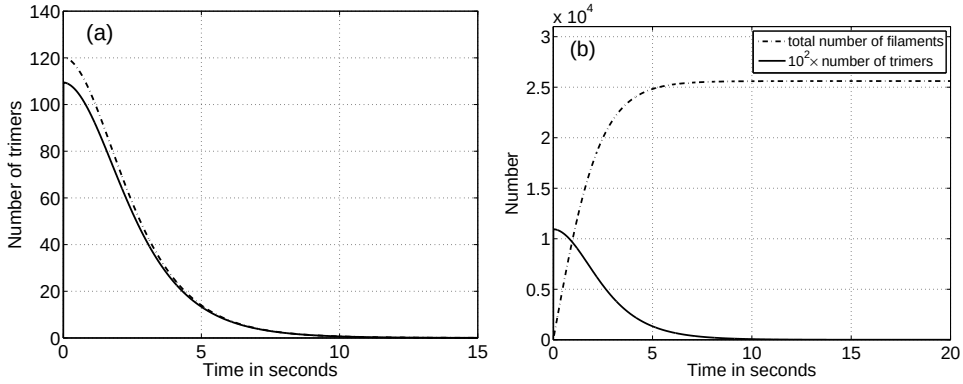

Figure 2.3: The time evolution of trimers and filament population. The initial concentration of G-actin is 10 μM. The solid line on the left figure corresponds to the numerical computations, whereas the dashed line corresponds to the theoretical approximation given by (2.25).

In the next phase, the trimer concentration (or number) decreases monotonically and when it reaches a level at which there is only one trimer, the total number of filaments essentially stops increasing. To estimate the end of this phase, which one sees is about 8 secs in Figure 2.3(b), we define

$$\mathcal{F}_4 = \sum_{n=4}^{N} u_n \tag{2.26}$$

and then have

$$\begin{aligned} \frac{du_1}{d\tau} &= -2(\kappa_1^+ u_1^2 - \kappa_1^- u_2) - \sum_{n=3}^{N} \left(\kappa_{n-1}^+ u_1 u_{n-1} - \kappa_{n-1}^- u_n\right) \\ &= -2j_2 - j_3 - \kappa^+ u_1 (u_3 - u_N) - (\kappa^+ u_1 - \kappa^-)\mathcal{F}_4 \qquad (2.27) \\ \frac{d\mathcal{F}_4}{d\tau} &= \kappa_3^+ u_1 u_3 - \kappa_3^- u_4 \qquad (2.28) \end{aligned}$$

Since the trimers have already equilibrated with the monomer pool we assume that the fluxes j_2 and j_3 are negligible. We also assume that the non-dimensional concentrations u_3 and u_N are small compared to $\mathcal{F}_4$ and that $u_3 \approx u_4$ at this phase. This leads to the following approximation

to the system of (2.27) and (2.28).

$$\frac{du_1}{d\tau} = -(\kappa^+ u_1 - \kappa^-)\mathcal{F}_4 \quad (2.29)$$

$$\frac{d\mathcal{F}_4}{d\tau} = (\kappa^+ u_1 - \kappa^-)K_1 K_2 u_1^3 \quad (2.30)$$

From (2.25) one can see that, given the standard parameter values, when the number of trimers is one, $\kappa^- \ll \kappa^+ u_1$. Thus we further approximate the system (2.29) and (2.30) as follows.

$$\frac{du_1}{d\tau} = -\kappa^+ u_1 \mathcal{F}_4 \quad (2.31)$$

$$\frac{d\mathcal{F}_4}{d\tau} = \kappa^+ K_1 K_2 u_1^4 \quad (2.32)$$

From these one finds that

$$\ln \frac{(1 + (1 - (u_1/u_1(0))^4)^{\frac{1}{2}})}{(1 - (1 - (u_1/u_1(0))^4)^{\frac{1}{2}})} = 4(\kappa^+ \kappa^+ K_1 K_2)^{\frac{1}{2}} u_1(0)^2 \tau \quad (2.33)$$

Using this and (2.25) shows that the time T_3 needed for the trimer population to drop below one is approximately 6 seconds, which corresponds very well with the computed result shown in Figure 2.3(b).

2.4.3 The convective phase

The next phase is characterized by a roughly constant shape of length distribution, but the speed of this traveling wave gradually slows as the monomer pool decreases (see Figure 2.5). To understand when this phase ends and the wave stops, note that the monomer concentration approaches the critical level defined earlier, which led us to approximation (2.29)-(2.30) instead of the subsequent approximations.

By integrating Equations (2.29) and (2.30) numerically we obtain an estimate of 30 seconds for the time T_4 needed for the equilibration of the number of monomers. In fact one sees in Fig 2.4(a) that this system provides an excellent approximation for u_1 for all but a short initial time interval when the initial concentration of G-actin, which is an alternative way to denote actin monomers, is 10 μM. For an initial G-actin concentration of 100 μM, the estimated time needed

for G-actin equilibration is 0.3 seconds, but one sees in Figure 2.4(b) that the approximation of the time evolution is not as accurate as for an initial concentration of 10 μM. Thus, when the monomer concentration increases 10 fold, the time scale decreases hundred fold, as can also be seen from the dimensionless on rate κ^+.

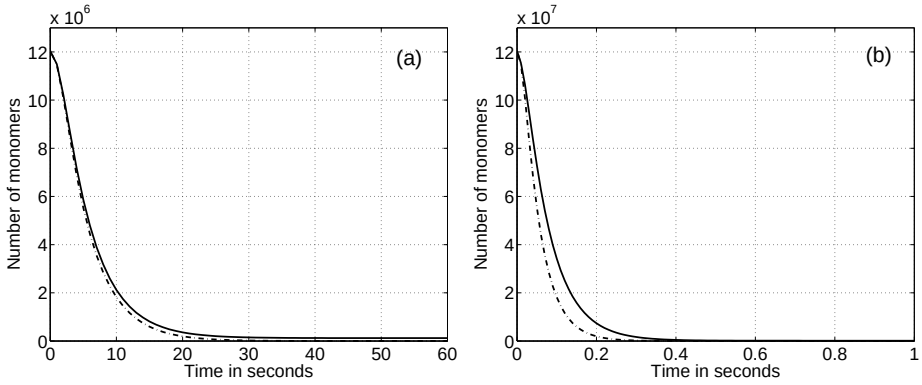

Figure 2.4: The time evolution of G-actin population. The initial concentration of G-actin is 10μM on the left and 100μM on the right. The solid lines represent the corresponding numerical solutions, whereas dashed lines correspond to the theoretical approximation, given by (2.29) and (2.30).

To understand the evolution when the filament number is constant, for $n \geq 4$ the evolution equations (2.4) can be written as

$$\frac{du_n}{d\tau} + (\kappa^+ u_1 - \kappa^-)(u_n - u_{n-1}) = \frac{\kappa^+ u_1 + \kappa^-}{2}(u_{n-1} - 2u_n + u_{n+1}) \tag{2.34}$$

The second term on the left can be regarded as a convective flux with the time-dependent speed $(\kappa^+ u_1 - \kappa^-)$, whereas the term on the right is diffusion with the diffusion rate constant as $(\kappa^+ u_1 + \kappa^-)/2$. When $(\kappa^+ u_1 - \kappa^-) > (\kappa^+ u_1 + \kappa^-)/2$ convection dominates, but as the monomer concentration approaches the critical level $u_1 = \kappa^-/\kappa^+$, the speed goes to zero and the evolution is dominated by diffusion. Thus one predicts that the hyperbolic phase ends when the monomer reaches the critical level, and ones sees in Figure 2.5(a) that this prediction is accurate.

Using the relation between the peak speed and the monomer dynamics, one can approximate

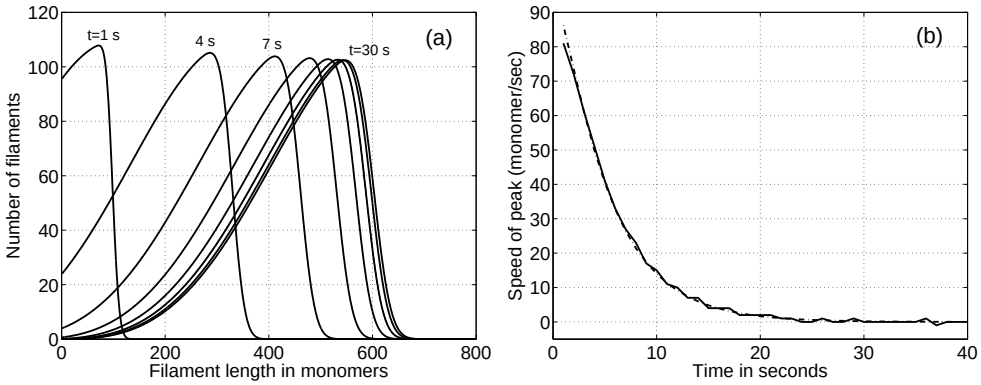

Figure 2.5: The convective phase of actin dynamics for an initial concentration of 10 μM. The profiles in (a) correspond to 1, 4, 7, 10, 13, 16, 19, and 30 secs, respectively. The speed of the traveling peak is shown in (b), where the solid line corresponds to the speed computed by numerically tracking the peak location, whereas the the dashed line corresponds to the theoretical approximation given by the convective term in (2.34).

the filament length at which the peak stalls by the expression

$$N^* = \int v(t)\mathrm{d}t = \int \left(k^+ c_1(t) - k^-\right) \mathrm{d}t \tag{2.35}$$

If (2.29) and (2.30) are used to predict the monomer dynamics, then (2.35) predicts that $N^* \approx 576$ for $c_0 = 10$ μM, whereas the result obtained from the full system is $N^* \approx 555$. However, for reasons similar to those given earlier, the approximation is not as accurate for $c_0 = 100$ μM, where the predicted value is $N^* \approx 58$ and the actual value is $N^* \approx 68$. Also as before, if c_0 increases ten fold the time scale decreases hundred fold, and we expect an approximately ten-fold decrease in N^*.

2.4.4 The diffusive phase

The hyperbolic phase ends coincidently with the onset of the diffusive reorganization of the length distribution. The dynamics at this stage are characterized by a monomer concentration that is approximately critical, and a fixed number of filaments. The analysis of the moment equations in Section 2.3.3 indicates that diffusion is the dominant process in this phase, and numerical results for the full system shown in Figure 2.6 confirm this. In Figure 2.6 one sees

that the mean length of the distribution only increases about 1% after the first thirty seconds, and the estimated diffusion coefficient is found to be approximately 1 monomer^2/sec.

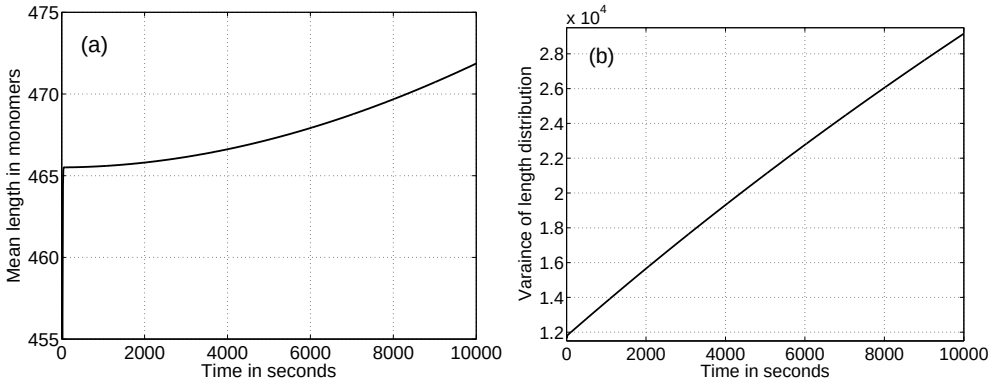

Figure 2.6: The time evolution of the mean and variance of the filament length distribution.

To better understand when the diffusive regime applies, we consider the time scale set by the depolymerization rate k^-. It follows from (2.5) that $\kappa^- = 1$, and we further assume that u_1 has equilibrated at the critical concentration, which implies that system (2.4) becomes linear. If we let $u = (u_2, u_3, \cdots, u_N)^T$ and $\Gamma = \left(\kappa_1^+ u_1^2, 0, \cdots 0\right)^T$, then (2.4) are equivalent to

$$\frac{du}{d\tau} = Au + \Gamma \tag{2.36}$$

where A is the $(N-1) \times (N-1)$ matrix

$$A = \left[\begin{array}{cc|ccccc} -(\kappa^+ u_1 + \kappa_1^-) & \kappa_2^- & 0 & & & & \\ \kappa^+ u_1 & -(\kappa^+ u_1 + \kappa_2^-) & 1 & 0 & & & \\ \hline 0 & \kappa^+ u_1 & -(\kappa^+ u_1 + 1) & 1 & & & \\ & 0 & \kappa^+ u_1 & \ddots & \ddots & & \\ & & & \ddots & -(\kappa^+ u_1 + 1) & 1 & \\ & & & & \kappa^+ u_1 & -1 \end{array}\right].$$

We use a perturbation argument to obtain information with respect to the eigenvalues of A. We rewrite A in the form

$$A = \epsilon^{-1} B = \epsilon^{-1}(A_0 + \epsilon A_1) \tag{2.37}$$

where $\epsilon = \mathcal{O}(10^{-6})$ and

$$A_0 = \left[\begin{array}{cc|ccccc} -1-10^{-6} & 10^{-3} & 0 & & & & \\ 10^{-6} & -10^{-3}-10^{-6} & 0 & 0 & & & \\ \hline & & & & & & \\ 0 & 0 & -2\times 10^{-6} & 10^{-6} & & & \\ & 0 & 10^{-6} & -2\times 10^{-6} & & & \\ & & & \ddots & \ddots & & \\ & & & 10^{-6} & -2\times 10^{-6} & 10^{-6} & \\ & & & & 10^{-6} & -10^{-6} & \end{array}\right]$$

$$A_1 = \left[\begin{array}{cc|ccccc} 0 & 0 & 0 & & & & \\ 0 & 0 & 1 & 0 & & & \\ \hline & & & & & & \\ 0 & 1 & 0 & 0 & & & \\ & 0 & 0 & 0 & & & \\ & & & \ddots & \ddots & & \\ & & & 0 & 0 & 0 & \\ & & & & 0 & 0 & \end{array}\right],$$

Let λ_0 be an eigenvalue of A_0. The eigenvalues of the first 2×2 block are clearly -1.000001 and -0.001001, whereas the latter $(N-3)\times(N-3)$ block has eigenvalues as $\alpha_k \times 10^{-6}$,

where the α_k are the eigenvalues of the matrix

$$\Delta = \begin{pmatrix} -2 & 1 & & & & \\ 1 & -2 & 1 & & & \\ & 1 & -2 & & & \\ & & & \vdots & & \\ & & & -2 & 1 & \\ & & & 1 & -2 & \end{pmatrix}_{(N-3)\times(N-3)}$$

The eigenvalues and eigenvectors of this matrix can be computed explicitly [32] and are given by

$$\alpha_k = -4\sin^2\left(\frac{\pi(k-5/2)}{2N-5}\right) \qquad k = 3,\ldots,N-1 \tag{2.38}$$

$$u_{k,l} = \sqrt{\frac{2}{(N-5/2)}}\sin\left(\frac{\pi(k-5/2)l}{N-5/2}\right) \qquad l = 1,\ldots,N-3. \tag{2.39}$$

Thus all the eigenvalues of A_0 are simple. Standard results from perturbation theory [33] show that the eigenvalues of B can be written in the form

$$\lambda = \lambda_0 + \epsilon\lambda_1 + \mathcal{O}(\epsilon^2) \tag{2.40}$$

$$y = y_0 + \epsilon y_1 + \mathcal{O}(\epsilon^2) \tag{2.41}$$

An easy calculation shows the eigenvalues of B as given in Table 2.1.

Therefore, on the $\mathcal{O}(1)$ time scale there are two large negative eigenvalues corresponding to the relaxation rate of monomer/dimers, and dimers/trimers, respectively, and $N-3$ eigenvalues that arise from the discrete Laplacian Δ. The latter eigenvalues represent the time scales for relaxation of the diffusional modes that characterize the re-shuffling of monomers amongst the filaments during the diffusive phase. The lowest modes relax on a time scale of order 10^6 secs, for $N \sim \mathcal{O}(10^3)$. This explains the very slow diffusive phase in the evolution of the length distribution, and to further substantiate this, we reconstruct the length distribution at a sequence of times in terms of the eigenfunction of A. As shown in Figure 2.7(a) this can be done accurately using only the three slowest modes for $T \sim \mathcal{O}(10^5)$ secs ($\sim$ 30 hours), but

Table 2.1: Terms in the perturbation expansion of the eigenvalues

Index	λ_0	λ_1
1	-1.000001	0
2	-0.001001	0
$k = 3, N-1$	$\alpha_k \times 10^{-6}$	0

more are required for earlier times. Moreover, Figure 2.7(b) shows that the evolution of the amplitudes proceeds as expected in that the higher modes decay rapidly, as predicted by the linear theory.

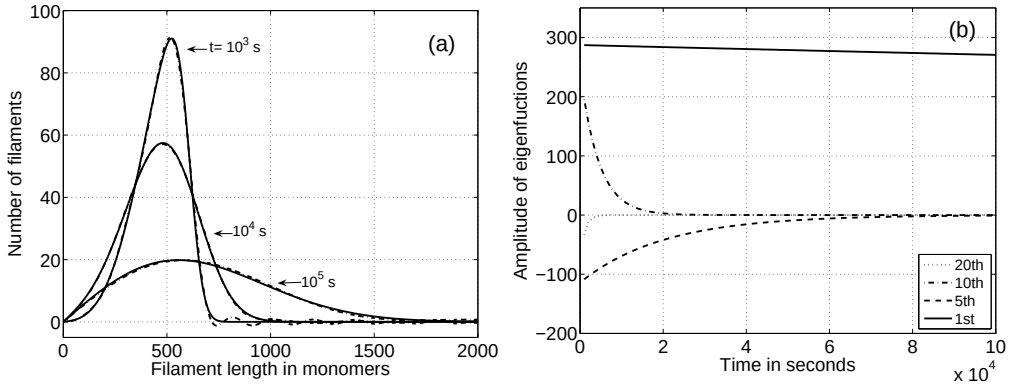

Figure 2.7: Reconstruction of the length distribution in terms of the eigenfunctions (a), and the time evolution of the amplitudes of eigenfunctions needed (b). In (a) the dotted lines represent the reconstruction of the length distribution, whereas the solid lines represent the computational results. For t $= 10^3, 10^4, 10^5$ s, the reconstruction requires only the lowest $20, 10, 3$ modes, respectively.

As a final remark we note that, although the evolution of the mean and variance in Figure 2.6 indicates the existence of a diffusion process , the diffusion-dominated phase in the

original experiment, where the nucleation pathway is active, is more complicated than a pure diffusion process. This is due to the existence of the trimer-to-dimer and dimer-to-monomers reaction pathways through which some of the monomers return to the monomer pool. Our numerical computations indicate that the number of filaments in solution decreases by 400 during a time interval of $\sim 10,000$ seconds after the initiation of the diffusion-dominated phase. That is, 400 trimers depolymerize to monomers and, hence, the monomer pool increases by $1,200$ monomers. Of course this number is negligible compared to the $\sim 10^5$ monomers in the monomer pool during the diffusion phase, but, nonetheless, contributes to a small deviation from pure diffusion.

Chapter 3

The dynamics of pure filament polymerization with fragmentation

3.1 Introduction

In the previous chapter, a simple nucleation-elongation model of actin filament growth was proposed to predict a long-lived Gaussian-like profile of filament lengths, which agrees very well with purified actin experiments [34] (compare Figure 2.1 and Figure 3.1(A)). Eventually this intermediate unimodal length profile evolves to an exponential distribution. However, the actin structure should be able to change its lengths rapidly in order to meet the mechanical requirement for cell locomotion. Many additional actions must be exerted on actin lengths to achieve this demand. Abrupt fragmentation is one of the reactions postulated to importantly influence the actin structure reorganization during both the steady cell sliding motion and sudden membrane protrusions [35]. It is observed that the incorporation of fragmentation in actin dynamics characteristically modifies the filament length distribution from an exponential steady-state distribution to a Poisson-like one as depicted in Figure 3.1(B) [34]. This chapter is devoted to the effect of fragmentation on filament length dynamics. We assume a uniform fragmentation at any subunit-subunit bond in a filament. Strikingly, the addition of fragmentation, even with a

small rate, characteristically changes the steady-state filament length profile. The fragmentation occurring within a filament body, together with monomer redistribution at filament ends, forces a Poisson-like distribution. The final distribution is similar for all rates of fragmentation.

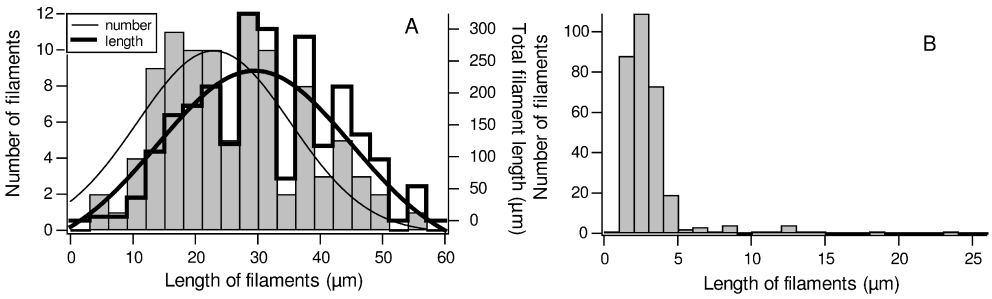

Figure 3.1: The actin filament length distributions observed in *in vitro* assays (from [34]). Figure A corresponds to the spontaneous polymerization of pure actin proteins, whereas in Figure B the filament is polymerizing in the presence of severin proteins.

3.2 Formulation of the fragmentation model

In the following, we investigate the actin filament dynamics in the presence of fragmentation. Severing is assumed to take place between any two adjacent subunits except the terminal pairs. Thus individual filament is severed into fragments of lengths ranging from 2 to N-2 subunits. As treated in the nucleation-elongation model, the two filament ends are not distinguished and effective on- and off-rate are assumed. The dynamics of filament populations are governed by

the differential equations:

$$
\begin{aligned}
\frac{dc_1}{dt} &= -2(k_1^+ c_1^2 - k_1^- c_2) - \sum_{i=3}^{N}(k_{i-1}^+ c_1 c_{i-1} - k_{i-1}^- c_i) = -2J_2 - \sum_{i=3}^{N} J_i \\
\frac{dc_2}{dt} &= k_1^+ c_1 c_1 - k_1^- c_2 - k_2^+ c_1 c_2 + k_2^- c_3 + 2k_f \sum_{i=4}^{N} c_i \\
\frac{dc_3}{dt} &= k_2^+ c_1 c_2 - k_2^- c_3 - k_3^+ c_1 c_3 + k_3^- c_4 + 2k_f \sum_{i=5}^{N} c_i \\
\frac{dc_4}{dt} &= k_3^+ c_1 c_3 - k_3^- c_4 - k_4^+ c_1 c_4 + k_4^- c_5 - k_f c_4 + 2k_f \sum_{i=6}^{N} c_i \\
&\cdots \\
\frac{dc_n}{dt} &= k_{n-1}^+ c_1 c_{n-1} - k_{n-1}^- c_n - k_n^+ c_1 c_n + k_n^- c_{n+1} - (n-3)k_f c_n + 2k_f \sum_{i=n+2}^{N} c_i \\
\frac{dc_N}{dt} &= (k_{N-1}^+ c_1 c_{N-1} - k_{N-1}^- c_N) - (N-3)k_f c_N
\end{aligned}
\tag{3.1}
$$

where $k^{\pm}$'s and c_i's are the same as defined in the nucleation-elongation model, and k_f denotes the uniform fragmentation rate. The mass conservation condition requires

$$\sum_{i=1}^{N} i \cdot c_i = c_0 \tag{3.2}$$

A sufficiently large N is imposed on the system such that the concentrations of long filaments are negligible.

3.3 Analysis of the steady state of filament polymerization

3.3.1 The monomer pool at the steady state

At the steady state, the size changes of all filament populations vanish. Thus one can solve backward for c_n as functions of c_1 and c_N at the steady state; i.e.

$$c_n = f_n(c_1, c_N) \tag{3.3}$$

These relations, together with the mass conservation condition, render a steady-state solution of (3.1). However, it is impossible to solve the steady-state solution analytically due to the high

non-linearity of the f_n's. In spite of this, one could derive that the steady-state monomer pool is close to the critical concentration ($= k^-/k^+$) as below.

The ODE system (3.1) gives the rate change of actin monomer pool as

$$\frac{dc_1}{dt} = -(2J_2 + J_3 + k^+c_1c_3 - k^+c_1c_N) - (k^+c_1 - k^-)\sum_{i=4}^{N} c_i \tag{3.4}$$

and the rate of change of the remaining population as

$$\frac{d}{dt}\left(\sum_{i=2}^{N} c_i\right) = J_2 + k_f \sum_{i=4}^{N}(i-3)c_i \tag{3.5}$$

At the steady state, the rate changes of both quantities vanish. The cancellation of J_2 from the above equations then gives

$$(k^+c_1 - k^-)\sum_{i=4}^{N} c_i = 2k_f \sum_{i=4}^{N}(i-3)c_i - (J_3 + k^+c_1c_3 - k^+c_1c_N) \tag{3.6}$$

We can neglect the second term of the right hand side of (3.6), since (i) the nucleation pathway equilibrates faster than the polymerization at filament ends, and (ii) c_N is negligible as we choose the maximal length to be sufficiently large. We then obtain

$$c_1 \doteq (k^-/k^+) + 2k_f(\bar{l}_0 - 3)/k^+ \tag{3.7}$$

where the steady-state average length $\bar{l}_0 \equiv \left(\sum_{i=4}^{N} ic_i\right) / \left(\sum_{i=4}^{N} c_i\right)$. Later we show that the average length is a power function of the fragmentation rate.

The second term of (3.7) is small compared to the first term, thus at steady state the monomer pool is approximately equal to the critical concentration ($= k^-/k^+$). For example, a later simulation in Section 3.4 shows that when $k_f = 10^{-6}$ s^{-1} the average length is around 140 monomers, thus (3.7) estimates $c_1 = 0.10003$ μM. This is very close to the steady state of monomer pool obtained by numerically solving the full system (3.1) as depicted in Figure 3.4.

3.3.2 The steady-state distribution of filament lengths

At the steady state, the filament populations of various lengths are constant. The concentrations c_i ($i \geq 2$) satisfy a set of linear equations provided that c_1 is known. We estimated in (3.7) that

at the steady state $\bar{c}_1 \approx k^-/k^+$, so the solution satisfies

$$A_0 \cdot c = b \tag{3.8}$$

where $\bar{c} = (\bar{c}_2, \bar{c}_3, \ldots, \bar{c}_N)'$, $b = (-(k^-)^2/k^+, 0, \ldots, 0)$, and

$$A_0 = \begin{pmatrix} -a_2 & k_2^- & 2k_f & 2k_f & \ldots & 2k_f & 2k_f & 2k_f & 2k_f \\ k^- & -a_3 & k^- & 2k_f & \ldots & 2k_f & 2k_f & 2k_f & 2k_f \\ 0 & k^- & -a_4 & k^- & \ldots & 2k_f & 2k_f & 2k_f & 2k_f \\ & & & & \vdots & & & & \\ 0 & 0 & 0 & 0 & \ldots & 0 & k^- & -a_{N-1} & k^- \\ 0 & 0 & 0 & 0 & \ldots & 0 & 0 & k^- & -a_N \end{pmatrix}$$

where

$$a_i = \begin{cases} k_1^- + k^- & i = 2 \\ k_2^- + k^- & i = 3 \\ k^- + (N-3)k_f & i = N \\ 2k^- + (i-3)k_f & \text{otherwise.} \end{cases}$$

The solution of above linear equation is

$$\bar{c} = A_0^{-1} \cdot b. \tag{3.9}$$

Numerical results indicate that the predicted steady-state solution of (3.9) agrees very well with the steady-state solution of the full system over a wide range of fragmentation rates as displayed in Figure 3.2.

The steady-state filament lengths reveal that the fragmentation action produces a unimodally distributed filament sizes, which achieve a maximal population size at an intermediate length. This is characteristically distinguished from the previous case where the nucleation and elongation are the only processes. For the nucleation-elongation model, the steady-state distribution is of the exponential type and thus the maximal population size is either at the shortest length

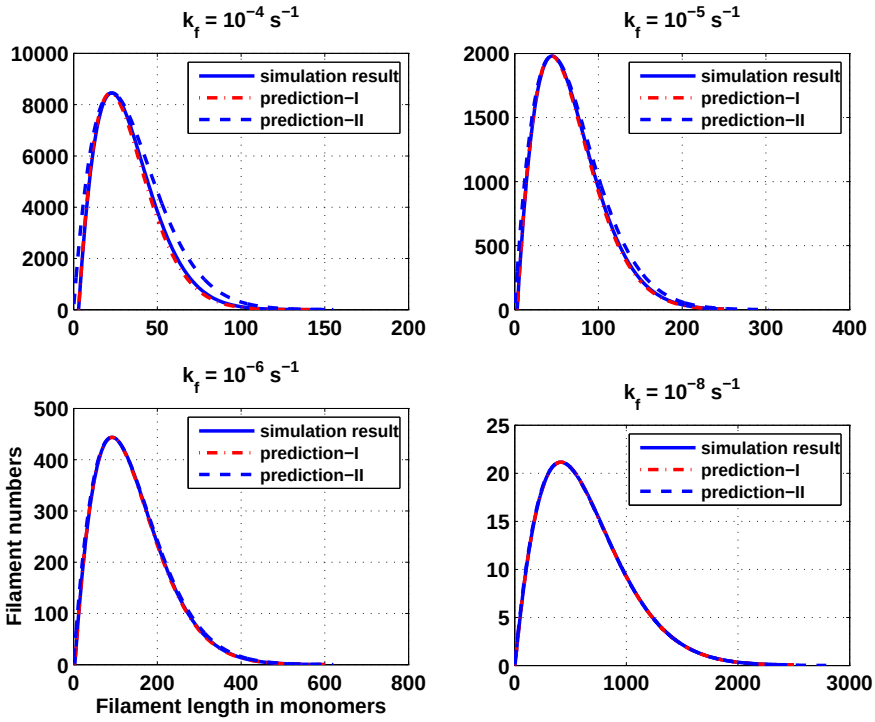

Figure 3.2: The steady-state distributions of filament lengths at various fragmentation rates. Blue lines represent the steady-state distribution from simulation results; prediction-I represents that predicted by (3.9), whereas prediction-II depicts the steady-state distribution as predicted by (3.31).

or longest length. Furthermore, the distributions are similar over a wide range of fragmentation activities as shown in Figure 3.2. With elevated fragmentation rates, the filament lengths tends to shrink and population sizes will increase.

The establishment of the unimodal steady-state distribution of actin filaments in the presence of fragmentation, as will be explained in detail in next section, is the consequence of balance of opposing forces. On one side, fragmentation tends to reduce the filament size by cutting filaments into two. On the other, the short fragments accumulated from fragmentation will be recycled to the monomer pool via the nucleation pathway, which in turn adds to the filament ends. In an average sense, at the steady state the amount of filament length decrease by fragmentation is compensated by polymerization at the ends of the filaments.

3.4 Analysis of the dynamics of filament length distribution

3.4.1 Overview of the time evolution of filament lengths

Numerical simulations were performed to examine how fragmentation influences the filament length dynamics. For all simulations, 10 μM actin proteins are initially present in the monomeric state only. The same set of kinetic constants as in Chapter 2 are applied to the filament nucleation and polymerization.

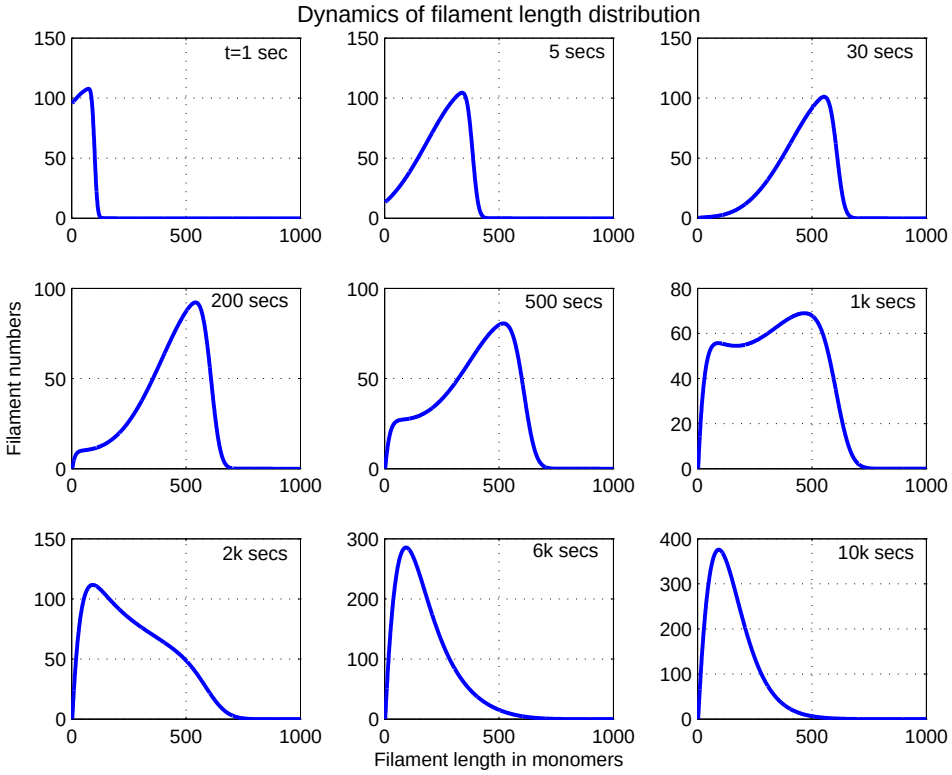

Figure 3.3: The size distribution of actin filaments in the presence of severing activity. The fragmentation rate is set to be $k_f = 10^{-6}$ s^{-1}.

An illustration of filament length dynamics is presented in Figure 3.3. The filament seeds are spontaneously formed immediately after the onset of the simulation. Then a peak-like length

profile emerges and convects smoothly to the right, which indicates the filament lengths are continuously increasing. This convective phase lasts for about 30 seconds, and a skewed Gaussian-like distribution is established at the end of this phase. Heretofore the dynamics of filament lengths in the first 30 seconds is indistinguishable from that in the nucleation-elongation model.

After that, the filaments enter a slow phase of size redistribution, where the fragmentation starts to exert a significant effect on the dynamics. Filaments gradually expand their population size at the expense of long filaments. A new peak emerges at short lengths in the presence of the old peak previously formed during the convection phase. As the dynamics proceed, the new peak dominates as the old peak disappears. The transition phase, induced by fragmentation, takes hours depending on the fragmentation rates. At the steady state, the filament assembly resembles a Poisson-like distribution, but skewed to the left.

The dynamics of the monomer pool is shown in Figure 3.4 (left). During the early dynamics, the monomer pool is depleted rapidly due to the emergence of new filaments and fast monomer addition at filament ends. The monomer pool decreases to the lowest concentration at around 30 secs, which corresponds to the transition point between the convective phase and subsequent length redistribution phase. After the transition, the monomer pool gradually increases until it approaches the steady state. The gradual increase of the monomer pool is presumably due to the recycling of fragmentation-generated short filaments to monomers. We note that the monomer pool is slightly above the critical concentration, which we predicted earlier in (3.7). The time evolution of the filament mean length is shown in Figure 3.4 (right). The filaments see a rapid growth during the convective phase, and then exhibit a gradual shrinking in average length. The shortening of filament lengths at large times are mainly due to fragmentation, as we will see in next section.

3.4.2 Temporal evolution of filament mean length

As the convective phase of filament growth resembles that of the nucleation-elongation model, we focus on the dynamic length changes in the late slow length redistribution phase. We have

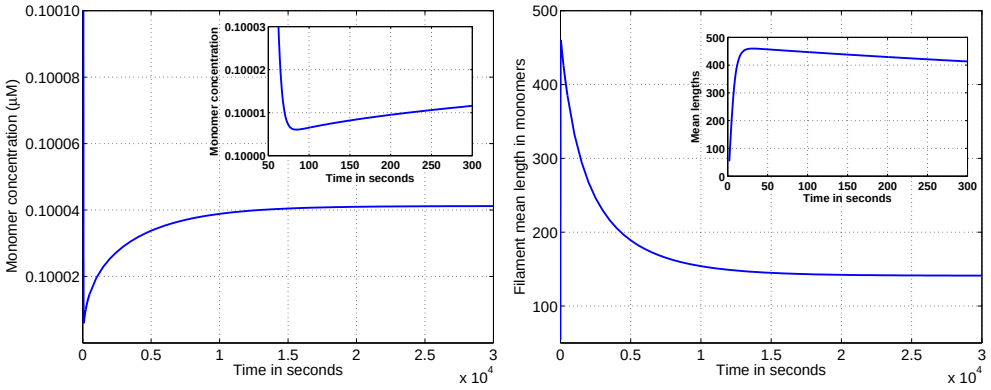

Figure 3.4: The time evolution of monomer pool and filament mean length. The fragmentation rate is set to be $k_f = 10^{-6}$ s^{-1}. The insets are enlargements of the early dynamics of the filament polymerization.

the rate of change of filament mean length as follows

$$\frac{d}{dt}\left(\frac{\sum_{i=4}^{N} ic_i}{\sum_{i=4}^{N} c_i}\right) = -\frac{\sum_{i=4}^{N} ic_i}{(\sum_{i=4}^{N} c_i)^2} * \frac{d}{dt}\left(\sum_{i=4}^{N} c_i\right) + \frac{1}{\sum_{i=4}^{N} c_i} * \frac{d}{dt}\left(\sum_{i=4}^{N} ic_i\right) \tag{3.10}$$

and the system (3.1) gives

$$\frac{d}{dt}\left(\sum_{i=4}^{N} c_i\right) = k_f \sum_{i=4}^{N}(i-7)\, c_i + (J_4 + 2k_f c_4) \tag{3.11}$$

$$\begin{aligned}\frac{d}{dt}\left(\sum_{i=4}^{N} ic_i\right) &= (k^+c_1 - k^- - 10k_f)\sum_{i=4}^{N} c_i \\ &\quad + \left(3J_4 + 6k_f c_4 + k^+c_1c_3 - k^+c_1c_N\right)\end{aligned} \tag{3.12}$$

Define the instantaneous average filament length as

$$\bar{l}(t) = \sum_{i=4}^{N} ic_i / \sum_{i=4}^{N} c_i \tag{3.13}$$

then (3.10) becomes

$$\frac{d\bar{l}}{dt} = (k^+c_1 - k^-) - k_f(\bar{l}-2)(\bar{l}-5) + T_3, \tag{3.14}$$

where the last term

$$T_3 = -\left(\sum_{i=4}^{N} c_i\right)^{-1} \left[(\bar{l}-4)k^+c_1c_3 - (\bar{l}-3)(k^- - 2k_f)c_4 + k^+c_1c_N\right] \quad (3.15)$$

$$\approx -(k^+c_1c_3 - k^-c_4)\,\bar{l}/\sum_{i=4}^{N} c_i = \bar{l} * (-J_4)/\sum_{i=4}^{N} c_i \quad (3.16)$$

The approximation in (3.16) holds, since (i) the average length at any time is orders of magnitude larger than unity (i.e. $\bar{l} \gg 1$), and (ii) the filament depolymerization rate is greater than fragmentation rate (i.e. $k^- \gg k_f$). Thus one has

$$\frac{d\bar{l}}{dt} \approx \underbrace{-\,k_f\,\bar{l}^2}_{\text{Term I}} + \underbrace{\bar{l} * (-J_4)/\sum_{i=4}^{N} c_i}_{\text{Term II}} + \underbrace{(k^+c_1 - k^-)}_{\text{Term III}} \quad (3.17)$$

From (3.17) we conclude that the dynamic change of filament mean length is controlled by three processes. First, fragmentation tends to shorten filament lengths and increase the total filament number, whereas the total concentration of F-actin remains unchanged. The contribution of fragmentation to the mean length change is represented by Term I. Term II denotes the mean length change influenced by the boundary condition where tetrameres depolymerize and becomes trimers. Since trimers are not included in the calculation of filament mean length as defined in (3.13), the loss of tetramers by depolymerization simply decreases the total filament number, which thus contributes to the increase of mean length. The filament length is also affected by the endwise polymerization, and the mean length change due to this process is represented by Term III.

The evolution of the magnititudes of Term I, II and III is depicted in Figure 3.5. We observe that during the early dynamics Term III decays rapidly, whereas Term I increases slowly. The decay of Term III is due to the decrease of monomer pool, which is consumed by fast filament polymerization. The effect of fragmentation on mean length change, represented by Term I, becomes significant as filaments grow longer. However, Term III is larger than Term I, thus the endwise polymerization is dominant among these processes affecting filament lengths. This explains why the early dynamics of filament polymerization in the presence of fragmentation

is indistinguishable from that without fragmentation. Around 30 seconds, the length increase resulting from endwise monomer addition is balanced by the fragmentation-caused length shortening. This is consistent with the cease of filament growth at the end of convective phase around 30 seconds as shown in Figure 3.3. After that, the fragmentation is the dominant process and filament length decreases. We notice that both Term II and III are approximately constant at large times, but Term III relatively small compare to Term II. This indicates that the contribution of endwise polymerization to the mean length change is relatively small during the length redistribution phase. Strikingly, at the steady state the shortening of filament mean length induced by fragmentation is compensated largely by the length increase due to the loss of filaments via depolymerization of tetramers instead of endwise polymerization. Our quantitative analysis on the steady state implies that fragmentation induces length shortening mainly by increasing filament populations without a significant change on the total F-actin concentration. Simultaneously, the depolymerization of tetramers into trimers reduces the filament population, and it counteracts the expansion of filament population resulted from fragmentation. To balance the loss of F-actin due to depolymerization of tetramers, trimers are recyled to the monomer pool, which in turn feeds polymerization at filament ends. Therefore, a non-vanishing actin flux cycle exists accompanying the steady state of filament polymerization in the presence of fragmentation. We conclude that at the steady steady fragmentation induces a significant reduction in the filament mean length, which is largely counteracted by the filament loss via tetramer depolymerization. The length increase by the endwise polymerization at the steady state is relatively small compared with the above two factors.

Since Term II and III are stablized faster than Term III as suggested in the numerical simulation (see Figure 3.5), suppose that Term II and III are stable at time t_0 and the filament mean length is $\bar{l}(t_0)$. At large times the evolution of filament mean length can be approximated by

$$\frac{d\bar{l}}{dt} = -k_f\, \bar{l}^2 + g \tag{3.18}$$

where the constant g is the sum of Term II and III as in (3.17). Because the rate of change of

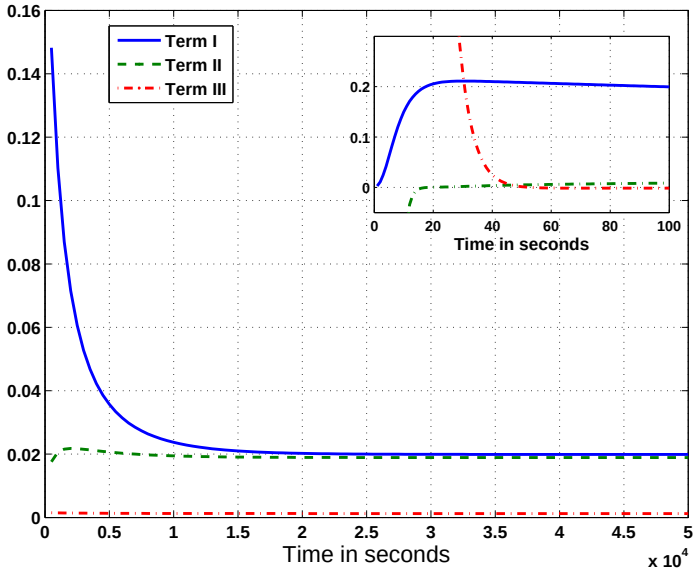

Figure 3.5: The contributions of three processes to the dynamics of filament mean length. The terms I, II and III are defined in equation (3.17).

filament mean length vanishes at the steady state, we have $g = k_f\ \bar{l}_0^2$, where $\bar{l}_0$ is the steady-state filament mean length. The general solution to (3.18) is a hyperbolic tangent function of time t as

$$\bar{l}(t) \quad = \quad \bar{l}_0 \cdot \tanh\left[k_f \bar{l}_0 \cdot t + C\right] \tag{3.19}$$

where the constant C is determined by the initial condition

$$\bar{l}(t_0) \quad = \quad \bar{l}_0 \cdot \tanh(C) \tag{3.20}$$

The prediction of mean length as in (3.18) is compared with the dynamic filament length directly solved from the full system (3.1), and the comparison is shown in Figure 3.6. For the fragmentation rate of 10^{-6} s^{-1}, the mean length can be accurately predicted by (3.19) after 200 secs of filament polymerization, which is short after the convective phase. Therefore, the mean length of filament evolves obeying (3.18) at the slow phase of filament length redistribution.

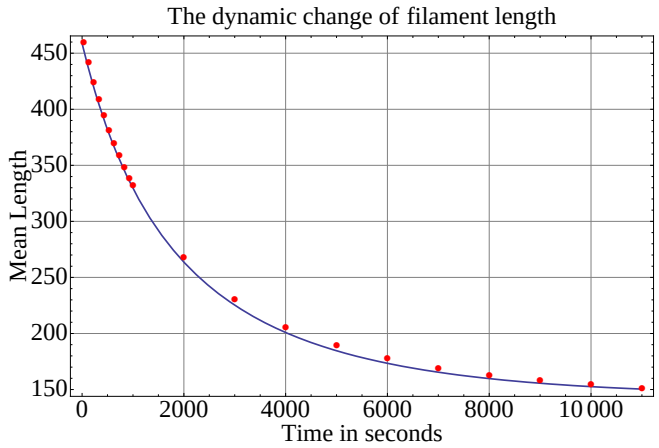

Figure 3.6: The dynamics of average length of actin filaments under the fragmentation of rate $k_f = 10^{-6}$ s^{-1}. Blue line represents the theoretical prediction according to (3.19), whereas the red dots show the mean length of actin filaments at discrete time points from the simulations of the full system (3.1).

3.5 A continuum approximation of fragmentation

In this section, we investigate the filament length dynamics in the continuum point of view. The validity of the continuum model is based on the fact that the increment size, δ, of a subunit is orders of magnitude smaller compared to the length of a typical filament. In the discrete model, a filament length is denoted by an integer, n, which is the number of subunits in the filament. A continuum filament has a continuous length, x, in the real space. The length in one view is related to the other by $x = n\ \delta$.

The discrete model of filament lengths reads

$$\begin{aligned} \frac{dc_n(t)}{dt} &= (k^+c_1c_{n-1} - k^-c_n) - (k^+c_1c_n - k^-c_{n-1}) \\ &\quad -(n-3)\ k_f\ c_n + k_f \sum_{i=n+2}^{\infty} c_i \end{aligned} \tag{3.21}$$

which in the continuum form is given by

$$\begin{aligned} \frac{\partial c(x,t)}{\partial t} &= -(k^+c_1 - k^-)\ \delta\ \frac{\partial c(x,t)}{\partial x} + \frac{k^+c_1 + k^-}{2}\ \delta^2\ \frac{\partial^2 c(x,t)}{\partial x^2} \\ &\quad -\frac{x\ k_f}{\delta}c(x,t) + \frac{2k_f}{\delta}\int_x^{\infty} c(s,t)ds + \mathcal{O}(\delta^3) \end{aligned} \tag{3.22}$$

By ignoring the higher order term, we have

$$\begin{aligned}\frac{\partial c(x,t)}{\partial t} &= -v\,\frac{\partial c(x,t)}{\partial x} + D\,\frac{\partial^2 c(x,t)}{\partial x^2} \\ &\quad -K_f\,x\,c(x,t) + 2K_f\int_x^\infty c(s,t)ds \end{aligned} \tag{3.23}$$

where $v = (k^+c_1 - k^-)\delta$, $D = (k^+c_1 + k^-)\delta^2/2$, and $K_f = k_f/\delta$.

Since the early phase of actin dynamics in the presence of fragmentation is similar to that in the nucleation-elongation model, we will apply the continuum approach only to the slow length redistribution phase. At this phase, the monomer pool is very close to the critical concentration, thus we assume the convective term vanishes, i.e. $v = 0$. Hence the equation becomes

$$\frac{\partial c(x,t)}{\partial t} = D\,\frac{\partial^2 c(x,t)}{\partial x^2} - K_f\,x\,c(x,t) + 2K_f\int_x^\infty c(s,t)ds \tag{3.24}$$

We also know that the amount of filament seeds is negligible due to the fast equilibration of nucleation pathway. The filament with infinite length has zero population size due to mass conservation condition of the system. We have the boundary conditions as

$$c(0,t) = c(\infty,t) = 0 \tag{3.25}$$

The dynamic and steady-state solution of (3.24) and (3.25) has been investigated in the literature [17]. Here we foucs on how the steady state of the continuum model reveals the features on the steady-state distribution of the discrete model (3.1). At the steady state, all rates of change of concentrations vanish, thus the continuum model becomes

$$D\,\frac{\partial^3 c(x)}{\partial x^3} - K_f\,x\,\frac{\partial c(x)}{\partial x} - 3\,K_f\,c(x) = 0 \tag{3.26}$$

$$c(0) = c(\infty) = 0 \tag{3.27}$$

where $D = \delta^2 k^-$, and $K_f = k_f/\delta$. By introducing a new length scale and changing variables

$$x \to x/X_0, \quad X_0 = (D/K_f)^{\frac{1}{3}} \tag{3.28}$$

we obtain a dimensionless form of the equation

$$\frac{\partial^3 u(x)}{\partial x^3} - x\,\frac{\partial u(x)}{\partial x} - 3\,u(x) = 0 \tag{3.29}$$

$$u(0) = u(\infty) = 0 \tag{3.30}$$

The linear equation of u can be solved analytically by the method of Fourier transformation [17], and a general non-vanishing solution is

$$u(x) = \sqrt{\frac{x^3}{3}} K_{1/3}\left(\frac{2x^{3/2}}{3}\right), (x > 0) \tag{3.31}$$

where $K_\nu(z)$ is the modified Bessel function of second kind, which solves

$$z^2\frac{d^2y}{dz^2} + z\frac{dy}{dz} - (z^2 + \nu^2)y = 0. \tag{3.32}$$

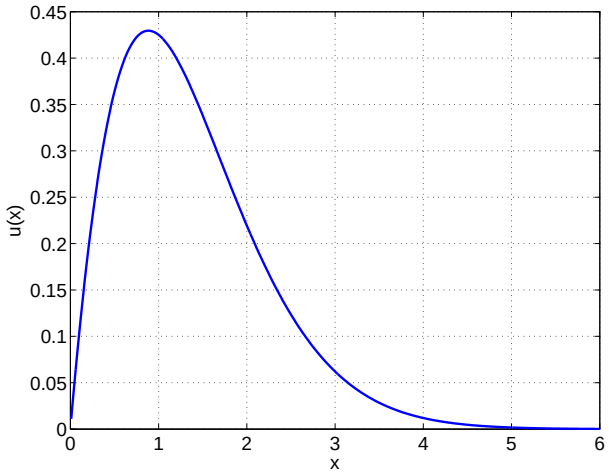

Figure 3.7: The curve of $u(x)$. The function $u(x)$ is defined as in (3.31).

The function $u(x)$ has a unimodal shape and skewed to the left as shown in Figure 3.7. A length distribution similar to $u(x)$ is called a distribution of Bessel type [17]. Therefore, the continuum model predicts a universal Bessel-type distribution of actin filament in the presence of fragmentation. The steady-state length distribution of Bessel type is the consequence of the combined diffusion process and uniform fragmentation process. No matter how weak the fragmentation activity, the steady state is a Bessel-type distribution. This is distinct from the nucleation-elongation model, where the slowly-evolving unimodal distribution eventually relaxes to an exponential one.

The steady-state solution of the continuum model accurately predicts that of the discrete

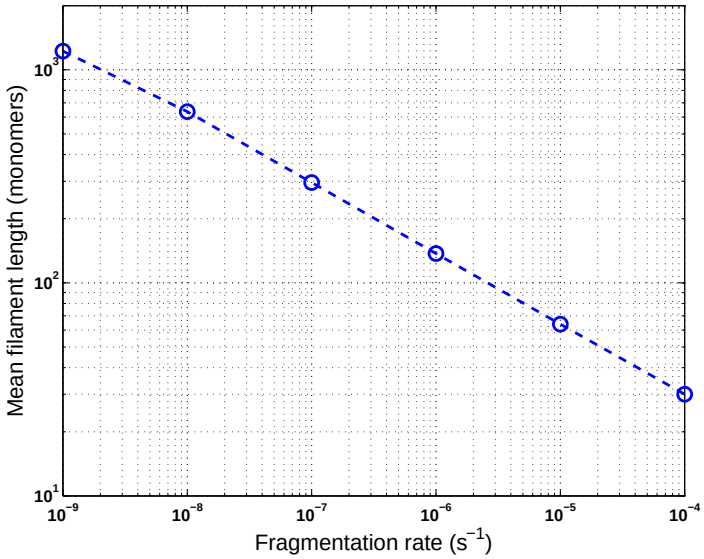

Figure 3.8: The dependence of filament mean length on the fragmentation activities.

model under various fragmentation rates, as depicted in Figure 3.2. We observed that the continuum model perfectly predicts the steady-state distribution at low fragmentation rates. As the fragmentation rate gets higher, the steady-state distribution predicted by the continuum model deviates slightly from that of the discrete model. We postulate that at high levels of fragmentation the actin flux becomes significant in the discrete model, but the continuum model does not include this effect.

In addition, the continuum model predicts the same Bessel-type distribution at various fragmentation rates up to a scaling facotr of $\sqrt[3]{D/K_f}$. With the other kinetic constants fixed, the mean length of actin filament is a power function of fragmentation rate. In particular, the average lengths ($\bar{L}$) under fragmentation rates of k_{f1} and k_{f2} are related to each other by

$$\bar{L}(k_{f1})/\bar{L}(k_{f2}) = \sqrt[3]{\frac{k_{f2}}{k_{f1}}}. \tag{3.33}$$

So when the fragmentation rate decreases by an order of magnitude, the mean filament length increases by a factor of $\sqrt[3]{10}$. This relationship between mean length and the fragmentation rate is consistent with simulation results of the discrete model as shown in Figure 3.8.

Chapter 4

Actin dynamics in the presence of profilin proteins

4.1 Introduction

Profilin has been shown to participate in many cellular activities including signal transduction, cytoskeleton organization, and gene expression [36]. An extensive effort has been directed to the research of how profilin regulates the dynamics of the actin cytoskeleton in motile cells [37, 38, 39, 40]. Investigators confirmed that profilin protein affects actin filament dynamics in at least two ways. One is via the interaction with G-actin and filament barbed ends so that profilin shuttles actin monomers onto filament barbed ends [41, 42, 43]. However, it remains controversial if profilin promotes actin filament polymerization [44]. On the other hand, profilin might enhance filament dynamics by accelerating the nucleotide exchange on G-ADP thus to feed filament ends with plenty G-ATP [45, 46, 47]. But there is a disagreement in the literature on whether ATP hydrolysis of F-actin is directly coupled to profilin-actin polymerization [44, 48].

In this chapter we investigate the profilin influence in the first aspect, and leave the probe of second possible action of profilin to a later chapter. Here the actin proteins associated with

distinct nucleotide types are not distinguished. Instead we view all the kinetic constants as effective rates averaging over all nucleotide types. A deterministic model on the profilin-actin interaction is first formulated, then theoretical and numerical model analysis follows to unveil the regulatory impact of profilin on the dynamics and steady state of the actin filament polymerization.

4.2 Model description

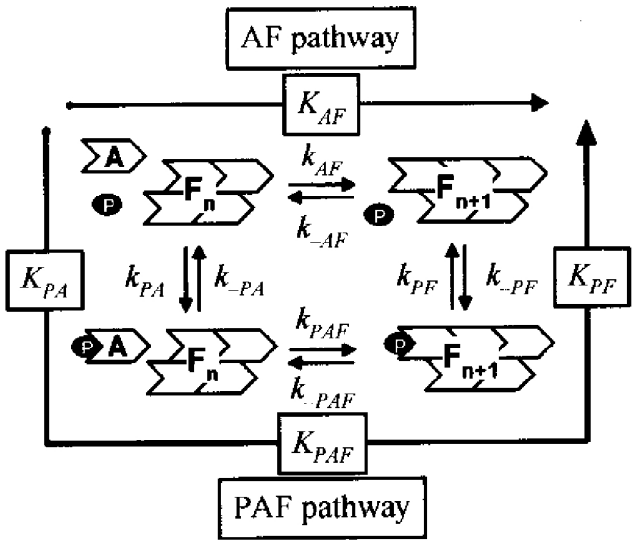

Figure 4.1: A schematic of barbed-end polymerization of an actin filament in the presence of profilin protein [46]. The letter **P** denotes a profilin protein, whereas the letters **A** and **F** represent the monomeric and filamentous form of actin protein.

Profilin regulates filament growth mainly through its interactions with actin monomers and filament ends. Profilin does not participate in the pointed-end dynamics, but only with the dynamics at the barbed end. How profilin exactly binds to the barbed end remains unclear. Most kinetic models in the literature assumed that only one profilin protein can bind to the barded end at the terminal subunit [41, 44, 46], whereas a recent model proposed that profilin binds to both the terminal and penultimate subunits of the barbed end [48]. However, the structural model

of actin filament indicated that the binding of profilin to the penultimate subunit is sterically inhibited by the terminal actin subunit [49]. We adopt the kinetic model of filament polymerization whereby profilin binds only to the terminal subunit of one strand of the double-stranded filament, as depicted in Figure 4.1. At a barbed end, the actin polymerization is done via two pathways: the AF pathway whereby actin monomer directly adds to the barbed end, and the PAF pathway whereby the addition of the profilin-actin complex onto the barbed end is followed by the dissociation of profilin from it [46]. The chemical reactions involved are as follows

$$\mathrm{M} + \mathrm{M} \underset{k_1^-}{\overset{k_1^+}{\rightleftarrows}} \mathrm{F}_2, \quad \mathrm{F}_2 + \mathrm{M} \underset{k_2^-}{\overset{k_2^+}{\rightleftarrows}} \mathrm{F}_3, \quad \mathrm{F}_n + \mathrm{M} \underset{k^-}{\overset{k^+}{\rightleftarrows}} \mathrm{F}_{n+1} \tag{4.1}$$

$$\mathrm{F}_n + \mathrm{P} \underset{k_{PF}^-}{\overset{k_{PF}^+}{\rightleftarrows}} \mathrm{PF}_n, \quad \mathrm{F}_n + \mathrm{PM} \underset{k_{PAF}^-}{\overset{k_{PAF}^+}{\rightleftarrows}} \mathrm{PF}_{n+1}, \quad \mathrm{PF}_n + \mathrm{M} \underset{k_p^-}{\overset{k_p^+}{\rightleftarrows}} \mathrm{PF}_{n+1} \tag{4.2}$$

$$\mathrm{P} + \mathrm{M} \underset{k_{PA}^-}{\overset{k_{PA}^+}{\rightleftarrows}} \mathrm{PM} \tag{4.3}$$

We observe that the kinetic rate constants vary in a large range in the literature. Both actin and profilin display cell-type-specific and organism-type-specific kinetics. The existence of several isoforms of actin and profilin adds to the complexity. We thus choose the parameters following these well-established criteria [41, 42, 46]: **(i)** profilin favors the binding for G-actin than for barbed ends; **(ii)** profilin-G-actin dissociates from barbed ends 4-6 fold faster than G-actin does; and **(iii)** the profilin-actin complex adds to the barbed end no faster than G-actin. For all simulations of this deterministic model, except otherwise specified, the parameters in Table 4.1 are adopted.

4.3 Theoretical analysis

4.3.1 Profilin slows the initial filament elongation

Since profilin reacts rapidly with the barbed end, filaments are swiftly switching between a profilin-capped state and profilin-free uncapped state during elongation. We thus assume the

Table 4.1: The kinetic rate constants used in the deterministic model of actin filament polymerization in the presence of profilin

Symbol	Definition	Value	Reference
k_1^+	On-rate of monomer to dimer	$10\ \mu\text{M}^{-1}\ \text{s}^{-1}$	[31]
k_1^-	Off-rate of monomer to dimer	$10^6\ \text{s}^{-1}$	[31]
k_2^+	On-rate of dimer to trimer	$10\ \mu\text{M}^{-1}\ \text{s}^{-1}$	[31]
k_2^-	Off-rate of dimer to trimer	$10^3\ \text{s}^{-1}$	[31]
k_b^+	On-rate of G-actin at the barbed end	$7.4\ \mu\text{M}^{-1}\ \text{s}^{-1}$	[4]
k_b^-	Off-rate of G-actin at the barbed end	$0.8\ \text{s}^{-1}$	[4]
k_p^+	On-rate of G-actin at the pointed end	$0.56\ \mu\text{M}^{-1}\ \text{s}^{-1}$	[4]
k_p^-	Off-rate of G-actin at the pointed end	$0.44\ \text{s}^{-1}$	[4]
k_{PA}^+	Association rate of profilin with G-actin	$15\ \mu\text{M}^{-1}\ \text{s}^{-1}$	[4]
k_{PA}^-	Dissociation rate of profilin with G-actin	$1\ \text{s}^{-1}$	[4]
k_{PF}^+	On-rate of profilin at the barbed end	$15\ \mu\text{M}^{-1}\ \text{s}^{-1}$	
k_{PF}^-	Off-rate of profilin at the barbed end	$300\ \text{s}^{-1}$	
k_{PAF}^+	On-rate of profilin-actin at the barbed end	$7.4\ \mu\text{M}^{-1}\ \text{s}^{-1}$	
k_{PAF}^-	Off-rate of profilin-actin at the barbed end	$4.44\ \text{s}^{-1}$	

fractions of filaments arrested in the uncapped and capped state are q and $1-q$, respectively. Let the populations of profilin-associated and free filaments be $[PF]$ and $[F]$. Thus one has

$$q = \frac{[F]}{[F]+[PF]}\ , \qquad 1-q = \frac{[PF]}{[F]+[PF]} \tag{4.4}$$

According to the polymer theory, the elongation rate of a filament with both ends uncapped by profilin but in a solution that contains profilin is

$$J_u = (k_b^+ + k_p^+)[A] - (k_b^- + k_p^-) + k_{PAF}^+[PA], \tag{4.5}$$

whereas a filament with its barbed end capped by profilin the rate becomes

$$J_c = k_p^+[A] - k_p^- - k_{PAF}^- \tag{4.6}$$

On average, a filament is elongating at the rate

$$\begin{aligned} J &= q\, J_u + (1-q)\, J_c \\ &= q\left(k_b^+([A]+[PA]) - k_b^-\right) + \left(k_p^+[A] - k_p^-\right) \\ &\qquad -q(k_b^+ - k_{PAF}^+)[PA] - (1-q)k_{PAF}^- \end{aligned} \tag{4.7}$$

Without profilin, a filament will elongate at a rate of

$$J_0 = \left(k_b^+[A]_0 - k_b^-\right) + \left(k_p^+[A]_0 - k_p^-\right) \tag{4.8}$$

where the initial monomer concentration, $[A]_0$, is the same as the case with profilin, i.e. $[A]_0 = [A] + [PA]$. By observing that the on-rate of profilin-actin complex is no greater than that of G-actin at the barbed end (i.e. $k_{PAF}^+ \leq k_b^+$), one can prove from (4.8)

$$J < \left(k_b^+[A]_0 - k_b^-\right) + \left(k_p^+[A]_0 - k_p^-\right) = J_0 \tag{4.9}$$

This implies that when a fraction of the actin monomers are bound to profilin filament elongation is initially slowed down. The above argument shows clearly the mechanism behind it. Profilin sequesters actin monomer thus greatly reducing the free G-actin pool which contributes to the pointed-end elongation. The association of profilin with barbed ends also makes less free barbed ends available for G-actin addition. Furthermore, profilin-actin complexes release from the barbed end faster than G-actin.

4.3.2 The steady-state filament length distribution

The previous nucleation-elongation model of pure actin filament predicted an exponential profile of the steady-state length distribution. What then is the shape of the length profile in the presence of profilin? To answer this question, we regard the inter-conversion of filaments of all lengths as a network of first-order chemical reactions as below

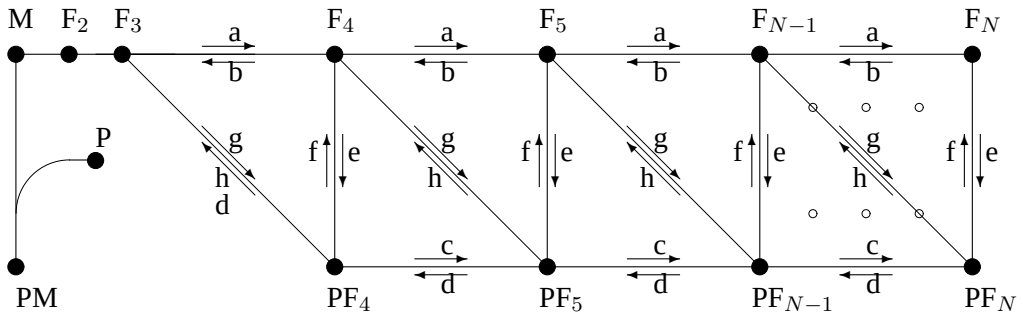

where the forward and backward reaction rates are denoted as

$$a = k^{+}[A], \qquad c = k_p^{+}[A], \qquad e = k_{PF}^{+}[P], \qquad g = k_{PAF}^{+}[PA],$$
$$b = k^{-}, \qquad d = k_p^{-}, \qquad f = k_{PF}^{-}, \qquad h = k_{PAF}^{-}.$$

Suppose the concentrations of F_n and PF_n are x_n and y_n, repectively. We construct two vectors to represent the concentrations of uncapped and capped filaments as

$$\begin{cases} \vec{x} = ([F_4], [F_5], \ldots, [F_N]) \\ \vec{y} = ([PF_4], [PF_5], \ldots, [PF_N]) \end{cases}$$

where N is the upper limit we post on the filament lengths. Since the concentrations of all filaments are constant at the steady state, for trimers we have

$$0 = \frac{dx_3}{dt} = -(a+g)x_3 + b\ x_4 + (d+h)y_4 \tag{4.10}$$

and for uncapped filaments

$$\begin{cases} 0 = \dfrac{dx_4}{dt} = a\ x_3 - (a+b+e+g)x_4 + b\ x_5 + f\ y_4 + h\ y_5 \\ 0 = \dfrac{dx_n}{dt} = a\ x_{n-1} - (a+b+e+g)x_n + b\ x_{n+1} + f\ y_n + h\ y_{n+1}, \quad (4 < n < N) \\ 0 = \dfrac{dx_N}{dt} = a\ x_{N-1} - (b+e)x_N + f\ y_N \end{cases} \tag{4.11}$$

and for capped filaments

$$\begin{cases} 0 = \dfrac{dy_4}{dt} = g\ x_3 + e\ x_4 - (c+d+f+h)y_4 + d\ y_5 \\ 0 = \dfrac{dx_n}{dt} = g\ x_{n-1} + e\ x_n + c\ y_{n-1} - (c+d+f+h)y_n + d\ y_{n+1}, \quad (4 < n < N) \\ 0 = \dfrac{dx_N}{dt} = c\ y_{N-1} - (d+f+h)y_N \end{cases} \tag{4.12}$$

Solving x_3 from equation (4.10) and plugging it into (4.11)-(4.12) results in

$$\begin{cases} A\vec{x} + B\vec{y} = 0 \\ C\vec{x} + D\vec{y} = 0 \end{cases} \tag{4.13}$$

where A, B, C and D are the following rate matrices

$$A = \begin{pmatrix} -(a+g+e+bg/(a+g)) & b & & & & \\ a & -(a+b+g+e) & b & & & \\ & & \vdots & & & \\ & & a & -(a+b+g+e) & b & \\ & & & a & -(b+e) \end{pmatrix}$$

$$D = \begin{pmatrix} -(c+f+\frac{a(d+h)}{a+g}) & d & & & & \\ c & -(c+d+f+h) & d & & & \\ & & \vdots & & & \\ & & c & -(c+d+f+h) & d & \\ & & & c & -(d+f+h) \end{pmatrix}$$

$$B = \begin{pmatrix} f+\frac{a(d+h)}{a+g} & h & & \\ & f & h & \\ & & \vdots & \\ & & f & h \\ & & & f \end{pmatrix}, \quad C = \begin{pmatrix} e+\frac{bg}{a+g} & & & \\ g & e & & \\ & \vdots & & \\ & g & e & \\ & & g & e \end{pmatrix}$$

From (4.13) one gets

$$\begin{cases} \vec{y} = -B^{-1}A\vec{x} \\ \vec{x} = -C^{-1}D\vec{y} \end{cases} \tag{4.14}$$

and further has

$$\begin{cases} (C^{-1}DB^{-1}A - I)\ \vec{x} = 0 \\ (B^{-1}AC^{-1}D - I)\ \vec{y} = 0 \end{cases} \tag{4.15}$$

Though it is difficult to obtain an explicit analytic solution from (4.15), the well-structured matrices enable us to estimate $\vec{x}$ and $\vec{y}$. The inverse of the matrix B is

$$B^{-1} = \begin{pmatrix} u^{-1} & -u^{-1}v & -u^{-1}\,v^2 & \dots & (-1)^{n-1}u^{-1}\,v^{n-1} \\ & 1/f & -v/f & \dots & (-1)^{n-1}v^{n-2}/f \\ & & 1/f & \dots & (-1)^{n-1}v^{n-3}/f \\ & & & \dots & \\ & & & & 1/f \end{pmatrix}$$

where $u = f + a(d+h)/(a+g)$ and $v = h/f$. Note that

$$f^{-1} = 1/k^{-}_{PF} \ll 1, \quad h/f = k^{-}_{PAF}/k^{-}_{PF} \ll 1$$

we approximate the inverse of B by its diagonal part only. Thus we solve

$$\vec{y} = -B^{-1}A\ \vec{x} = R_1\ \vec{x} \tag{4.16}$$

where

$$R_1 = \begin{pmatrix} \frac{a+g+e}{u} + \frac{bg}{u(a+g)} & \frac{-b}{u} & & & & \\ -a/f & w/f & -b/f & & & \\ & -a/f & w/f & -b/f & & \\ & & & \ddots & & \\ & & & -a/f & w/f & -b/f \\ & & & & -a/f & (b+e)/f \end{pmatrix}$$

where $w = a + b + g + e$. If we further assume that $x_{n+1} - x_n \ll x_n$ for $3 < n < N$, equation (4.16) is approximated by

$$\vec{y} \approx R_2 \, \vec{x} \tag{4.17}$$

where

$$R_2 = \begin{pmatrix} \frac{a+g+e}{u} - \frac{ab}{u(a+g)} & & & & \\ & (g+e)/f & & & \\ & & \ddots & & \\ & & & (g+e)/f & \\ & & & & (b+e-a)/f \end{pmatrix}$$

The approximation (4.17) predicts that the number of profilin-capped filament of all lengths is proportional to the number of uncapped filaments with a fixed ratio except for y_4 and y_N. In particular, the ratio is

$$s = \frac{g+e}{f} = \frac{k^+_{PAF}[PA] + k^+_{PF}[P]}{k^-_{PF}}$$

Therefore, in each cell of the reaction network as depicted below, the steady state requires

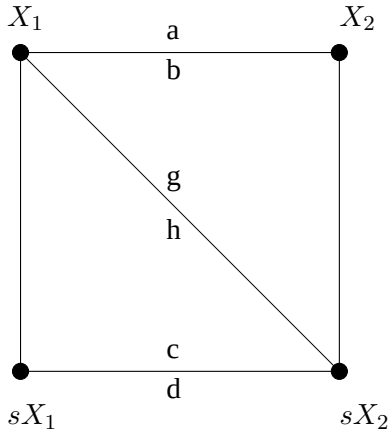

a zero flux from (X_1, sX_1) to (X_2, sX_2), which in turn suggests

$$X_2 = \frac{a + g + cs}{b + (d + h)s} X_1$$

This implies that the profilin would produce exponential distributions for both profilin-capped and profilin-free filaments, and the distributions differ approximately by a scaling factor

$$r = \frac{a + g + cs}{b + (d + h)s}.$$

4.3.3 The steady state of various protein populations

As shown in the previous section, the steady-state concentrations of actin, profilin and profilin-actin complex is important to determine the profile of filament length. To obtain the steady state of these and other filament quantities, we group all the proteins into five populations as

$$\begin{cases} [A] = \text{the population of free G-actin} \\ [P] = \text{the population of free profilin} \\ [PA] = \text{the population of profilin-G-actin complexes} \\ [F] = \text{the population of profilin-free filaments} \\ [PF] = \text{the population of profilin-associated filaments} \end{cases} \tag{4.18}$$

The dynamics of these populations is governed by

$$\begin{aligned} \frac{d[A]}{dt} &= -(k_p^+[A] - k_p^-)[PF] - (k_{PA}^+[P][A] - k_{PA}^-[PA]) \\ &\qquad + \left(-(k_b^+ + k_p^+)[A] + (k_b^- + k_p^-)\right)[F] \qquad (4.19) \\ \frac{d[P]}{dt} &= -k_{PF}^+[P][F] + k_{PF}^-[PF] - k_{PA}^+[P][A] + k_{PA}^-[PA] \qquad (4.20) \\ &\triangleq -J_{PF} - J_{PA} \\ \frac{d[PA]}{dt} &= k_{PA}^+[P][A] - k_{PA}^-[PA] - k_{PAF}^+[PA][F] + k_{PAF}^-[PF] \qquad (4.21) \\ &\triangleq J_{PA} - J_{PAF} \\ \frac{d[F]}{dt} &= -k_{PF}^+[P][F] + k_{PF}^-[PF] - k_{PAF}^+[PA][F] + k_{PAF}^-[PF] \qquad (4.22) \\ &\triangleq -J_{PF} - J_{PAF} \\ \frac{d[PF]}{dt} &= -\frac{d[F]}{dt} \qquad (4.23) \end{aligned}$$

where J_{PA}, J_{PF}, J_{PAF} are the fluxes among the five protein populations. The conservation conditions read as

$$[F_{tot}] = [F] + [PF] \tag{4.24}$$

$$[P_{tot}] = [P] + [PA] + [PF] \tag{4.25}$$

By introducing the fraction of uncapped filaments as $x = [F]/F_{tot}$, one solves the steady state of the system (4.19)-(4.23)

$$\begin{aligned}
[P] &= \frac{k^-_{PF} + k^-_{PAF} + k^+_{PAF}(P_{tot} - F_{tot})}{k^+_{PAF} - k^+_{PF}} \\
&\quad + \frac{k^-_{PF} + k^-_{PAF}}{k^+_{PF} - k^+_{PAF}} \cdot \frac{1}{x} - \frac{k^+_{PAF} F_{tot}}{k^+_{PF} - k^+_{PAF}} \cdot x
\end{aligned} \tag{4.26}$$

$$\begin{aligned}
[A] &= \frac{1}{(k^+_p + k^+_b x) F_{tot}} \\
&\quad \cdot \Bigg\{ \left((k^-_p - k^-_{PF} -) + \frac{k^-_{PF} + k^-_{PAF}}{k^+_{PF} - k^+_{PAF}} \cdot k^+_{PF} \right) F_{tot} \\
&\quad + \left(k^-_b + k^-_{PF} + \frac{k^-_{PF} + k^-_{PAF} + k^+_{PAF}(P_{tot} - F_{tot})}{k^+_{PAF} - k^+_{PF}} \cdot k^+_{PF} \right) \cdot F_{tot} \cdot x \\
&\quad + \frac{k^+_{PAF}}{k^+_{PAF} - k^+_{PF}} \cdot k^+_{PF} \cdot F^2_{tot} \cdot x^2 \Bigg\}
\end{aligned} \tag{4.27}$$

where x is the solution of

$$\begin{aligned}
0 &= k^-_{PF} \cdot F_{tot} + k^-_{PA} \cdot (P_{tot} - F_{tot} - [P]) \\
&\quad + (k^-_{PA} - k^-_{PF}) \cdot F_{tot} \cdot x - k^+_{PF} \cdot F_{tot} \cdot [P] \cdot x - k^+_{PA} \cdot [P] \cdot [A]
\end{aligned} \tag{4.28}$$

Here x solves a fourth-order polynomial, but only one solution lies in the range $(0, 1)$. With all kinetic rate constants fixed, x depends only on two variables P_{tot} and F_{tot}, which are the external input in an experiment. All the five quantities in (4.18) can subsequently be determined as explicit functions of x.

We would like to point out that in general the fluxes among the five protein populations as defined in (4.19)-(4.23) will not vanish at the steady state. The force of these non-vanishing fluxes comes from the fact that the barbed end is thermodynamically distinct from the pointed

end, i.e. $k_p^-/k_p^+ \neq k_b^-/k_b^+$. Define the variable

$$Q = \frac{(k_b^-/k_b^+)\cdot(k_{PF}^-/k_{PF}^+)}{(k_{PA}^-/k_{PA}^+)\cdot(k_{PAF}^-/k_{PAF}^+)} \tag{4.29}$$

The polymerization square consisted of AF and PAF pathways as in Figure 4.1 is called thermodynamically balanced if and only if $Q = 1$ [44]. We notice that even with the pointed end blocked, i.e. $k_p^+ = k_p^- = 0$, the flux still exists provided the polymerization square is not thermodynamically balanced. An unbalanced polymerization square requires energy input such as ATP hydrolysis. $Q > 1$ implies the PAF pathway is preferred over the AF pathway, whereas $Q < 1$ means the reverse. One can show that with the pointed end sealed the flux vanishes only when the polymerization square is thermodynamically balanced. In our simulations, we use the set of rate constants in Table 4.1 where $Q = 54$, and the PAF pathway is favored.

4.4 Numerical results

4.4.1 Time evolution of profilin-regulated filament lengths

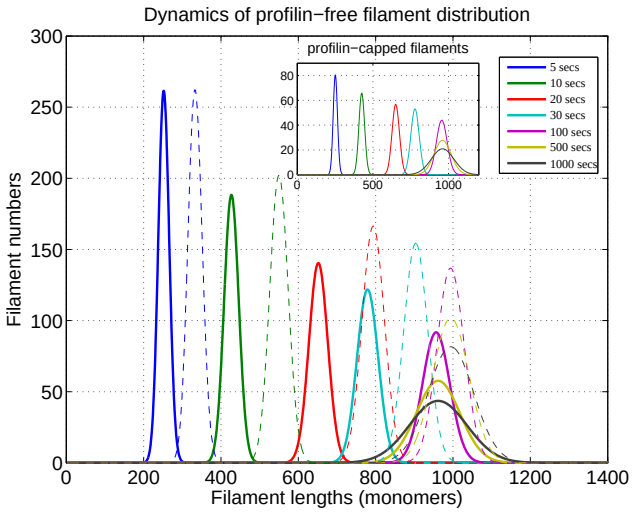

Figure 4.2: Time evolution of filament length distribution in the absence (dash lines) or in the presence (solid lines) of 10 μM profilin proteins.The inset depicts the length evolution of profilin-capped filaments.

Hereafter we will analyze the profilin-mediated filament polymerization in the light of simulation results. The same ODE solver applied in simulating the nucleation-elongation model is implemented to simulate the dynamics of profilin-actin interactions as described in (4.1)-(4.3). Unless otherwise specified, the default setting for all numerical simulations is 10 nM filaments in the mixture of 10 μM G-actin and 10 μM profilin. The solution volume is 2000 μm^3.

The temporal evolution of filament lengths as shown in Figure 4.2 reveals a similar bulk behavior as in the nucleation-elongation model where profilin is excluded. After the outset of polymerization, the filament profile sequentially undergoes a convective phase and a diffusive phase. In comparison with the filament growth without profilin, we observed a delayed shift of filament lengths to the right. This confirms our prediction as in (4.9) that profilin slows the filament elongation rate. With profilin the filament ceases its further growth at a mean length which is 30-50 subunits shorter than that without profilin. Therefore the profilin suppresses the extent of polymerization in addition to the elongation rate. During the entire time period we are interested in, the length profile of the profilin-capped filaments is similar to that of profilin-free filaments but with lower numbers.

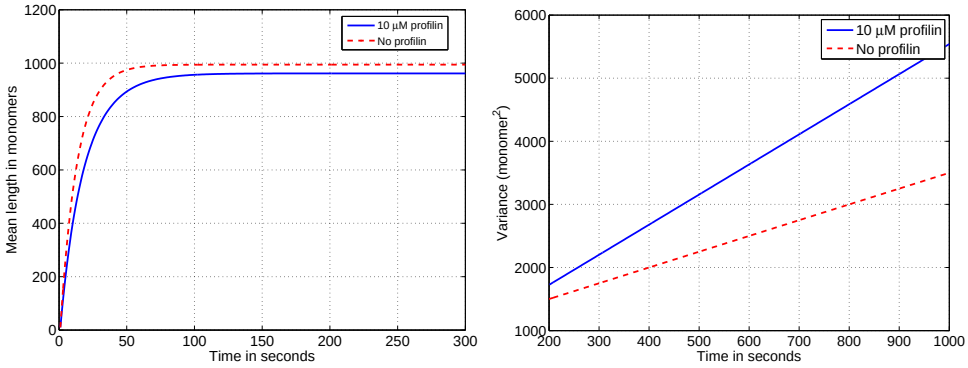

Figure 4.3: The evolution of first and second moments of filament length distribution in the absence and in the presence of profilin proteins.

The presence of profilin does not qualitatively alter the dynamics of filament polymerization. This is also confirmed by the comparison of the first and second moments of length distribution in both cases as in Figure 4.3. In both cases, the filament sees an initial rapid growth,

then elongation is slowed down as the G-actin pool is gradually depleted, and eventually the mean length is stabilized. The relaxation of the mean length to the steady state is slightly prolonged in the presence of profilin. After the mean length is stabilized, the variance of length distribution evolves linearly with respect to time. This implies the filaments are undergoing the process of length redistribution, which is characterized by a diffusion process. With the current model parameters, the diffusion of filament lengths is doubled under the regulation of profilin proteins, which will be explained later.

4.4.2 Protein concentrations and endwise polymerization

The numerical simulations also provide the temporal evolution of the protein populations such as profilin, uncomplexed G-actin and profilin-actin complex, which is difficult to be measured separately in experiments. The temporal profile of these proteins are displayed in Figure 4.4. Before the filament seeds are exposed to the monomers, the $10\ \mu$M G-actin is well mixed with profilin, and the latter arrests more than 90% actin monomers in the complexed state. After the filament seeds are added, the small fraction of free G-actin is rapidly depleted. The profilin-G-actin pool reduces exponentially when barbed-end polymerization follows the PAF pathway. As the polymerization proceeds, it frees up the profilin complexed with actin, and consequently raises the profilin pool.

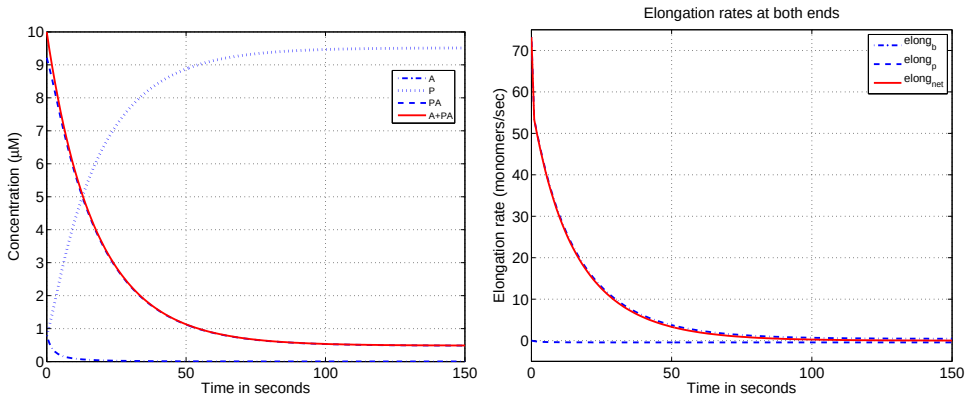

Figure 4.4: The actin pool and elongation rates at both ends during the dynamics.

Since profilin-actin does not involve pointed-end growth, the rapid depletion of free G-actin forces a nearly constant shrinkage at the pointed end as shown in Figure 4.4. The barbed end, however, exhibits significant elongation in the excess profilin-G-actin pool. A close look at the initial dynamics at both filament ends upon the addition of filament seeds is shown in Figure 4.5. The displayed elongation rate is an average rate among all filaments. In the absence of profilin, both ends are undergoing net elongation with faster growth at the barbed end than pointed end. However, the introduction of profilin effectively suppresses the growth of pointed end but preserves the elongation at the barbed end. The summed elongation of both ends in the presence profilin is less than the case with no profilin. This agrees with the analytic result as in (4.9) that the presence of profilin decreases the initial elongation rate of actin filaments.

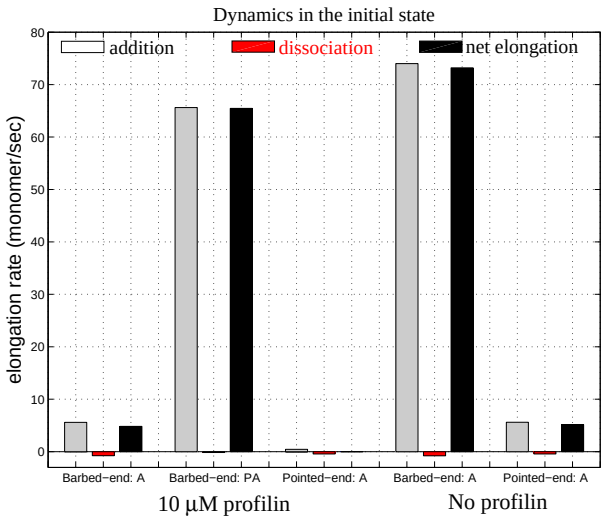

Figure 4.5: The initial polymerization at the barbed and pointed ends.

However, the dynamics at the diffusion regime are quite different from the initial state as shown in Figure 4.6. In the absence of profilin, G-actin polymerizes at the barbed end with a positive net elongation rate, where the net elongation rate is negative at the pointed end. The balanced net elongation at the two ends implies the filament is undergoing the treadmilling process. When a large pool of profilin is present, G-actin detaches from both ends and the addition

is negligible. The elongation of the barbed end is mainly due to the incorporation of profilin-actin complex. This suggests that at the steady state G-actin is below the critical concentrations of both ends. The profilin-actin-generated net elongation at the barbed end balances the depolymerization of G-actin at both ends. Thus at the diffusion phase monomers randomly add to and detach from the filament ends. For a filament with random monomer addition and deletion at rates of k_{on} and k_{off}, respectively, the diffusion rate is expected to be

$$D = (k_{on} + k_{off})/2 \tag{4.30}$$

Since the addition of G-actin is negligible at both ends, the total addition rate of 2.4 monomer/sec is due to the polymerization of profilin-actin at the barbed end. An equal amount depolymerization of filaments results from the detachment of both uncomplexed and complexed actin monomers at both ends. According to (4.30), the filament experiences a length fluctuation with the diffusion rate equal to the on-rate, which in the presence of profilin is 2.4 monomer^2/sec. This explains why the profilin promotes the length fluctuation in the diffusion phase as displayed in Figure 4.3.

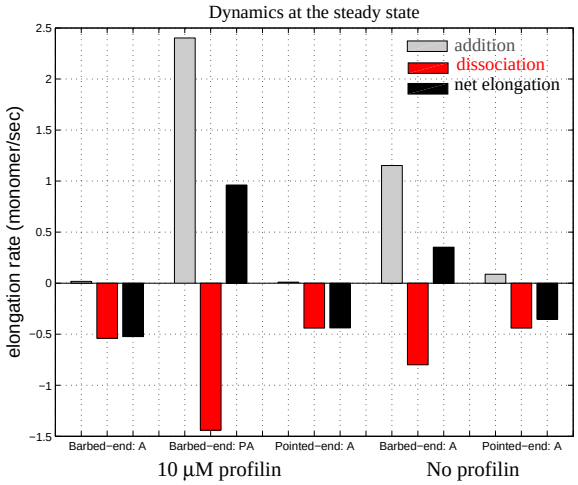

Figure 4.6: The steady-state dynamics at the barbed and pointed ends.

We now fix in space a filament of length 10 subunits and watch how the filament ends change their positions. The simulation result shown in Figure 4.7 confirms during early dynamics the

elongation of actin filaments slows down a little bit in the presence of profilin. However, profilin shuttles actin monomer to barbed ends for polymerization and prevents a massive pointed-end growth. Thus profilin facilitates filament treadmilling. This is important in a real cell when it has a large amount of free pointed ends and unpolymerized actin monomer in the cytoplasm.

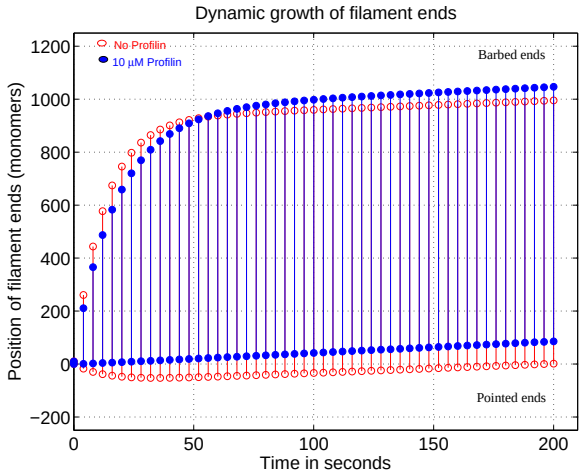

Figure 4.7: The treadmilling of filament in the absence (red) or in the presence (blue) of 10 μM profilin proteins.

Many *in vitro* assays use filament seeds with blocked pointed-ends, such as spectrin-actin seeds. We examined the statistics of barbed-end growth at the steady state in details shown in Figure 4.8. In the absence of profilin, the addition of G-actin at the barbed end is balanced by its dissociation with a rate of 0.8 monomer/sec. The introduce of profilin diminishes the addition of G-actin, and the polymerization of profilin-actin complex is balanced by the depolymerization of both actin and profilin-actin. A similar argument as above would show profilin amplifies the length fluctuation at the diffusion stage.

4.4.3 The dependence of protein concentrations on P_{tot}

In the following, we examine the dependence of steady-state quantities on the total profilin concentration accordingly to the theoretical prediction that result from (4.24)-(4.28). We numerically solve (4.24)-(4.28) in *Mathematica 6.0*. As the profilin concentration rises, the fraction of

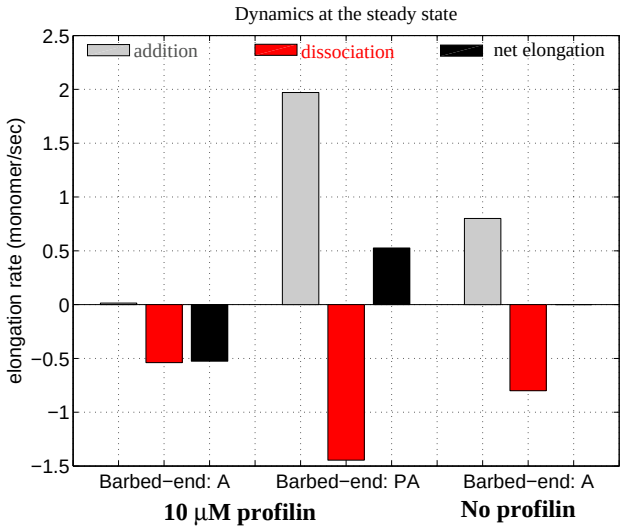

Figure 4.8: The statistics of steady-state polymerization at the barbed ends for filaments with blocked pointed end.

profilin-free filaments decreases as seen in Figure 4.9. About 35% filaments out of 10 nM have their barbed end capped in the presence of 10 μM profilin. At the steady state, the majority of profilin proteins are in the uncomplexed state. The fast equilibration between profilin and barbed end thus leads to an approximation of the ratio of uncapped filaments, x, as

$$x = \frac{K_{PF}}{K_{PF} + P_{tot}} \tag{4.31}$$

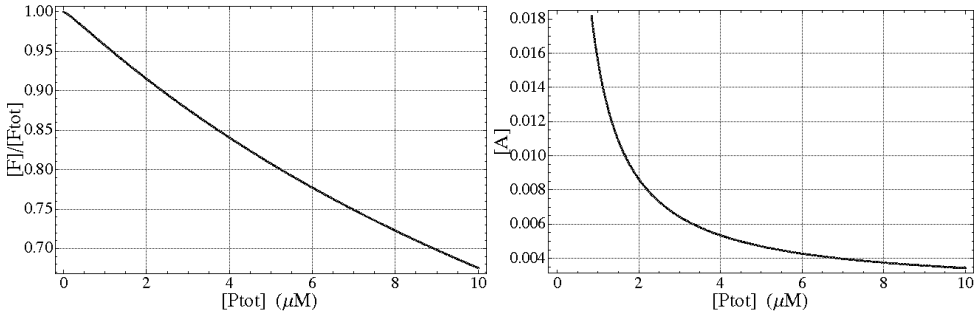

Figure 4.9: The dependence of profilin-free filament population and G-actin pool on total profilin concentration.

where K_{PF} is the equilibrium constant for the reaction of profilin binding to the barbed end. The above estimate of x matches very well with the prediction in (4.28). We discover that the steady-state G-actin pool drops dramatically with elevated profilin concentrations. At the steady state, the G-actin population shrinks to 0.0035 μM at 10 μM profilin, while it is of 0.156 μM without profilin. However, the level of unpolymerized actin pool, $[A]+[PA]$, increases linearly with profilin. The comparison of the actin and profilin-actin levels are displayed in Figure 4.10. It indicates that after a transition regime the profilin-actin level linearly increases, whereas G-actin concentration is negligible.

We performed numerical simulations on the full model as described in (4.1)-(4.3). The simulation result is compared to the prediction as in (4.24)-(4.28) at profilin concentrations of 0.001, 1, 5 and 10 μM. Our theoretical analysis correctly predicts the steady state of various actin sub-populations as shown on Figure 4.10.

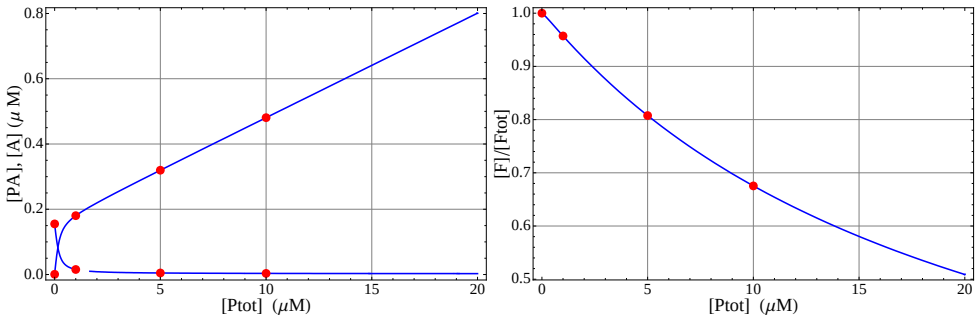

Figure 4.10: The dependence of unpolymerized actin and profilin-free filament population on total profilin concentration. The blue line is the prediction according to (4.24)-(4.28), whereas the red dots represent the simulation result on the profilin-mediated filament growth model as described in the text.

It is reported that the pointed-end depolymerization *in vivo* could be 10 fold higher than *in vitro* data. We deliberately raise the pointed-end off rate by 10 fold. Our result indicates that the fraction of uncapped filament at the steady state has no significant change, while the level of G-actin is raised 5 fold as seen in Figure 4.11. The linear relationship between the unpolymerized actin level and total profilin level remains, and the concentration of the unpolymerized actin protein is greatly increased with the elevated pointed-end kinetics as we compare Figure 4.11

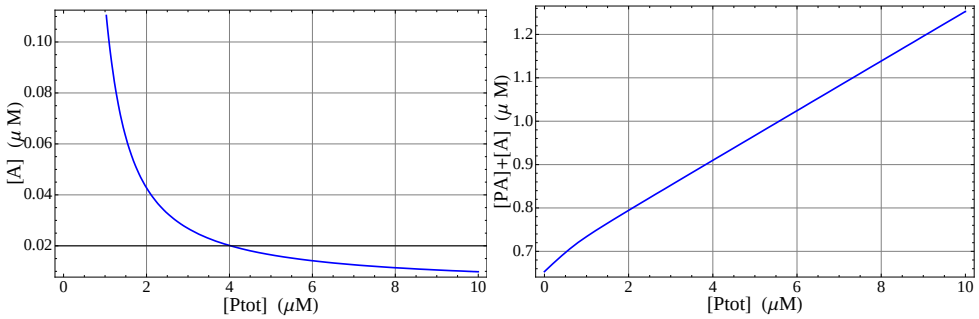

Figure 4.11: The dependence of G-actin and total unpolymerized actin on total profilin concentration. Here the pointed-end depolymerization is increased 10 fold.

and 4.10.

4.4.4 The dependence of protein concentrations on F_{tot}

As our analysis predicted, the steady state of the dynamics should also depends on the total filament number. We thus raise the filament number from 1 nM to 100 nM to examine the possible changes brought by the filament population. The numerical result reveals that both the levels of profilin-free filament and G-actin increase with increased filament numbers. On the contrary, our data indicates that the unpolymerized actin pool is reduced linearly with respect to the size of filament seeds. In spite of these changes, we note that the changes induced by the expanded filament population is extremely small. This indicates that the steady state of the system is less sensitive to the filament sizes than to the profilin concentrations. The reason is that the concentration of profilin greatly outnumbers the filament concentration.

Chapter 5

A stochastic approach to actin filament polymerization with profilin

5.1 Introduction

In Chapter 2 and 4, we investigated the actin dynamics from a deterministic point of view. There the actin monomers associated with different nucleotide types are not distinguished, and essentially a single actin state is assumed. This simplification prevents the examination on the nucleotide profile of a filament. The latter is important for the interaction of many actin-binding proteins with a filament. These include profilin, twinfilin, cofilin, Arp2/3 etc. The role of actin-bound nucleotides has been appreciated in explaining many actin-related phenomena, such as length fluctuation of a treadmilling filament [26], the biphasic behavior of filament growth in the presence of twinfilin [50], and actin-driven force generation [51, 52]. In this chapter, we focus on how actin-bound nucleotides influence the length and nucleotide profile of the filaments both in the absence and presence of profilin proteins.

For the pure actin dynamics, we adopt the kinetic model of filament polymerization proposed by Fujiwara *et al.* [8]. In this model, the actin monomers bound with ATP, ADP-Pi and ADP, bind reversibly with both filament ends, and the ATP-associated subunit in the filament

hydrolyzes its ATP randomly and subsequently releases the γ-phosphate. The Pi release rate of the terminal subunits at both ends are faster than that of the interior subunits. In the solution, G-ADP-Pi rapidly release its attached Pi, whereas G-ADP becomes G-ATP through the slow nucleotide exchange. For the actin dynamics in the presence of profilin, additional reactions between profilin, actin monomers and filaments are considered. For each actin state, profilin can complex with actin monomers and participate in the barbed-end polymerization as depicted in Figure 4.1. Profilin accelerates the nucleotide exchange on G-ADP when it binds to G-ADP. In the current model, we assume profilin binding at the barbed end does not affect the ATP hydrolysis and the subsequent Pi release. It remains controversial whether the binding of profilin to the barbed end interrupts the ATP hydrolysis and Pi release on the terminal subunit [48]. The kinetic rate constants applied in the simulations are listed in Table 5.1 and 5.2.

By distinguishing each subunit by its bound nucleotide, we will have a total 3^n possible configurations for a filament of length n. One would expect that the number of filaments with a particular length and nucleotide profile is extremely low, and the reactions on the filaments follow a random process. We thus model the actin dynamics using a stochastic approach. Monte Carlo methods are applied to generate the realizations of the underlying stochastic process. Specifically, for numerical simulations in this chapter we implement an efficient stochastic simulation algorithm developed by Matzavinos and Othmer [50]. The algorithm is modified from the direct method proposed earlier by Gillespie [54].

We present below the results of the stochastic simulations on the bulk dynamics of pure actin filaments first, and then the dynamics with profilin. The focus is on the dynamic length and nucleotide composition of filaments. We also compare the results of the stochastic models with the deterministic models in Chapter 2 and 4. In all simulations, the reactions are assumed to take place in the solution with a volume $500\ \mu\text{m}^3$. One realization is performed for each stochastic model, and then the statistics on the filament populations is done on the realization outcome.

Table 5.1: The kinetic rate constants used in the stochastic profilin-actin model

Symbol	Definition	Value	Ref.
k_{bA}^{+1}	G-ADP on-rate of at the barbed end	$2.9\ \mu\text{M}^{-1}\ \text{s}^{-1}$	[8]
k_{bA}^{+2}	G-ADP-Pi on-rate of at the barbed end	$3.4\ \mu\text{M}^{-1}\ \text{s}^{-1}$	[8]
k_{bA}^{+3}	G-ATP on-rate of at the barbed end	$11.6\ \mu\text{M}^{-1}\ \text{s}^{-1}$	[8]
k_{bA}^{-1}	G-ADP off-rate of at the barbed end	$5.4\ \text{s}^{-1}$	[8]
k_{bA}^{-2}	G-ADP-Pi off-rate of at the barbed end	$0.2\ \text{s}^{-1}$	[8]
k_{bA}^{-3}	G-ATP off-rate of at the barbed end	$1.4\ \text{s}^{-1}$	[8]
k_{pA}^{+1}	G-ADP on-rate of at the pointed end	$0.14\ \mu\text{M}^{-1}\ \text{s}^{-1}$	[8]
k_{pA}^{+2}	G-ADP-Pi on-rate of at the pointed end	$0.11\ \mu\text{M}^{-1}\ \text{s}^{-1}$	[8]
k_{pA}^{+3}	G-ATP on-rate of at the pointed end	$1.3\ \mu\text{M}^{-1}\ \text{s}^{-1}$	[8]
k_{pA}^{-1}	G-ADP off-rate of at the pointed end	$0.25\ \text{s}^{-1}$	[8]
k_{pA}^{-2}	G-ADP-Pi off-rate of at the pointed end	$0.02\ \text{s}^{-1}$	[8]
k_{pA}^{-3}	G-ATP off-rate of at the pointed end	$0.8\ \text{s}^{-1}$	[8]
k_{PAF}^{+1}	On-rate of profilin-G-ADP at the barbed end	$1.26\ \mu\text{M}^{-1}\ \text{s}^{-1}$	[46]
k_{PAF}^{+2}	On-rate of profilin-G-ADP-Pi at the barbed end	$9.0\ \mu\text{M}^{-1}\ \text{s}^{-1}$	[46]
k_{PAF}^{+3}	On-rate of profilin-G-ATP at the barbed end	$9.0\ \mu\text{M}^{-1}\ \text{s}^{-1}$	[46]
k_{PAF}^{-1}	Off-rate of profilin-G-ADP at the barbed end	$12.6\ \text{s}^{-1}$	[46]
k_{PAF}^{-2}	Off-rate of profilin-G-ADP-Pi at the barbed end	$5.5\ \text{s}^{-1}$	[46]
k_{PAF}^{-3}	Off-rate of profilin-G-ATP at the barbed end	$5.5\ \text{s}^{-1}$	[46]
k_{PF}^{+1}	On-rate of profilin binding to ADP-barbed end	$15.0\ \mu\text{M}^{-1}\ \text{s}^{-1}$	[46]
k_{PF}^{+2}	On-rate of profilin binding to ADP-Pi-barbed end	$15.0\ \mu\text{M}^{-1}\ \text{s}^{-1}$	[46]
k_{PF}^{+3}	On-rate of profilin binding to ATP-barbed end	$15.0\ \mu\text{M}^{-1}\ \text{s}^{-1}$	[46]
k_{PF}^{-1}	Off-rate of profilin binding to ADP-barbed end	$300.0\ \text{s}^{-1}$	[46]
k_{PF}^{-2}	Off-rate of profilin binding to ADP-Pi-barbed end	$300.0\ \text{s}^{-1}$	[46]
k_{PF}^{-3}	Off-rate of profilin binding to ATP-barbed end	$300.0\ \text{s}^{-1}$	[46]

Table 5.2: The kinetic rate constants used in the stochastic profilin-actin model (continued)

Symbol	Definition	Value	Ref.
k_{PA}^{+1}	On-rate of profilin binding to G-ADP	$15.0\ \mu\text{M}^{-1}\ \text{s}^{-1}$	[46]
k_{PA}^{+2}	On-rate of profilin binding to G-ADP-Pi	$15.0\ \mu\text{M}^{-1}\ \text{s}^{-1}$	[46]
k_{PA}^{+3}	On-rate of profilin binding to G-ATP	$15.0\ \mu\text{M}^{-1}\ \text{s}^{-1}$	[46]
k_{PA}^{-1}	Off-rate of profilin binding to G-ADP	$5.7\ \text{s}^{-1}$	[46]
k_{PA}^{-1}	Off-rate of profilin binding to G-ADP-Pi	$1.5\ \text{s}^{-1}$	[46]
k_{PA}^{-1}	Off-rate of profilin binding to G-ATP	$1.5\ \text{s}^{-1}$	[46]
r^h	Hydrolysis rate of ATP subunit	$0.3\ \text{s}^{-1}$	[8]
r^i	Pi release rate on internal actin subunits	$0.003\ \text{s}^{-1}$	[8]
r_b^i	Pi release rate at the barbed end	$2.0\ \text{s}^{-1}$	[8]
r_p^i	Pi release rate at the pointed end	$2.0\ \text{s}^{-1}$	[8]
h_{13}^A	Nucleotide exchange rate on G-ADP	$0.071(0.01)^a\ \text{s}^{-1}$	[53]
h_{21}^A	Pi release rate on G-ADP-Pi	$100.0\ \text{s}^{-1}$	
h_{13}^{PA}	Nucleotide exchange rate on profilin-G-ADP	$8.0\ \text{s}^{-1}$	[53]
h_{21}^{PA}	Pi release rate on profilin-G-ADP-Pi	$100.0\ \text{s}^{-1}$	

[a] For all simulations in Section 5.2, h_{13}^A=0.01 s^{-1}; in Section 5.3, h_{13}^A=0.071 s^{-1}.

5.2 Results of the stochastic model of pure actin dynamics

5.2.1 Dynamics of the filament length distribution

In the current stochastic model of pure actin dynamics, the reactions considered include the endwise polymerization of three actin types, the hydrolysis of ATP-actin and subsequent Pi release, and the nucleotide exchange of G-ADP as described in Section 5.1. The numerical experiment setting is: $10\ n$M filament seeds consisting uniformly of 10 ADP-subunits is to polymerize in a solution of $5\ \mu$M G-ATP. The nucleation of new filaments is negligible with existing filament seeds, thus in simulations filament nucleation is blocked.

Snapshots of the length distribution at discrete time points from one realization of the stochastic model are displayed in Figure 5.1. The fluctuating length distribution instead of a

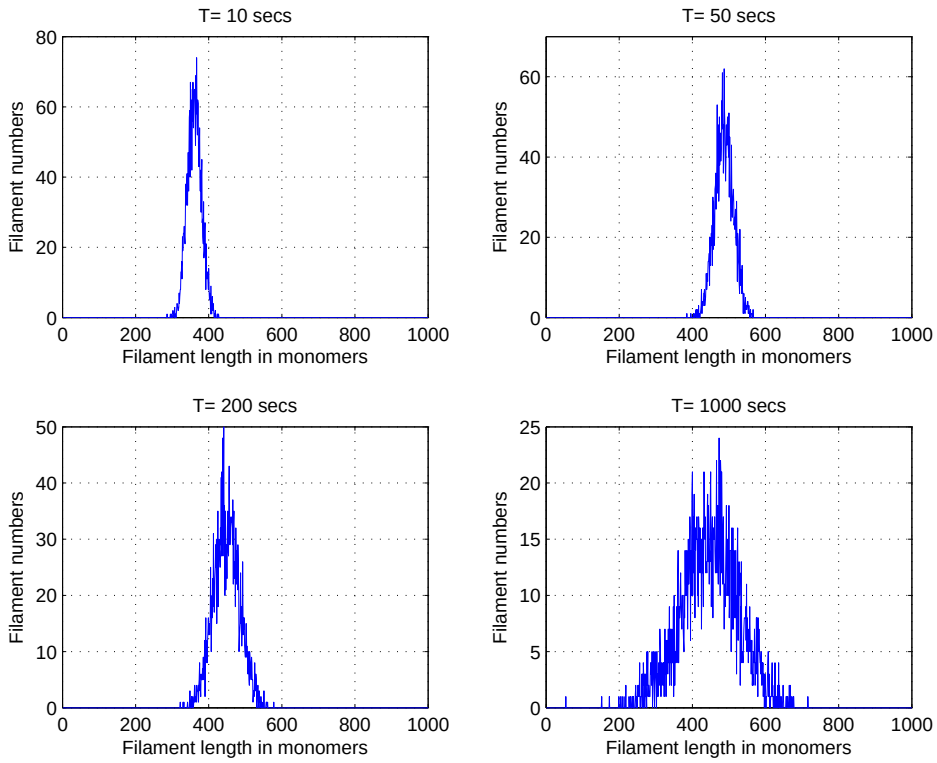

Figure 5.1: The temporal evolution of actin filament lengths.

smooth one is the signature of the stochastic model. The evolution of length distribution indicates that the filament length undergoes two sequential phases: convective phase and diffusive phase, which resembles that of the deterministic model discussed in Chapter 2. However, the stochastic model reveals a distinct feature as shown in Figure 5.2 (left). The average filament length initially increases and starts to decrease at about 40 secs until it eventually approaches a steady state after about 200 secs of polymerization. This overshoot behavior is not observed for the deterministic model.

The overshoot specific to the stochastic model can be explained in the light of the dynamics of each actin type. We track the change in amounts of three actin types as depicted in Figure 5.2 (right). G-ATP exhibits a rapid drop in concentration after the outset of polymerization, but G-ADP gradually accumulates in the solution due to the hydrolysis and depolymerization

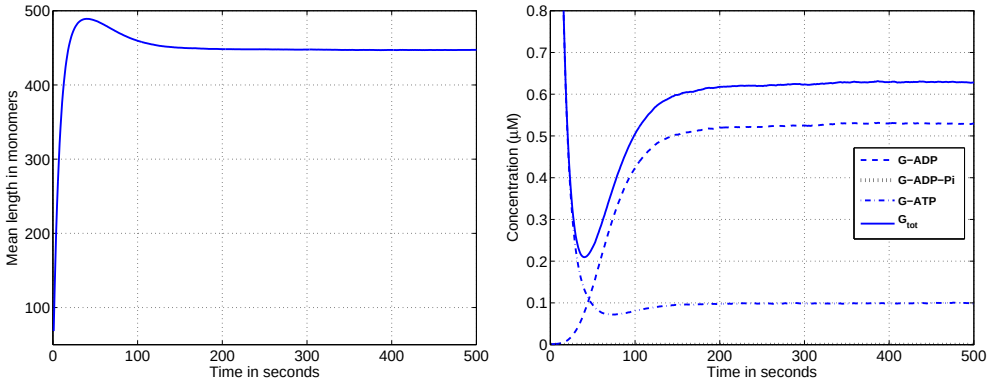

Figure 5.2: The dynamics of filament mean length and monomer pool from one realization of the stochastic model. The totoal G-actin concentration is the sum of all three actin species, and the concentration of G-ADP-Pi is negligible.

of G-ATP. The amount of G-ADP-Pi is too small to be detected. During the first 40 secs of polymerization, the total G-actin pool is decreasing, corresponding to the filament elongation at the convective phase as one sees in Figure 5.2 (left). After that, G-ATP sees a small undershoot and eventually relaxes to a resting level around 0.1 μM. However, the G-ADP pool continues to expand following a sigmoid curve before it approaches the steady state. Therefore, the G-actin pool exhibits a undershoot over 0.4 μM. This undershoot corresponds to the overshoot of the actin filament. We postulate that the accumulation of G-ADP pool is mainly due to both the massive depolymerization of G-ADP and G-ADP-Pi from a large number of filaments and the slow nucleotide exchange on G-ADP in the solution. At the steady state, G-ATP accounts for only 15% of the total G-actin pool as indicated in Figure 5.2 (right). This contradicts with the generally-held view that G-ATP is the dominant species in the G-actin pool. This thus emphasizes the importance of regulatory proteins, such as profilin, that accelerate the nucleotide exchange *in vivo*.

5.2.2 Dynamics of the nucleotide composition

In our stochastic simulation, we are able to sample one filament and examine the dynamics of nucleotide composition of the filament. A sample of tagged filament with its nucleotide profile

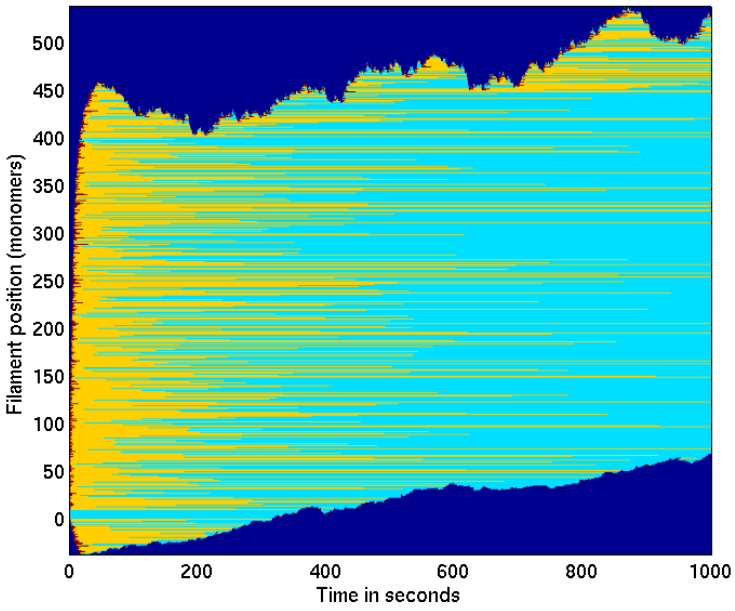

Figure 5.3: The evolution of nucleotide profile on a filament body. The filament is fixed in the space at some point. The upper boundary stands for the barbed end, whereas the lower represents the pointed end. The red denotes the subunit associated with ATP, yellow with ADP-Pi, and cyan with ADP.

during the dynamics is displayed in Figure 5.3. In the early stages of growth dynamics, both filament ends are capped by a short portion of ATP-associated subunits. Away from the two ends is a G-ADP-Pi portion. The ADP core is sanwiched by ADP-Pi subunits. This core is initiated by the filament seed. After 40 secs of polymerization, the pointed end starts to shrink gradually, but the shortening is intermittent due to occasional polymerization attributed to the stochastic nature of the reactions. However, the barbed end experiences a larger length fluctuation as shown in Figure 5.3. After the elogation phase, the filament body is exposed to more ADP due to the Pi release of ADP-Pi subunits. Eventually the filament body is mainly associated with ADP except a short region at the barbed end.

We also obtain the statistical nucleotide profile along the length as displayed in Figure 5.4. The probability of a particular nucleotide type, say ATP, of the n-th subunit from the

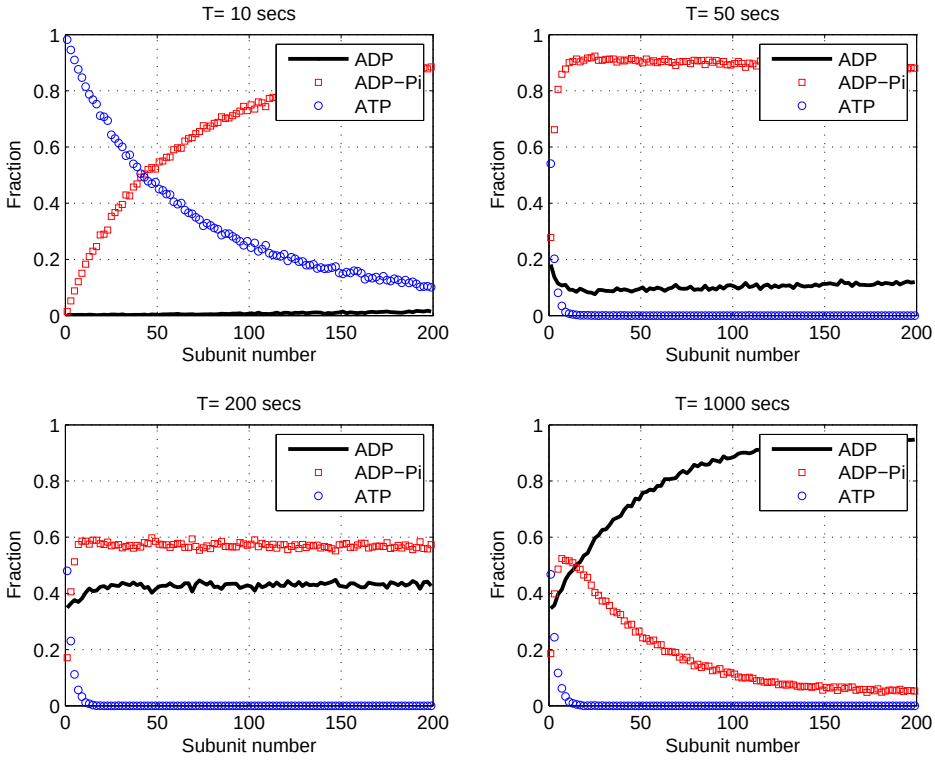

Figure 5.4: The statistical nucleotide profile of the filament population. The horizontal axis represents the position of a subunit counted from the barbed end. Only the profile on the first 200 subunits is plotted.

barbed end is calculated by dividing the number of filaments with ATP on the n-th subunit by the total filament number. This tells the probability of finding ATP in the n-th subunit. At the early phase of filament polymerization (e.g. 10 secs), the barbed-end region is capped by exponentially-decreasing distributed ATP and exponentially-increasing distributed ADP-Pi making the probability for ADP negligible. The tip is associated with ATP at a near 100% probability. At 50 secs, the barbed-end G-ATP is greatly reduced. The ATP is bound only with several subunits at the barbed end, and even at the tip its probability is less than 50 $\%$. The G-ADP-Pi profile is more uniform, since previously incorporated G-ATP hydrolyzes its ATP fast but still has its Pi due to the slow Pi release rate. At $T = 200$ secs, the probability of G-ADP-Pi decreases and that of G-ADP increases, due to the Pi release of G-ADP-Pi. At large times, the

G-ADP-Pi distribution evolved to be exponentially decreasing except in the close proximity to the barbed end. The cause of this exponential distribution of ADP-Pi profile remains unclear. The combination of filament treadmilling from the barbed end to pointed end and slow Pi release seems to lead to the steady-state profile [29]. However, simulations on filaments with a blocked pointed-end exhibit the same profile, which disagrees with the treadmilling-driven mechanism. We postulate that the length fluctuations of barbed ends could simply generate the exponential ADP-Pi profile. We point out that at the steady state ATP is found only within the first several subunits located at the barbed end. This may shed light on the contraversial question of whether ARP2/3 branches a daughter filament at the end of the mother filament or at the site close to the barbed end. Since ARP2/3 complex seems to preferentially bind to ATP-subunit of a mother filament, it would bind to the site, which is spatially very close to the barbed end. If the microscopy resolution is not high, one cannot tell if ARP2/3 binds to the barbed end or not.

5.2.3 Effect from the filament population

Since the accumulation of a large G-ADP pool is due to the depolymerization at filament ends, one would expect a reduced filament population may decrease the concentration of G-ADP. We thus purposely reduce the concentration of filament seeds from 10 nM to 1 nM and 0.1 nM, respectively. At reduced filament numbers, the monomer pool exhibits different dynamics as shown in Figure 5.5. For both filament concentrations, the G-ATP pools monotonically decreases and approaches a steady state at 0.14 μM. G-ADP populations accumulate gradually in the solution, but its level is below that of G-ATP. When the filament level is reduced to 1 nM, the equilibrium concentration of G-ADP is nearly half of that for G-ATP. A slight overshoot is observed. For 0.1 nM filaments, G-ADP pool further decreases to a steady state far below G-ATP. The overshoot of F-actin polymerization completely disappears. Thus, we conclude that a large pool of filament seeds produces a large G-ADP population when thte nucleotide exchange is slow, and this generates the overshoot of filament polymereization at the intermediate phase.

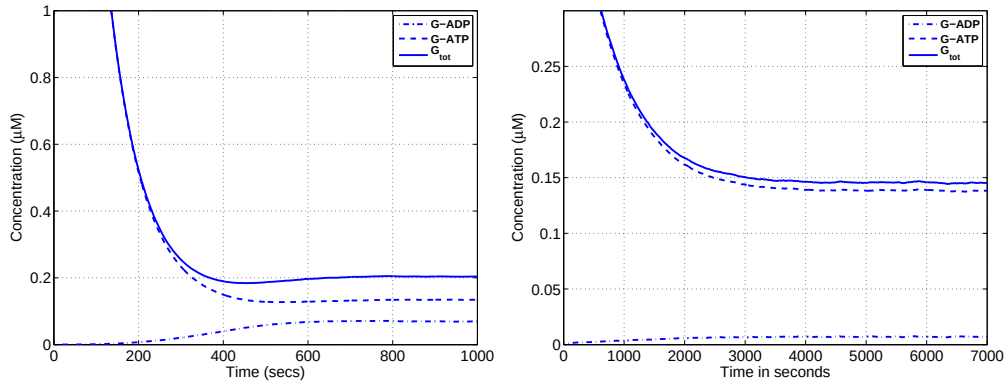

Figure 5.5: The dynamics of actin monomer pool with reduced filament seeds. The filament concentrations are of 1 nM (left) and 0.1 nM (right).

5.3 Results of the stochastic model of actin dynamics with profilin

In this section, we will probe the potential influence of profilin on the dynamics of lengths and nucleotide composition of the filaments. The kinetic model of actin dynamics in the presence of profilin is described in Section 5.1, and the kinetic rate constants applied in our stochastic simulations are listed in Table 5.1 and 5.2.

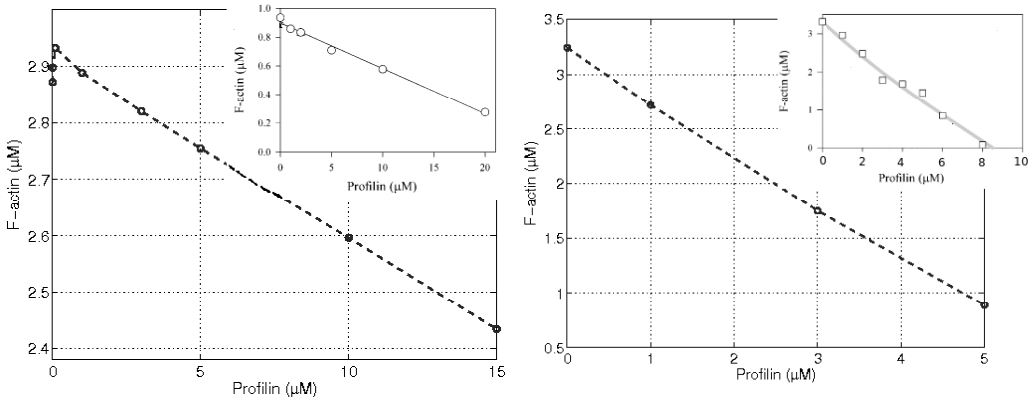

Figure 5.6: The steady-state F-actin concentrations for 10 nM filament seeds polymerizing in the solution of 3 μM ATP-actin (left) and 5 μM ADP-actin (right) mixed with varying profilin concentrations. The insets are the experimental data published by Kinosian et al. [46].

Before we analyze the simulation results of the profilin-mediated actin dynamics, we first

test our stochastic model and its parameters by comparing our simulation results with existing experimental data. Kinosian *et al.* performed the *in vitro* experiments where a number of aged filament seeds is mixed in the solution of either G-ATP alone with excess of nucleotide ATP or G-ADP alone with excess of ADP. They observed that the steady-state F-actin level linearly decreases with profilin concentrations [46] . We conducted numerical simulations similar to the *in vitro* assays, and let a pool of 10 nM filament seeds consisting uniformly of 10 ADP-subunits polymerize in the solution of either 3 μM G-ATP with excess of nucleotide ATP or 5 μM G-ADP with excess of nucleotide ADP. Numerical results show that our kinetic model reproduces the linear dependence of the concentration of F-actin on profilin as shown in Figure 5.6.

In the following, we investigate how profilin affects the actin filament polymerization. The default setting for our numerical simulations is: 10 nM filament seeds uniformly composed of 10 ADP-subunits are to polymerize in a 3 μM ATP-G-actin solution, which pre-mixed with varying levels of profilin.

5.3.1 Dynamics of G-actin and F-actin

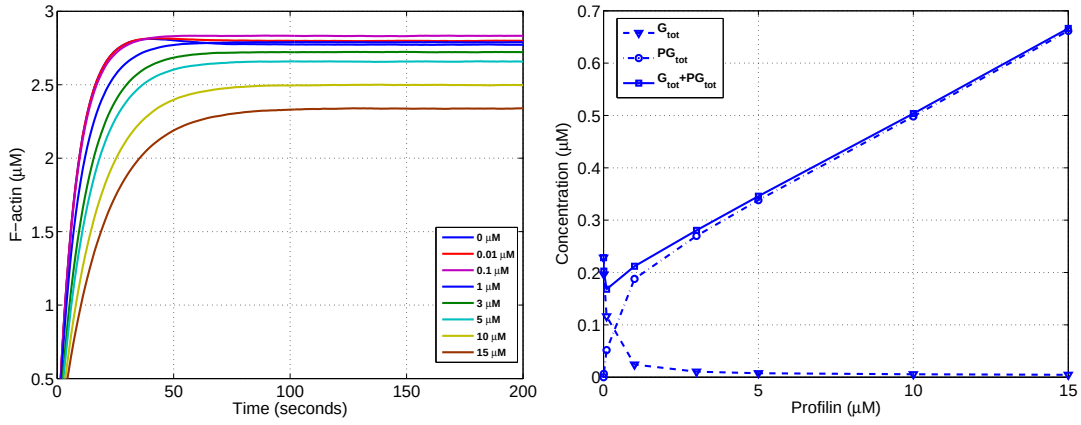

Figure 5.7: The dynamics of F-actin polymerization and steady-state monomer pool in the presence of profilin.

The temporal evolution of F-actin polymerization with varying profilin levels is shown in Figure 5.7 (left). As the result shows, without profilin the polymerization curve reveals two

distinct phases of filament growth: the convective phase and the diffusive phase. Between these phases is a transition phase characterized by the slight overshoot of F-actin. We have argued that this overshoot is attributed to the slow ADP-ATP exchange on G-ADP. With the introduction of profilin, the overshoot is suppressed, and completely disappears even at a small amount of profilin as 0.1 μM. This is consistent with that the binding to profilin accelerates the nucleotide exchange on G-ADP by at least 100 fold. This role of profilin as recharging G-ADP is important for the dynamics of actin cytoskeleton since *in vivo* a large number of filament ends are present and the depolymerization of G-ADP is significant. As profilin increases, the elongation of filaments is inhibited, which is reflected by smaller polymerization slopes at the convective phase. Furthermore, the extent of F-actin polymerization is reduced by increased concentrations of profilin, which resembles the deterministic model as we investigated in Chapter 4.

The suppression of F-actin polymerization by profilin is also reflected in the expansion of unpolymerized actin pool as shown in Figure 5.7 (right). Without profilin, the actin monomer pool rests at 0.23 μM at the steady state. As profilin level increases, the G-actin pool decreases. By contrast, the profilin-actin complex sees monotone increase. The total unpolymerized actin pool consisting of both free and profilin-complex actin monomers decreases with profilin when the total profilin level is below 0.1 μM. This is because profilin accelerates the refreshing of G-ADP to G-ATP, and thus promotes the F-actin polymerization. As the profilin concentration further increases, the total unpolymerized actin pool linearly increases. Therefore, profilin exhibits a biphasic effect on the F-actin polymerization: at low concentrations, profilin promotes the F-actin polymerization, while a large concentration of profilin attenuates the polymerization. This feature results from the dual roles of profilin as to boost the nucleotide exchange on G-ADP and to promote the actin depolymerization at the barbed end. At the barbed end, profilin-G-actin depolymerizes 4-6 fold faster than G-actin.

5.3.2 Filament treadmilling and length fluctuations

We further examine the filament treadmilling and length fluctuation by looking into the numbers of actin-involved reactions occurred at the barbed end at the steady state. For each reaction type,

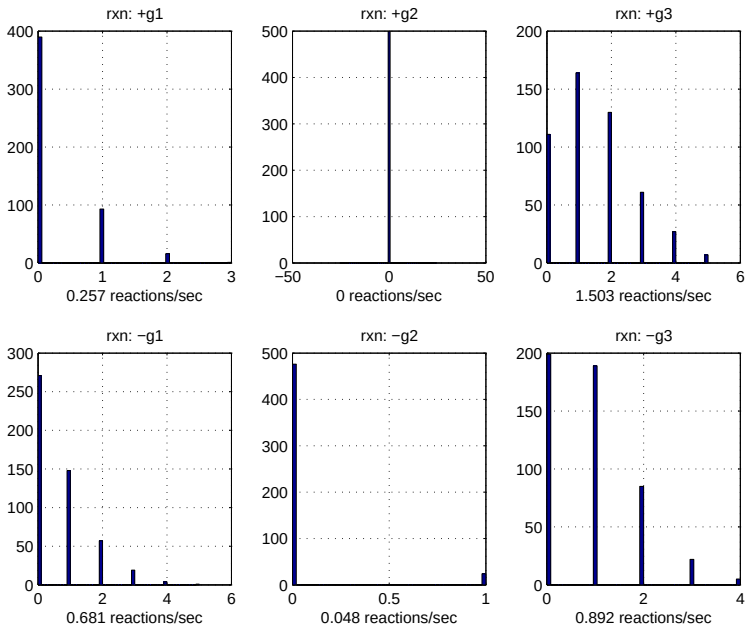

Figure 5.8: Histogram illustrating the number of barbed-end reaction firings. The letter g denotes actin monomer, where number $1, 2, 3$ encodes the nucleotide ADP, ADP-Pi and ATP, respectively. The plus and minus notation means the reaction is an addition or deletion reaction. For a tagged filament, the firing number for each reaction type is counted in consecutive 500 one-second time intervals. The average firing rate is calculated for each reaction type.

we count the numbers of its firing at a barbed end for one-second time intervals in the period of 500 seconds, and then obtain the firing rate by averaging them. As shown in Figure 5.8, at the steady state without profilin the dominant polymerization reaction is the addition of G-ATP, which fires at a rate 1.50 firings/sec. The G-ADP polymerization occurs at a low rate of 0.26 firings/sec, which only accounts for 15% of the total monomer additions. However, the depolymerization of G-ADP compares to that of G-ATP. The net elongation rate, which is the sum of addition rate minus the sum of off rates, is estimated to be 0.14 monomers/sec. This rate also represents the treadmilling speed of the filament, since the pointed-end shrinkage is balanced by the barbed-end elongation at the steady state. As discussed in the nucleation-elongation model, a barbed-end with the effective on- and off-rate of k_{on} and k_{off}, respectively, has a length diffusion rate constant of $D = (k_{on} + k_{off})/2$. The diffusion rate constant at the

barbed end can be approximated by the sum of firing rates of all reactions. Thus, the barbed end diffusion without profilin is estimated to be 1.69 monomer^2/sec. By introducing 15 μM profilin in the solution, the dominant polymerization occurring is ATP-bound profilin-actin, whereas the addition of other species is negligible, as the statistics show in Figure 5.9. ATP-associated profilin-actin dominates the depolymerization at a barbed end, and its firing rate is followed by detachment of G-ATP and profilin-bounded G-ADP-Pi. We estimated that the treadmilling rate is 0.36 monomer/sec, whereas the length diffusion rate constant is 3.37 monomer^2/sec. Thus profilin promotes the filament treadmilling and increases the length fluctuation at the barbed end.

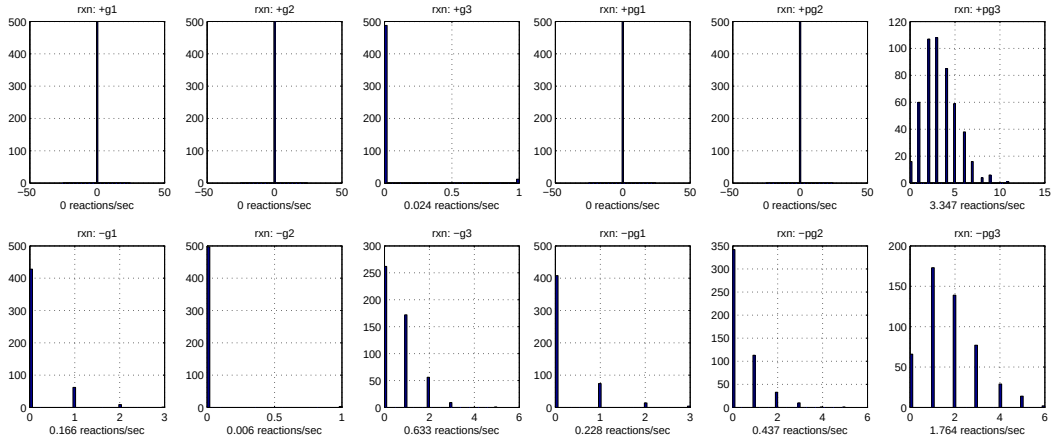

Figure 5.9: Histogram illustrating the number of barbed-end reaction firings. The letter g denotes actin monomer, p for profilin, where number $1, 2, 3$ encodes the nucleotide ADP, ADP-Pi and ATP, respectively. The plus and minus notations mean the reaction is an addition or deletion one. For a tagged filament, the firing numbers of each reaction type is counted in consecutive 500 one-second time intervals. The average firing rate is calculated for each reaction type.

5.3.3 Dynamics of filament nucleotide profile

To visualize the influence of profilin on the filament nucleotide profile, we track the dynamics of the nucleotide profile of a tagged filament in the absence and presence of profilin. The comparison can be seen in Figure 5.10. During the treadmilling stage, the filament polymerizing

in the presence of 15 μM profilin is slightly shorter than that without profilin. With profilin, nearly half of the filament body is associated with ATP/ADP-Pi. However, the filament is only capped by a short ATP/ADP-Pi portion at the barbed end without profilin. The effect of profilin on the statistical nucleotide profile at the steady state is shown in Figure 5.11. Two main changes on the nucleotide profiles are observed: i) the probability of ATP for terminal subunits increases by 10% with profilin; ii) the exponential decay of ADP-Pi profile is slowed by profilin, and the ADP-Pi portion extends deeper into the filament body. In our simulation, without profilin ADP-Pi can be observed with 50% of chance on the 30-th subunit deeper from the barbed end, whereas the 70-th subunit is found 50% bound to ADP-Pi in the presence of 15 μM profilin. We postulate that both elevated treadmilling and length fluctuation induced by profilin contribute to the decaying of ADP-Pi profile deeper into the filament body.

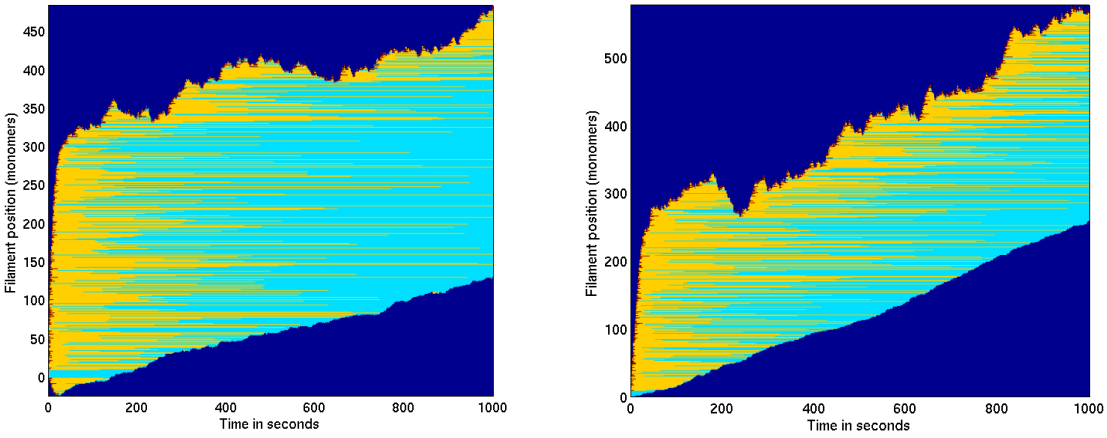

Figure 5.10: The time evolution of nucleotide profile of a tagged filament without profilin (left) and with 15 μM profilin (right).

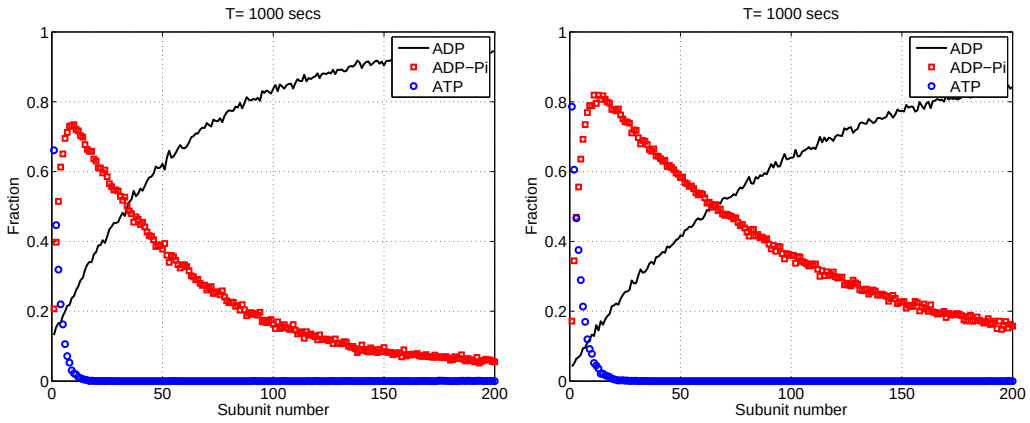

Figure 5.11: The statistics of nucleotide profiles of the filament population without profilin (left) and with 15 μM profilin (right).

Chapter 6

Large length fluctuations: a single-filament approach

6.1 Introduction

The complex dynamics of actin filament lengths has been investigated by two approaches. One approach is to focus on a large population of filaments in the solution. The other is to track the length fluctuations of single filament. The growth and length fluctuations of such individual filaments provides insight into the bulk filament dynamics. This single filament approach has been applied to understand the nature of filament polymerization [24] and polymerization-driven force generation [51, 55].

When a filament is immersed in a monomer pool, its length change will exhibit two distinct phases: the continuous elongation phase, and the diffusive phase. The polymerization of actin monomers associated with different nucleotides is often simplified as effective polymerization of single-state actin, where at any instant of time the polymerization rate is linearly related to the monomer concentration. The nucleation-elongation model predicted that the elongation rate is be

$$j(c) = k^{+}c - k^{-} \tag{6.1}$$

and the diffusion rate of the length fluctuation is

$$D(c) = \frac{1}{2}(k^+ c + k^-). \tag{6.2}$$

where c is the monomer concentration, and $k^\pm$ are the on- and off-rate constants of G-actin.

However, *in vitro* experiments challenge the above prediction by two remarkable observations: (i) the filament elongation curve exhibits a biphasic behavior in that the linear growth rate changes around the critical concentration [56]; (ii) around the critical concentration the measured diffusion rate constant, D, could be as high as $30 - 45$ times the prediction in (6.2) [24, 25]. In order to explain these discrepancies, we re-examine the dependence of monomer polymerization on its associated nucleotides. Actin monomer could change its associated nucleotide type during the polymerization course, and the nucleotide composition of a filament in turn influences the length changes. Vavylonis *et al.* [26] related the filament length fluctuations to the nucleotide state of the filament tip. They confirmed the biphasic growth behavior by differentiating three actin states. Furthermore, a tooth-shaped diffusion-concentration curve is obtained from the Monte Carlo simulations, and a 35-fold large length fluctuation occurring at a monomer concentration slightly below the critical value is theoretically predicted in a simple filament polymerization model where a filament with a long ADP core is polymerizing in the G-ATP pool. In Section 6.3.1, we re-investigate the same simple case by applying a more general multi-step side walk model. Other factors, such as filament buckling, paused polymerization and annealing, may also contribute the observed high length fluctuation [25, 28].

In this chapter, we will systematically explore the length dynamics of single filament by taking into account the differentiation of actin states. We will focus on the long-time behavior of the first and second moments of the filament length distribution, and different filament models are compared. A more general mathematical description of the filament length and underlying nucleotide composition is formulated at the end of this chapter.

6.2 The single-state filament model

In this section, we first examine the filament growth in a closed system, for which the total monomer is constant, and then in a fixed monomer bath. The F-actin has only single state, and its elongation is proportional to the monomer concentration.

Suppose only one sufficiently long filament is in the monomer pool of volume V_{ol}. The rate constants of monomer addition and removal are k^+ and k^-, respectively. Let $p(n,t)$ denote the probability of monomer pool having n subunits at time t, and let $P(n,t)$ be the probability of the filament having n subunits at time t. Since at any instant of time the sum of F-actin and G-actin is constant, the statistical properties of the single filament is reflected in those of the monomer pool. If the filament nucleation is ignored, then the master equation reads

$$\frac{dp(n,t)}{dt} = k^{*+}(n+1)p(n+1) + k^{*-}p(n-1) - k^{*+}np(n) - k^{*-}p(n) \tag{6.3}$$

where

$$k^{*+} = k^+/(\mathcal{N}_A V_{ol}), \quad k^{*-} = k^-$$

and $\mathcal{N}_A$ is the Avogadro's number.

The evolution of first and second moments, denoted as $M(t)$ and $V(t)$, then satisfies

$$\frac{dM(t)}{dt} = \frac{d\sum_n n\, p(n,t)}{dt} = -k^{*+}M(t) + k^{*-} \tag{6.4}$$

$$\frac{dV(t)}{dt} = \frac{d\sum_n n^2\, p(n,t)}{dt} = -2k^{*+}V(t) + (k^{*-} + 2k^{*-})M(t) + k^{*-} \tag{6.5}$$

At equilibrium, the first and second moments are

$$M(\infty) = k^{*-}/k^{*+}, \quad V(\infty) = (k^{*-}/k^{*+})^2 \tag{6.6}$$

Therefore, the variance of monomer numbers is

$$\sigma^2(\infty) = V(\infty) - M^2(\infty) = (k^-/k^+)(\mathcal{N}_A V_{ol}) \tag{6.7}$$

In addition, the monomer number at equilibrium is Poisson distributed as [57]

$$p(n) = \frac{1}{n!}\left[(\mathcal{N}_A V_{ol})k^-/k^+\right]^n e^{-(\mathcal{N}_A V)k^-/k^+} \tag{6.8}$$

Thus at large times, the monomer pool approaches a steady-state Poisson distribution. Accordingly, the filament length exhibits a Poisson distribution at long times. Eventually the mean and variance of the single filament are stable in the close system.

If we instead let a filament polymerize in a constant monomer bath of concentration c, and the probability of the filament having n subunits at time t is $P(n,t)$, then the master equation becomes

$$\frac{dP(n,t)}{dt} = k^+cP(n-1) + k^-P(n+1) - (k^+c + k^-)P(n) \tag{6.9}$$

The mean length evolves at rate

$$j(c) = \frac{dM(t)}{dt} = \frac{d\sum_n nP(n,t)}{dt} \quad = \quad k^+c - k^- \tag{6.10}$$

The second moment of $P(n,t)$ follows

$$\frac{dV}{dt} = \frac{d\sum_n n^2P(n,t)}{dt} \quad = \quad (k^+c + k^-) + 2\ EX\ (k^+c - k^-) \tag{6.11}$$

and therefore, the variance is

$$\sigma^2(t) = V(t) - M^2(t) \quad = \quad (k^+c + k^-)t \tag{6.12}$$

Therefore, the diffusion rate of its length fluctuation (in unit of monomer^2/sec) is

$$D(c) = \sigma^2(t)/(2t) = (k^+c + k^-)/2. \tag{6.13}$$

So the mean and variance of the filament polymerizing in the constant monomer pool linearly increases with time. However, the single-state filament model shows the linear dependence of mean and variance on monomer pool is uniform for all monomer concentrations. Therefore, this model cannot explain the biphasic behavior of both mean and variance changes observed in experiments.

6.3 The two-state filament model

6.3.1 The multi-step side walk model

The above single-state filament model predicts linear dependence of both growth rate and diffusion rate on the monomer pool, which cannot explain the biphasic behavior observed in experiments. We note that the biphasic feature takes place around the critical concentration. The monomer pool consists mainly of G-ATP, whereas the aged filament is composed of G-ADP. Above the critical concentration, the filament is capped by G-ATP most of the time. Below it, the filament occasionally exposes its G-ADP. One may thus conjecture that the two distinct capping states of the filament tip is the source of the biphasic behavior. Here we introduce a two-state model of filament. The actin either in monomeric or filamentous form assumes one of the two states depending on the bound nucleotides: G-ATP and G-ADP. We further assume no inter-conversion between these two states, which is left to the full three-state model in next section.

So we investigate a special case where the long ADP-filament is polymerizing in a constant G-ATP pool. We are interested in the case that the level of G-ATP is below its critical concentration at the end. If G-ATP is above the critical concentration, one would expect a continual length growth and ATP-cap expansion. The ADP-core thus never changes, and the dynamics reduces to the one-state case as discussed in the previous section.

In the following we consider a more general two-state polymer growth model. Suppose a polymer composed of untagged subunits is blocked at one end and immersed in a fixed pool of tagged proteins and untagged proteins. Both proteins bind reversibly to the polymer. However, the capping of a polymer by tagged protein will terminate the (de)polymerization of untagged proteins at the polymer end. We consider the dynamics of the polymer at one end while the other end is blocked. Thus, the polymer is always composed of two non-overlapping regions: the portion of tagged proteins, and the core portion of untagged proteins. The polymer length is then the sum of two portions. The polymer state is uniquely characterized by (m, n), where m and n are the lengths of tagged and untagged portion, respectively. Let $p(m, n, t)$ denote the

probability of the polymer being at the configuration (m, n) at time t. The rate of change of $p(m, n, t)$ depends on the states of m and n as displayed in Figure 6.1. The length of tagged proteins, m, lies in the non-negative integer space, and can increase or decrease by one after firing of each reaction during which n is unchanged. However, the untagged portion can jump back and forth by one unit only when the polymer is free of any tagged capping, i.e., $m = 0$. To describe the reactions easily, we called the jump along the vertical axis ($m = 0$) as the main walk, whereas the horizontal jump is the side walk.

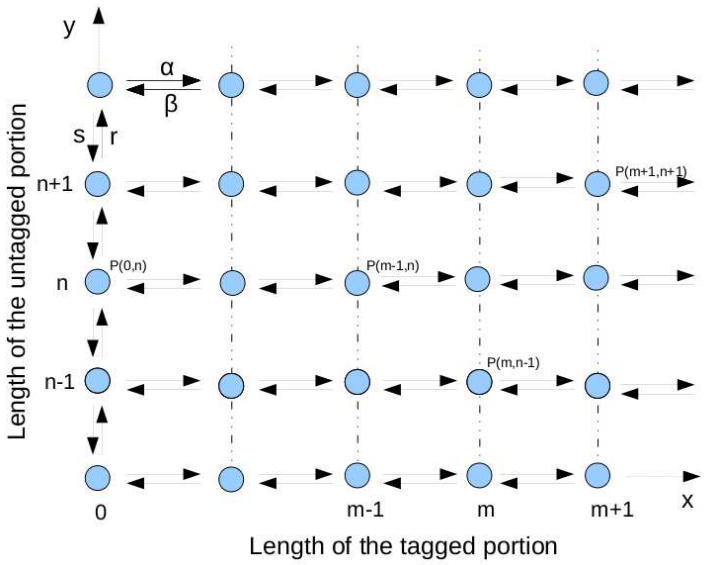

Figure 6.1: The schematic of polymerization of a filament with a core of untagged proteins occasionally interrupted by the capping of tagged proteins. Each point of the grid (m, n) represents a filament state, where m, n are the lengths of tagged and untagged portion, respectively. $P(m, n)$ denoted the probability of a filament being in that state. (α, β, r, s) are kinetic rate constants for the indicated reactions.

Suppose the on- and off-rate of tagged and untagged proteins binding are (α, β) and (r, s), respectively. In addition, $\alpha < \beta$. The master equation is as follows

when $m \geq 1, n \geq 1$: (side walk)

$$\frac{dp(m,n,t)}{dt} = \alpha\, p(m-1,n,t) + \beta\, p(m+1,n,t) - (\alpha+\beta)\, p(m,n,t) \quad (6.14)$$

when $m = 0, n \geq 1$: (main walk)

$$\begin{aligned} \frac{dp(0,n,t)}{dt} &= -\alpha\, p(0,n,t) + \beta\, p(1,n,t) - (r+s)p(0,n,t) \\ &\quad +r\, p(0,n-1,t) + s\, p(0,n+1,t) \end{aligned} \tag{6.15}$$

In the following, we want to derive the long-term behavior of the first and second moments of the polymer length distribution.

Define the probability of the filament having a cap of length m and the mean core length for fixed cap m as

$$P_m(t) = \sum_{n=0}^{\infty} p(m,n,t) \tag{6.16}$$

$$L_m(t) = \sum_{n=0}^{\infty} n\, p(m,n,t) \tag{6.17}$$

where $m \in \mathbf{N}^+ = \{0, 1, 2, \ldots\}$. It is easy to show that

$$\begin{cases} \dfrac{dP_m(t)}{dt} = \alpha\, P_{m-1}(t) + \beta\, P_{m+1}(t) - (\alpha+\beta)\, P_m(t)\ (m \geq 1) \\ \dfrac{dP_0(t)}{dt} = -\alpha\, P_0(t) + \beta\, P_1(t) \end{cases} \tag{6.18}$$

$$\begin{cases} \dfrac{dL_m(t)}{dt} = \alpha\, L_{m-1}(t) + \beta\, L_{m+1}(t) - (\alpha+\beta)\, L_m(t)\ (m \geq 1) \\ \dfrac{dL_0(t)}{dt} = -\alpha\, L_0(t) + \beta\, L_1(t) + (r-s)\, P_0(t) \end{cases} \tag{6.19}$$

Assuming that the polymer is initially composed of N_0 untagged subunits, the initial condition is

$$P_0(0) = 1, \qquad P_m(0) = 1 \quad \text{for } m \geq 0 \tag{6.20}$$

$$L_0(0) = N_0, \qquad L_m(0) = 0 \quad \text{for } m \geq 1 \tag{6.21}$$

We further assume a sufficiently large filament length (i.e. $N_0 \gg 1$) so that the filament length will not shrink to zero during the time interval we are interested in. We notice two interesting features concerning the dynamics: i) the dynamics of P_m is independent of the main walk; ii)

the evolution of L_m is only coupled to P_0. We further introduce the following quantities

$$M_x(t) = \sum_{m=0}^{\infty}\sum_{n=0}^{\infty} m\ p(m,n,t), \qquad M_y(t) = \sum_{m=0}^{\infty}\sum_{n=0}^{\infty} n\ p(m,n,t) \tag{6.22}$$

$$V_x(t) = \sum_{m=0}^{\infty}\sum_{n=0}^{\infty} m^2\ p(m,n,t), \qquad V_y(t) = \sum_{m=0}^{\infty}\sum_{n=0}^{\infty} n^2\ p(m,n,t) \tag{6.23}$$

$$V_{xy}(t) = \sum_{m=0}^{\infty}\sum_{n=0}^{\infty} 2mn\ p(m,n,t) \tag{6.24}$$

and

$$M_{x+y}(t) = M_x(t) + M_y(t) \tag{6.25}$$

$$V_{x+y}(t) = V_x(t) + V_y(t) + V_{xy}(t) \tag{6.26}$$

According to the definitions and (6.14), one has

$$\frac{dM_y(t)}{dt} = (r-s)\ P_0(t) \tag{6.27}$$

$$\frac{dV_y(t)}{dt} = 2(r-s)L_0(t) + (r+s)P_0(t) \tag{6.28}$$

The mean length of the untagged core can be solved from (6.27)

$$M_y(t) = N_0 + (r-s)\int_0^t P_0(\tau)d\tau \tag{6.29}$$

and the variance of the core length evolves as

$$\begin{aligned}\frac{d\sigma_y^2}{dt} &= \frac{d}{dt}(V_y - M_y^2) \\ &= (r+s)P_0(t) - 2(r-s)\Big[M_y(t)P_0(t) - L_0(t)\Big]\end{aligned} \tag{6.30}$$

When $\alpha < \beta$, P_m is solved as [58]

$$\begin{aligned}P_m(t) &= \rho^{m/2}e^{-(\alpha+\beta)t}\Big[I_m(vt) + \rho^{-1/2}I_{m+1}(vt) \\ &\quad +(1-\rho)\sum_{j=2}^{\infty}\rho^{-j/2}I_{m+j}(vt)\Big]\end{aligned} \tag{6.31}$$

where $\rho = \alpha/\beta, v = 2\sqrt{\alpha\beta}$, and $I_m(z)$ is a modified Bessel function of the first kind, defined as

$$I_m(z) = \Big(\frac{z}{2}\Big)^m \sum_{k=0}^{\infty} \frac{(z^2/4)^k}{k!(m+k)!}. \tag{6.32}$$

In particular,

$$P_0(t) \;\; = \;\; e^{-(\alpha+\beta)t}\Big[I_0 + \rho^{-1/2} I_1 + (1-\rho)\sum_{j=2}^{\infty} \rho^{-j/2} I_j\Big] \tag{6.33}$$

At the steady state

$$P_m(\infty) = \rho^m (1-\rho). \tag{6.34}$$

Moreover, the deviation of the transient probability $P_m(t)$ from the equilibrium value is bounded by [59]

$$|P_m(t) - P_m(\infty)| \le C e^{-t(\alpha+\beta-2\sqrt{\alpha\beta})} \tag{6.35}$$

which gives an estimate of the relaxation time of $P_m(t)$ as

$$T_{1/2} = 1/\left(\alpha + \beta - 2\sqrt{\alpha\beta}\right) \tag{6.36}$$

Define the dynamic deviation of probability $P_m(t)$ from the steady state as

$$Q_m(t) \equiv P_m(t) - P_m(\infty). \tag{6.37}$$

From (6.18) we have

$$\begin{cases} \dfrac{dQ_m(t)}{dt} = \alpha\, Q_{m-1}(t) + \beta\, Q_{m+1}(t) - (\alpha+\beta)\, Q_m(t), \quad (m \ge 1) \\ \dfrac{dQ_0(t)}{dt} = -\alpha\, Q_0(t) + \beta\, Q_1(t) \end{cases} \tag{6.38}$$

with the following initial conditions

$$Q_0(0) = \rho, \quad Q_0(\infty) = 0,$$

$$Q_m(0) = -\rho^m(1-\rho), \quad Q_m(\infty) = 0 \quad (m \ge 1).$$

We are interested in the quantities of $A_m = \int_0^\infty Q_m(\tau)d\tau$. By integrating (6.38) from 0 to ∞, we obtain

$$A_0 = \int_0^\infty [P_0(\tau) - (1-\rho)]\, d\tau = \frac{1}{\beta}\frac{\rho}{1-\rho} \tag{6.39}$$

$$A_1 = \int_0^\infty [P_1(\tau) - \rho(1-\rho)]\, d\tau = \frac{\rho}{\beta}\frac{2\rho-1}{1-\rho} \tag{6.40}$$

$$\begin{aligned} A_m &= \int_0^\infty [P_m(\tau) - \rho^m(1-\rho)]\, d\tau \\ &= \frac{1}{\beta}\frac{1}{1-\rho}\Big[(m+1)\rho^{m+1} - m\rho^m\Big] - \frac{\rho}{\beta} + \alpha \end{aligned} \tag{6.41}$$

To solve $L_m(t)$ from (6.19), we apply the method of generating functions [58]. First, nondimensionalize L_m by changing variables

$$K_m(t) = L_m(t)/N_0 \tag{6.42}$$

Then K_m's solve

$$\begin{cases} \dfrac{dK_m(t)}{dt} = \alpha\ K_{m-1}(t) + \beta\ K_{m+1}(t) - (\alpha+\beta)\ K_m(t)\ (m \geq 1) \\ \dfrac{dK_0(t)}{dt} = -\alpha\ K_0(t) + \beta\ K_1(t) + (r-s)\ P_0(t)/N_0 \end{cases} \tag{6.43}$$

with the initial condition

$$K_0(0) = 1, \quad K_m(0) = 0 \text{ for } m \geq 1.$$

After introducing dummy initial conditions as

$$K_{-m}(0) = d_m \text{ for } m \geq 1, \tag{6.44}$$

we get the generating function of K_m as

$$G(t,z) = \sum_{n=-\infty}^{\infty} K_n(t)\ z^n \tag{6.45}$$

and it satisfies

$$\frac{\partial G(t,z)}{\partial t} = (z-1)(\alpha - \beta/z)\ G(t,z) \tag{6.46}$$

with initial condition

$$G(0,z) = 1 + \sum_{n=1}^{\infty} d_n \; z^{-n}. \tag{6.47}$$

The general solution to (6.46) is

$$G(t,z) = \phi(z) e^{-(\alpha+\beta)t} \sum_{n=-\infty}^{\infty} \rho^{n/2} I_n(vt) \; z^n \tag{6.48}$$

The initial condition thus implies

$$\phi(z) = 1 + \sum_{n=1}^{\infty} d_n \; z^{-n} \tag{6.49}$$

To solve these K_m's, the coefficient of the m-th power of z as in (6.45), we need to solve the d_n's. We notice the boundary condition in (6.43), and thus have

$$\alpha \; K_{-1}(t) - \beta \; K_0(t) = (r-s) P_0(t)/N_0 \tag{6.50}$$

By observing $K_{-1}(t)$ and $K_0(t)$ as the coefficients of the terms containing z^{-1} and z^0 in (6.48), we have

$$K_0(t) = \left[I_0(vt) + \sum_{n=1}^{\infty} d_n I_n(vt) \rho^{\frac{n}{2}} \right] e^{-(\alpha+\beta)t} \tag{6.51}$$

$$K_{-1}(t) = \left[\rho^{-\frac{1}{2}} I_1(vt) + \sum_{n=1}^{\infty} d_n I_{n-1}(vt) \rho^{\frac{n-1}{2}} \right] e^{-(\alpha+\beta)t} \tag{6.52}$$

Plug K_{-1}, K_0 and P_0 into (6.50), one has

$$\begin{aligned} & \beta \left[(\rho d_0 - 1) \, I_0 + \rho^{\frac{1}{2}} \, (\rho d_2 + 1 - d_1) \, I_1 + \sum_{n=2}^{\infty} \rho^{-\frac{n}{2}} \, (\rho d_{n+1} - d_n) \, I_n \right] e^{-(\alpha+\beta)t} \\ = & \\ & \frac{r-s}{N_0} \left[I_0 + \rho^{-\frac{1}{2}} I_1 + (1-\rho) \sum_{n=2}^{\infty} \rho^{-\frac{n}{2}} I_n \right] e^{-(\alpha+\beta)t} \end{aligned} \tag{6.53}$$

Since the above equation holds for all t, all the coefficients of I_n's should agree on both sides. Accordingly, one gets

$$d_1 = \rho^{-1} \left[1 + \frac{1}{\beta} \frac{r-s}{N_0} \right] \tag{6.54}$$

$$d_j = \rho^{-j} \left[1 - \rho + \frac{2}{\beta} \frac{r-s}{N_0} + (j-2) \frac{1-\rho}{\beta} \frac{r-s}{N_0} \right], \text{for } j \geq 2 \tag{6.55}$$

Therefore, one solves all the L_n's as

$$\begin{aligned} L_n(t) &= N_0 P_n(t) + \frac{r-s}{\beta}\,\rho^{n/2} e^{-(\alpha+\beta)t}\Big[\rho^{-1/2} I_{n+1} + 2\rho \sum_{j=2}^{\infty} \rho^{-j/2} I_{n+j} \\ &\quad + (1-\rho)\rho^{n/2} \sum_{j=n+2}^{\infty} \rho^{-j/2} j I_j - n(1-\rho)\rho^{n/2} \sum_{j=n+2}^{\infty} \rho^{-j/2} I_j\Big] \end{aligned} \tag{6.56}$$

In particular, one has

$$L_0(t) = N_0 P_0 + \frac{r-s}{\beta} e^{-(\alpha+\beta)t} \left[\rho^{-1/2} I_1 + 2\rho \sum_{j=2}^{\infty} \rho^{-j/2} I_j + (1-\rho) \sum_{j=2}^{\infty} j \rho^{-j/2} I_j\right] \tag{6.57}$$

Applying the following relationship between Bessel functions

$$I_{j+1}(x) = I_{j-1}(x) - \frac{2j}{x} I_j(x) \tag{6.58}$$

one has

$$j I_j(vt) = \frac{vt}{2}\,\Big(I_{j-1}(vt) - I_{j+1}(vt)\Big) \tag{6.59}$$

Hence, $L_0(t)$ can be simplified as

$$\begin{aligned} L_0(t) &= \frac{r-s}{\beta}\,\Big(\rho^{-1/2} I_1 + \beta\rho^{-1/2}(1-\rho) I_1 t + \beta(1-\rho) I_2 t\Big)\; e^{-(\alpha+\beta)t} \\ &\quad + \frac{r-s}{\beta}\,\Big(2\rho + \beta(1-\rho)^2 t\Big)\left(\sum_{j=2}^{\infty} \rho^{-j/2} I_j\right)\; e^{-(\alpha+\beta)t} + N_0 P_0 \end{aligned} \tag{6.60}$$

We also obtain from (6.33)

$$\sum_{j=2}^{\infty} \rho^{-j/2} I_j = \frac{1}{1-\rho}\Big[P_0(t) e^{(\alpha+\beta)t} - (I_0 + \rho^{1/2} I_1)\Big] \tag{6.61}$$

Therefore

$$L_0(t) = N_0\; P_0(t) + \frac{r-s}{\beta}\frac{2\rho}{1-\rho} P_0(t) + (r-s)(1-\rho) P_0(t) t + \mathcal{R}(t) \tag{6.62}$$

where the remainder term is

$$\mathcal{R}(t) = \frac{r-s}{\beta}\; e^{-(\alpha+\beta)t}\left(-\frac{2\rho + \beta(1-\rho)^2 t}{1-\rho} I_0 + \frac{\rho^{-1/2} - 3\rho^{1/2}}{1-\rho} I_1 + \beta(1-\rho) t I_2\right) \tag{6.63}$$

For any fixed n and $\alpha < \beta$,

$$I_n(z) \to \frac{e^z}{\sqrt{2\pi z}}, \text{ as } z \to \infty \tag{6.64}$$

Therefore,

$$\mathcal{R}(t) \to 0, \text{ as } t \to \infty. \tag{6.65}$$

Accordingly,

$$\begin{aligned} L_0 - M_y P_0 &= L_0 - \left(N_0 + (r-s) \int_0^t P_0(\tau) d\tau \right) P_0(t) \\ &= \frac{r-s}{\beta} \frac{2\rho}{1-\rho} P_0(t) - (r-s) P_0(t) \int_0^t P_0(\tau)(1-\rho) d\tau + \mathcal{R}(t) \end{aligned} \tag{6.66}$$

So as t goes infinitely large

$$\begin{aligned} L_0 - M_y P_0 &= \frac{r-s}{\beta} \frac{2\rho}{1-\rho} P_0(\infty) - (r-s) P_0(\infty) \int_0^\infty P_0(\tau)(1-\rho) d\tau \\ &= \frac{r-s}{\beta} \frac{\alpha}{\beta} \end{aligned} \tag{6.67}$$

According to (6.39), $M_y(t)$ in (6.29) asymptotically approaches

$$M_y(t) \to N_0 + (r-s)(1-\alpha/\beta)t + \frac{r-s}{\beta} \frac{\alpha/\beta}{1-\alpha/\beta}. \tag{6.68}$$

and from (6.67) the rate of change of the variance in (6.30) becomes

$$\frac{d\sigma_y^2}{dt} \to (r+s)(1-\alpha/\beta) + 2\frac{(r-s)^2}{\beta} \frac{\alpha}{\beta} \tag{6.69}$$

We are now considering the total length of a filament, then

$$\frac{dM_{x+y}(t)}{dt} = (\alpha - \beta) + (\beta + r - s)\ P_0(t) \tag{6.70}$$

$$\begin{aligned} \frac{dV_{x+y}(t)}{dt} &= (\alpha + \beta) + 2rP_0(t) + 2(\alpha - \beta) M_{x+y}(t) \\ &\quad + (\beta + r - s)\Big(2L_0(t) - P_0(t) \Big) \end{aligned} \tag{6.71}$$

The integration of (6.70) yields a total mean length

$$M_{x+y}(t) = N_0 + (\alpha - \beta)\ t + (\beta + r - s) \int_0^t P_0(\tau) d\tau \tag{6.72}$$

$$\to N_0 + (r-s)(1-\alpha/\beta)t + \frac{\beta + r - s}{\beta} \frac{\alpha/\beta}{1-\alpha/\beta} \tag{6.73}$$

so

$$j(t) = \frac{dM_{x+y}(t)}{dt} = (r-s)(1-\alpha/\beta) \tag{6.74}$$

Therefore, the comparison of (6.68) and (6.73) gives M_x at large times

$$M_x = M_{x+y} - M_y \to \frac{\alpha/\beta}{1-\alpha/\beta} \tag{6.75}$$

which is consistent with the mean size of the tagged cap

$$M_x = \sum_{m=0}^{\infty} mP_m(t) \to \frac{\alpha/\beta}{1-\alpha/\beta}. \tag{6.76}$$

The evolution of the variance follows as

$$\begin{aligned} \frac{d\sigma_{x+y}^2}{dt} &= \frac{d}{dt}(V_{x+y} - M_{x+y}^2) \\ &= (\alpha+\beta) + (r+s-\beta)P_0(t) + 2(\beta+r-s)\Big[L_0(t) - M_{x+y}(t)P_0(t)\Big] \\ &\to (r+s)(1-\alpha/\beta) + 2\frac{(r-s)^2}{\beta}\frac{\alpha}{\beta} \end{aligned} \tag{6.77}$$

so

$$j(t) = \frac{d\sigma_{x+y}^2}{dt} = (r+s)(1-\alpha/\beta) + 2\frac{(r-s)^2}{\beta}\frac{\alpha}{\beta} \tag{6.78}$$

At large times,

$$\frac{d\sigma_{x+y}^2}{dt} = \frac{d\sigma_y^2}{dt} \tag{6.79}$$

which implies that the length fluctuation is largely due to the dynamic change of the untagged core. This conclusion is reasonable, because the cap lengths eventually relax to an exponentially decreasing distribution at large times. Thus, the time-dependent expansion of the variance of total length results mainly from the core length fluctuation.

Now we obtain the mean elongation rate of the polymer at large times as

$$j(t) \to (r-s)(1-\alpha/\beta), \tag{6.80}$$

and the diffusion rate for the length fluctuation

$$D(t) \to \frac{r+s}{2}\left(1-\frac{\alpha}{\beta}\right) + \frac{(r-s)^2}{\beta}\left(\frac{\alpha}{\beta}\right). \tag{6.81}$$

The time required for the establishment of stable elongation and diffusion rates is the relaxation time ($T_{1/2}$) for $P_0(t)$ as indicated in (6.27) and (6.30). The relaxation time $T_{1/2}$ is determined only by the side walk, and is a function of α and β only as in (6.36).

The above analysis shows how tagged protein interferes with the length evolution of a filament of untagged protein when the tagged protein is below its critical concentration (i.e. $\alpha < \beta$). The tagged proteins at this concentration form a cap of finite length at the tip, and thus the direct contribution of cap lengths to the filament length changes is negligible at large times. It is the persistent addition or removal of untagged proteins that cause the change and fluctuation of total lengths. Therefore, the long-term elongation and fluctuation of the total lengths is equivalent to those of the untagged core.

However, the occasional cap formation indirectly contributes to the total length changes by interrupting the untagged core length dynamics. In the absence of tagged proteins, the filament composed of untagged protein alone is undergoing a biased random walk in the discrete length space. The elongation and diffusion rates are $r - s$ and $(r + s)/2$, respectively. In the presence of tagged proteins, the untagged core is free to grow or shrink only when the tip is not capped by the tagged proteins, which has a probability of $1 - \alpha/\beta$. In fact, the persistent firing of reactions involving untagged proteins consists of cycles of two processes: one is the process of the accumulation of tagged protein at the filament tip until it completely releases from the tip, and the other is the addition or removal of the untagged proteins, which is eventually terminated by capping of tagged proteins. If we view all the reactions in a unit time, we found that the two processes take place stochastically with a total time of $(1 - \alpha/\beta)$ allocated for the second processes. Thus, the effective elongation rate of the core is expected to be the product of uncapped elongation rate ($r - s$) and the mean time ($1 - \alpha/\beta$) being at the uncapped state as in (6.80). The effective diffusion, however, has two terms as indicated in (6.81): the first term represents the core length fluctuation induced by the stochastic dynamics of untagged protein during a mean time of $1 - \alpha/\beta$ when the tip is uncapped, and the second term represents the length fluctuation generated by the stochastic freezing during a mean time of α/β when the tip is capped by tagged proteins. Interestingly, the second term is a function of the net elongation

rate of uncapped core, which is $r - s$. Therefore, for $r = s$,

$$j(t) = 0, \quad D(t) = \left(1 - \frac{\alpha}{\beta}\right) s \tag{6.82}$$

The other interesting feature is that the diffusion constant is a decreasing function of β, provided that the ratio of α/β is fixed. This implies that the slow releasing of tagged protein may result in a greatly elevated length fluctuation.

As for the case where the tagged protein is above its critical concentration, i.e. $\alpha > \beta$, one expects the mean length of the tagged cap will linearly expand in time, and the probability of having the untagged portion exposed at the end is vanishing at large time. Therefore, the elongation and fluctuation result mainly from the dynamics of tagged proteins, with untagged portion nearly unchanged. The dynamics is then reduced to the single-state filament model as in the previous section, and the single state is the tagged protein. Thus, for $\alpha > \beta$, one has

$$j = \alpha - \beta \tag{6.83}$$

$$D = (\alpha + \beta)/2 \tag{6.84}$$

We note that the two-state filament model introduced earlier is a special case of the multi-step side walk model, with the corresponding parameters as

$$\alpha = k_T^+ \, c_T, \; \beta = k_T^-, \; s = k_D^-, \; r = 0,$$

where $k_T^{\pm}$ are the on- and off-rate of G-ATP, k_D^- is the depolymerization rate of ADP-actin, and c_T is the G-ATP concentration. We expect the long-time dynamics of the filament to have the statistical properties as in (6.80), (6.81), (6.83) and (6.84). The same dependence of diffusion rate on the G-ATP concentration is also predicted by Vavylonis *et al.* [26]. But we derived the result directly from the master equation of the filament state. In addition, our multi-step side walk model allows both addition and deletion of the untagged core proteins, and thus is more general than the case with only deletion of untagged proteins. Stochastic simulations confirm the biphasic behavior of the filament length dynamics at large time as shown in Figure 6.2 and 6.3.

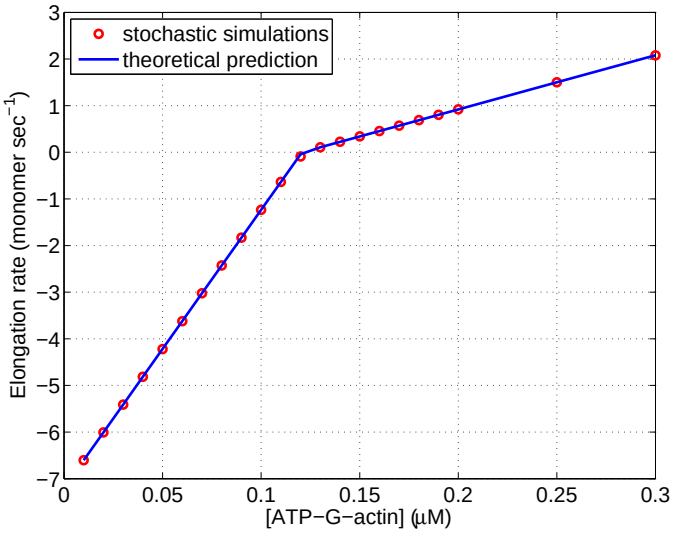

Figure 6.2: The elongation rate of filament barbed end. The kinetic constants used in the simulations are: $k_T^+ = 11.6\ \mu$M s^{-1}, $k_T^- = 1.4$ s^{-1}, $k_D^- = 7.2$ s^{-1}. The blue line represents results of stochastic simulations, whereas the red is predicted according to (6.80) and (6.83).

6.3.2 One-step side walk model

In the previous section, we described the nucleotide-associated filament in two-state model with an unbounded side walk, i.e., $m \in \{0, 1, 2, \dots, \}$. Now we use the modified two-state model to examine the dynamics of statistics of filament lengths in the presence of capping proteins. Suppose a generic capping protein binds at a polymer end with rates of (α, β), and the polymer in uncapped states adds or removes monomers at rates of (r, s). The dynamics of such polymer can be described as a model with one-step side walk ($m \in \{0, 1\}$) as in Figure 6.4.

Similarly, we aim to explore the long-time statistical properties, such as mean elongation rate and diffusion rate constant. Let $p_n(t)$ and $q_n(t)$ be the probabilities of the polymer of length n being at the uncapped and capped states, respectively. One has the master equation as

$$\begin{cases} \dfrac{dp_n}{dt} = -\alpha\ p_n + \beta\ q_n + r\ p_{n-1} + s\ p_{n+1} - (r+s)\ p_n \\ \dfrac{dq_n}{dt} = \alpha\ p_n - \beta\ q_n \end{cases} \tag{6.85}$$

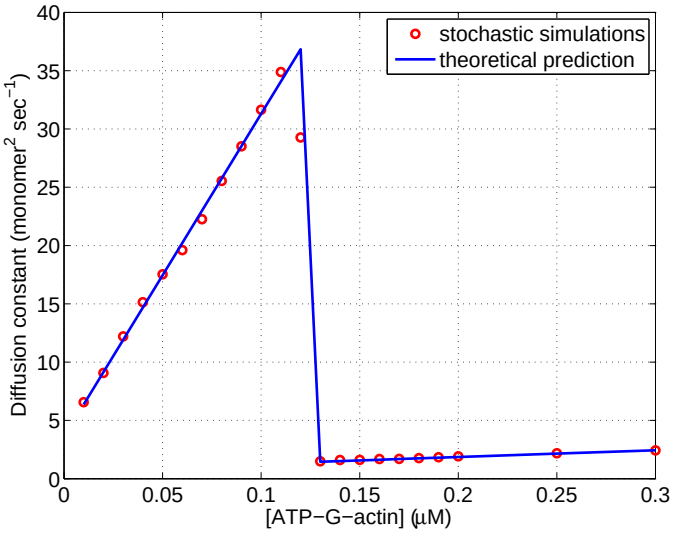

Figure 6.3: The length fluctuations of filament barbed end. The kinetic constants used in the simulations are: $k_T^+ = 11.6\ \mu\text{M s}^{-1}$, $k_T^- = 1.4\ \text{s}^{-1}$, $k_D^- = 7.2\ \text{s}^{-1}$. The blue line represents results of stochastic simulations, whereas the red is predicted according to (6.80) and (6.83).

Define the following quantities

$$P(t) = \sum_n p_n(t), \qquad Q(t) = \sum_n q_n(t) \tag{6.86}$$

$$M_p(t) = \sum_n n\ p_n(t), \qquad M_q(t) = \sum_n n\ q_n(t) \tag{6.87}$$

$$M(t) = \sum_n n\,(p_n(t) + q_n(t))\,, \quad V(t) = \sum_n n^2\,(p_n(t) + \ q_n(t)) \tag{6.88}$$

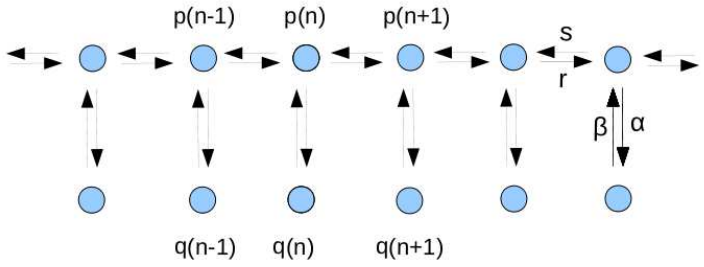

Figure 6.4: The schematic of a generic two-state polymer model with one-step side walk. In the context of polymer growth with capping factors, $p(n)$ and $q(n)$ represent the probability of the n-subunit polymer being at the uncapped and capped state, whereas (α, β, r, s) are relevant reaction rates.

and from (6.85) we know

$$\begin{cases} \dfrac{dP(t)}{dt} = -\alpha\ P(t) + \beta\ Q(t) \\ \dfrac{dQ(t)}{dt} = \quad \alpha\ P(t) - \beta\ Q(t) \end{cases} \tag{6.89}$$

$$\begin{cases} \dfrac{dM_p(t)}{dt} = -\alpha\ M_p + \beta\ M_q + (r-s)\ P(t) \\ \dfrac{dM_q(t)}{dt} = \quad \alpha\ M_p - \beta\ M_q \end{cases} \tag{6.90}$$

$$\begin{cases} \dfrac{dM(t)}{dt} = (r-s)\ P(t) \\ \dfrac{dV(t)}{dt} = 2(r-s)\ M_p(t) + (r+s)P(t) \end{cases} \tag{6.91}$$

If the polymer of length N_0 is assumed uncapped initially, then $P(0) = 1, Q(0) = 0$. We get

the solution as

$$
\begin{aligned}
P(t) &= \frac{\beta}{\alpha+\beta} + \frac{\alpha}{\alpha+\beta}\, e^{-(\alpha+\beta)t} && (6.92)\\
M_p(t) &= \frac{\alpha\, N_0}{\alpha+\beta}\left(\frac{\beta}{\alpha} + e^{-(\alpha+\beta)t}\right) && (6.93)\\
&\quad + \frac{\beta(r-s)}{\alpha+\beta}\left[\frac{\beta}{\alpha+\beta}\, t + \frac{\alpha}{(\alpha+\beta)^2}\left(1 - e^{-(\alpha+\beta)t}\right)\right] && (6.94)\\
&\quad + \frac{\alpha(r-s)}{\alpha+\beta}\left[\frac{\alpha}{\alpha+\beta}\, t\, e^{-(\alpha+\beta)t} + \frac{\beta}{(\alpha+\beta)^2}\left(1 - e^{-(\alpha+\beta)t}\right)\right] && (6.95)\\
M(t) &= N_0 + \frac{\beta(r-s)}{\alpha+\beta}\, t + \frac{\alpha(r-s)}{(\alpha+\beta)^2}\left(1 - e^{-(\alpha+\beta)t}\right) && (6.96)
\end{aligned}
$$

Accordingly, the variance evolves with a rate

$$
\begin{aligned}
\frac{d\sigma^2(t)}{dt} &= (r+s)P(t) - 2(r-s)\left(M(t)P(t) - M_p(t)\right)\\
&\to \frac{(r+s)}{(1+\alpha/\beta)} + \frac{2\alpha\beta(r-s)^2}{(\alpha+\beta)^3}, \qquad \text{as } t \to \infty && (6.97)
\end{aligned}
$$

The asymptotic value of diffusion constant is

$$
D = \frac{(r+s)}{2(1+\alpha/\beta)} + \frac{(r-s)^2}{\beta}\frac{\alpha/\beta}{(1+\alpha/\beta)^3} \qquad (6.98)
$$

and the time for the establishment of the stable diffusion depends on how fast the capping and uncapping is equilibrated ($T_{1/2} \sim 1/(\alpha+\beta)$). At large times, the elongation rate in (6.91) is

$$
j = (r-s)/(1+\alpha/\beta). \qquad (6.99)
$$

Let us consider the special case where $r = s$. In the absence of capping proteins the diffusion constant is $D = r$. However, with the introduction of capping proteins, the diffusion constant reduces to $D = r/(1+\alpha/\beta)$. But the net growth rate is always vanishing, which is independent of the capping proteins.

The multi-step model is occasionally reduced to a one-step model by lumping a sequence of first-order reactions into a single effective first-order reaction in the first order approximation [60]. We will examine the accuracy of such simplification in the context of filament growth. By the simplification, the multi-step binding of G-ATP back and forth is reduced into two effective

steps: the first step is the jump from $m = 0$ to $m = 1$, and the other is the effective jump back from $m = 1$ to $m = 0$. The mean rate of the forward jump is related to the G-ATP binding and $\alpha = k_T^+ c$. The mean return time from $m = 1$ to $m = 0$ is estimated to be $-1/J$, where J is the net elongation rate $k_T^- - k_T^+ c$ [60]. Thus a first approximation for the jumping rate we try is $\beta = k_T^- - k_T^+ c$. Now we obtain the approximated one-step side walk model with parameters

$$\alpha = k_T^+ c, \quad \beta = k_T^- - k_T^+ c, \quad s = k_D^-, \quad r = 0,$$

Thus, from (6.98) we have

$$\begin{aligned} D(c) &= -\frac{1}{k_T^-}\Big(\frac{k_D^-}{k_T^-}\Big)^2 \left[k_T^+ c - \frac{k_T^-}{2}\Big(1 - \frac{k_T^-}{2k_D^-}\Big)\right]^2 + \frac{k_D^-}{2} \\ &\quad + \frac{k_T^-}{4}\Big(\frac{k_D^-}{k_T^-}\Big)^2\Big(1 - \frac{k_T^-}{2k_D^-}\Big)^2 \end{aligned} \tag{6.100}$$

The diffusion rate achieves a maximum at $c_0 = \frac{1}{2}\frac{k_T^-}{k_T^+}\Big(1 - \frac{k_T^-}{2k_D^-}\Big)$ and

$$D(c_0) = \frac{k_D^-}{2} + \frac{k_T^-}{4}\Big(\frac{k_D^-}{k_T^-}\Big)^2\Big(1 - \frac{k_T^-}{2k_D^-}\Big)^2. \tag{6.101}$$

At the boundaries, one has

$$D(0) = \frac{k_D^-}{2}, \quad D\Big(\frac{k_T^-}{k_T^+}\Big) = 0 \tag{6.102}$$

$$\left.\frac{dD(c)}{dc}\right|_{c=0} = \frac{k_D^-}{k_T^-}\left(\frac{k_D^-}{k_T^-} - \frac{1}{2}\right)k_T^+ \tag{6.103}$$

$$\left.\frac{dD(c)}{dc}\right|_{k_T^- c = k_T^-} = -2\Big(\frac{k_D^-}{k_T^-}\Big)^2 + \frac{k_D^-}{k_T^-}\left(\frac{k_D^-}{k_T^-} - \frac{1}{2}\right)k_T^+ \tag{6.104}$$

Qualitatively, the one-step model shares some features with the previous multi-step model. First, below the critical concentration, the diffusion of length fluctuations increases as the monomer concentration increases and then drops. Second, the maximal diffusion rate increases as k_D^- increases, but decreases with increased k_T^-. Examples of the dependence of diffusion rate on the kinetics are displayed in Figure 6.5. However, comparison of Figure 6.3 and 6.5 reveals an obvious difference between these two models. The one-step model predicts a bell-shaped

diffusion-concentration curve, whereas the multi-step model obtains a linear curve when the concentration is below the critical concentration. The diffusion starts to drop gradually before half of the critical concentration in the one-step model, whereas it is steep at the critical concentration in the multi-step model. Moreover, the maximal diffusion constant for the one-step model is one third of that predicted by multi-step model.

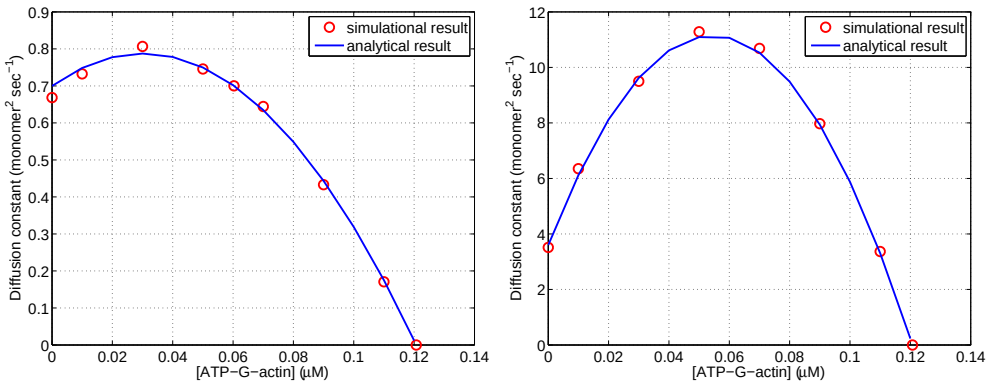

Figure 6.5: The concentration-diffusion curves. These curves are predicted according to (6.101), with rate constants $k_T^+ = 11.6\ \mu M^{-1}s^{-1}, k_T^- = 1.4\ s^{-1}, k_D^- = 1.4\ s^{-1}$ (left), $7.2\ s^{-1}$ (right).

6.4 The three-state filament model

6.4.1 The master equation for filament states

In this section we investigate the single filament polymerization in a system of fixed composition of actin monomers bounded with three nucleotides. Both filament ends are active for (Ode)polymerization. Suppose the constant concentrations for ADP-, ADP-Pi- and ATP-G-actin are c_1, c_2, c_3, respectively. Assume the on- and off-rates of the three-state actin at the barbed end are $k_b^{\pm 1}, k_b^{\pm 2}, k_b^{\pm 3}$, respectively. The corresponding kinetic rates at the pointed end are $k_p^{\pm 1}, k_p^{\pm 2}, k_p^{\pm 3}$, respectively. Within a filament, the uniform hydrolysis rate is assumed to be r_h, and the subsequent Pi release rate is r_i.

We identify a single filament by a sequence of nucleotide types, where ADP, ADP-Pi and

ATP are denoted as $1, 2, 3$, respectively. So a typical filament of length n can be viewed as $(a_1 a_2 \dots a_n)$, where a_i indicates the nucleotide type of the i-th subunits counted from the barbed end. Specifically, a_1 denotes the nucleotide associated with the barbed end. We order all the possible nucleotide states of single filament of particular length n as follows:

$$
\begin{aligned}
n = 1: \quad & [(1)\ (2)\ (3)] \\
n = 2: \quad & [(11)\ (21)\ (31)];\ [(12)\ (22)\ (32)];\ [(13)\ (23)\ (33)] \\
n = 3: \quad & [(111)\ (211)\ (311)];\ [(121)\ (221)\ (321)];\ [(131)\ (231)\ (331)] \\
& [(112)\ (212)\ (312)];\ [(122)\ (222)\ (322)];\ [(132)\ (232)\ (332)]; \\
& [(113)\ (213)\ (313)];\ [(123)\ (223)\ (323)];\ [(133)\ (233)\ (333)] \\
& \vdots
\end{aligned}
$$

We group all the nucleotide states into triads. One can generate the triads for length N from the states of length $N-1$. For each state in length $N-1$, say

$$(a_1 a_2 \dots a_{N-1}),$$

we generate a triad for length N as

$$[(1a_1 a_2 \dots a_{N-1}), (2a_1 a_2 \dots a_{N-1}), (3a_1 a_2 \dots a_{N-1})].$$

We put all the nucleotide sequences of certain length n ordered as above in the column vector P^n. For instance,

$$
\begin{aligned}
P^1 &= (p(1), p(2), p(3))^T \\
P^2 &= (p(11), p(21), p(31), p(12), p(22), p(32), p(13), p(23), p(33))^T
\end{aligned}
$$

where $p(a_1 a_2 \dots a_n, t)$ represents the probability of a filament being at a state with the particular nucleotide sequence $(a_1 a_2 \dots a_n)$ at time t (hereafter we suppress t).

In the presence of monomer pool, both filament ends are undergoing stochastic elongation and shrinkage. The time evolution of the probability P^n is

$$\frac{dP^n}{dt} = L_{n-1}P^{n-1} + U_{n+1}P^{n+1} - D_nP^n + H_nP^n \tag{6.105}$$

where the transfer terms

$$\begin{aligned}
L_{n-1} &= \mathbf{I}_{3^{n-1}} \otimes (k_b^{+1}c_1 \quad k_b^{+2}c_2 \quad k_b^{+3}c_3)^T + (k_p^{+1}c_1 \quad k_p^{+2}c_2 \quad k_p^{+3}c_3)^T \otimes \mathbf{I}_{3^{n-1}}, \\
U_{n+1} &= \left(\mathbf{I}_{3^n} \otimes (k_b^{-1} \quad k_b^{-2} \quad k_b^{-3}) + (k_p^{-1} \quad k_p^{-2} \quad k_p^{-3}) \otimes \mathbf{I}_{3^n}\right), \\
D_n &= \begin{pmatrix} k_b^{+1}+k_p^{+1} \\ k_b^{+1}+k_p^{+2} \\ k_b^{+1}+k_p^{+3} \end{pmatrix}^T \cdot \begin{pmatrix} c_1 \\ c_2 \\ c_3 \end{pmatrix} \mathbf{I}_{3^n} \\
&\quad + \mathbf{I}_{3^{n-1}} \otimes \begin{pmatrix} k_b^{-1} & & \\ & k_b^{-2} & \\ & & k_b^{-3} \end{pmatrix} + \begin{pmatrix} k_p^{-1} & & \\ & k_p^{-2} & \\ & & k_p^{-3} \end{pmatrix} \otimes \mathbf{I}_{3^{n-1}},
\end{aligned}$$

and the hydrolysis term is a collection of hydrolysis and Pi release reactions on all subunits as

$$H_n = \sum_{i=0}^{n-1} \mathbf{I_{3^i}} \otimes (\mathbf{R} \otimes \mathbf{I_{3^{n-1-i}}}),$$

where

$$R = \begin{pmatrix} 0 & r_i & 0 \\ 0 & -r_i & r_h \\ 0 & 0 & -r_h \end{pmatrix}.$$

Define the probability vector of a filament being of particular length and nucleotide composition as

$$P = (P^{1T}, P^{2T}, P^{3T}, P^{4T}, \ldots)^T.$$

According to (6.105), we get

$$\frac{dP}{dt} = K\ P, \tag{6.106}$$

where

$$K = \begin{pmatrix} H_1 - D_1 & U_2 & & & & \\ L_1 & H_2 - D_2 & U_3 & & & \\ & L_2 & H_3 - D_3 & U_4 & & \\ & & L_3 & H_4 - D_4 & U_5 & \\ & & & & \ddots & \end{pmatrix}$$

We notice that in the above expression the hydrolysis and Pi release are assumed to be the same for both terminal and interior subunit. The dynamic changes of mean and variance of the filament length are

$$j = \frac{dM}{dt} = \frac{d}{dt}\left(\sum_n nP_n\right) \tag{6.107}$$

$$D = \frac{d\sigma^2}{dt} = \frac{d}{dt}\left(\sum_n n^2 P_n - \left(\sum_n nP_n\right)^2\right) \tag{6.108}$$

where P_n is the sum of all components of P^n.

6.4.2 Result of numerical simulations

Though the dynamics of lengths and nucleotide composition of single filament can be described in a nice mathematical form as in (6.106), it is not feasible to analytically solve the filament profile due to the extremely large size of the linear ODEs. One has to turn to the stochastic simulation for numerical solutions.

Slightly different polymerization models have been proposed in the literature. Two major differences between the models lie in the dynamics of ADP-Pi-G-actin and Pi releasing rate at the filament ends. Some proposed that G-ADP-Pi is kinetically identical to G-ATP, while others argued that their dynamics are significantly different. Another debate is that whether the inorganic Pi of ADP-Pi releases significantly faster at the terminal subunit than at the interior subunits. Here we will examine the long-time elongation and fluctuations of filament polymerization using a kinetic model proposed by Fujiwara *et al.* [8]. In this model, the off rates of G-ADP-Pi at both ends are surprisingly small and the phosphate releases faster at the terminal

ADP-Pi-actin than at the interior ones. The kinetic rate constants are listed in Table 6.1 and 6.2. We also examine the effects of end capping and Pi releasing rate of the terminal subunit on the long-time behavior of elongation and length fluctuation by blocking the pointed ends and suppressing the terminal Pi release. The monomer pool is assumed to be composed of a constant concentration of G-ATP. The long-time elongation and length diffusion rate constants for each model are displayed in Figure 6.6. Interestingly, we observe that the capping of pointed end does not significantly affect the long-time behavior of filament polymerization when Pi releases fast at the tip as we compare Model I and III. However, both the elongation and diffusion curves changes significantly when Pi at the tip releases at the the slow rate as the interior subunits as displayed in Model I and II. The slow Pi release decreases the critical concentration of G-ATP, and produces a surprisingly high fluctuations at a G-ATP concentration slightly less than the critical concentration. With slow Pi release at the tip, the filament tip is presumably stabilized since the dynamics of ADP-Pi-actin is extremely slow. We also re-examine a kinetic model used by Vavylonis *et al.* [26] whereby G-ADP-Pi behaves similar to G-ATP and Pi release is slow at the barbed end. In all these models, we observed a biphasic behavior of filament polymerization around the critical concentration. A tooth-shaped diffusion curve occurs at concentrations below the critical concentration. By comparing Figure 6.2, 6.3 and 6.6, we conclude that the two-state filament model captures the biphasic feature of the full three-state model, and the large length fluctuations result from the intermittent capping of filament ends by dynamically distinct G-ADP and G-ATP.

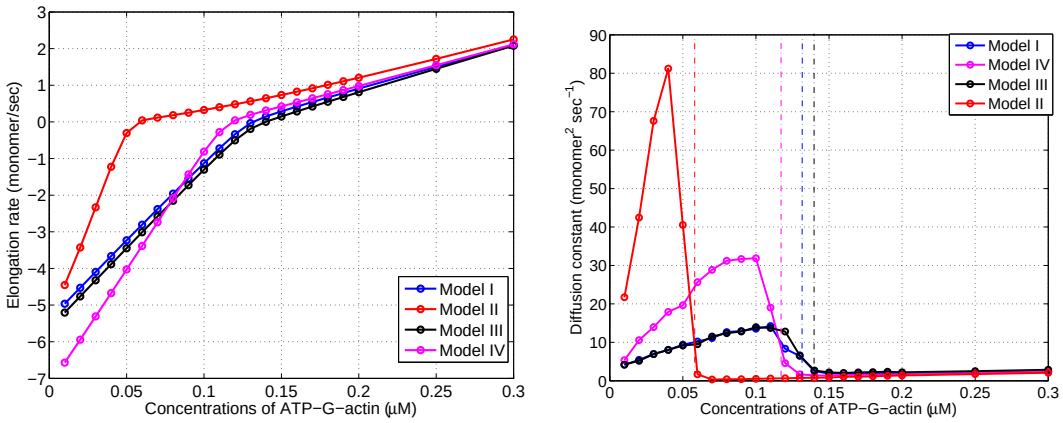

Figure 6.6: The elongation and diffusion curves of actin filament. The dash dot lines on the right figure represent the G-ATP concentrations where the net elongation rate is zero for each model. Model-I: filament with only barbed end free, fast Pi releasing at the tip; Model-II: same as in Model-I but with uniform slow Pi release; Model-III: filament with both ends free, fast Pi releasing at the tip; Model-IV: our three-state filament with only barbed end free, uniform slow Pi release. All the kinetic constants are listed on Table 6.1 and 6.2.

Table 6.1: The kinetic rate constants used in the single filament model

Symbol	Definition	Model I ([8])	Model II ([8])
k_b^{+3}	On-rate of G-ATP at the barbed end	$11.6\ \mu\text{M}^{-1}\ \text{s}^{-1}$	$11.6\ \mu\text{M}^{-1}\ \text{s}^{-1}$
k_b^{-3}	Off-rate of G-ATP at the barbed end	$1.4\ \text{s}^{-1}$	$1.4\ \text{s}^{-1}$
k_b^{-2}	Off-rate of G-ATP-Pi at the barbed end	$0.2\ \text{s}^{-1}$	$0.2\ \text{s}^{-1}$
k_b^{-1}	Off-rate of G-ADP at the barbed end	$5.4\ \text{s}^{-1}$	$5.4\ \text{s}^{-1}$
r_h	Hydrolysis rate of ATP	$0.3\ \text{s}^{-1}$	$0.3\ \text{s}^{-1}$
r_i	Pi release rate of interior subunits	$0.003\ \text{s}^{-1}$	$0.003\ \text{s}^{-1}$
r_i^*	Pi release rate of terminal subunits	$2\ \text{s}^{-1}$	$0.003\ \text{s}^{-1}$

Table 6.2: The kinetic rate constants used in the single filament model (continued)

Symbol	Definition	Model III ([8])	Model IV ([26])
k_b^{+3}	On-rate of G-ATP at the barbed end	$11.6\ \mu\text{M}^{-1}\ \text{s}^{-1}$	$11.6\ \mu\text{M}^{-1}\ \text{s}^{-1}$
k_b^{-3}	Off-rate of G-ATP at the barbed end	$1.4\ \text{s}^{-1}$	$1.4\ \text{s}^{-1}$
k_b^{-2}	Off-rate of G-ATP-Pi at the barbed end	$0.2\ \text{s}^{-1}$	$1.1\ \text{s}^{-1}$
k_b^{-1}	Off-rate of G-ADP at the barbed end	$5.4\ \text{s}^{-1}$	$7.2\ \text{s}^{-1}$
k_p^{+3}	On-rate of G-ATP at the pointed end	$11.6\ \mu\text{M}^{-1}\ \text{s}^{-1}$	
k_p^{-3}	Off-rate of G-ATP at the pointed end	$1.4\ \text{s}^{-1}$	
k_p^{-2}	Off-rate of G-ATP-Pi at the pointed end	$0.02\ \text{s}^{-1}$	
k_p^{-1}	Off-rate of G-ADP at the pointed end	$5.4\ \text{s}^{-1}$	
r_h	Hydrolysis rate of ATP	$0.3\ \text{s}^{-1}$	$0.3\ \text{s}^{-1}$
r_i	Pi release rate of interior subunits	$0.003\ \text{s}^{-1}$	$0.003\ \text{s}^{-1}$
r_i^*	Pi release rate of terminal subunits	$2\ \text{s}^{-1}$	$0.003\ \text{s}^{-1}$

Chapter 7

Cell blebbing

In this chapter, we investigate the cellular blebbing, a membrane protrusion drived by actin dynamics and acto-myosin contraction. After briefly reviewing the biological background of blebbing, we examine the mechanical components of cell blebs. Then we investigate the morphological changes of a blebbing cell under a constraint on the membrane extension. Last, the steady state of the blebbing is analyzed in a simple mechanical model where the intracellular pressure is related to the tensions in actin cortex and lipid membrane.

7.1 Background

7.1.1 Cell shape

The cell shape plays an important role in the cell physiology. Different cell types exhibit distinct resting shapes, such as those illustrated in Figure 1.1, and they may undergo a variety of morphological transformations during biological processes. A red blood cell (RBC) displays a typical biconcave shape, and undergoes extensive deformation when it squeezes through tiny capillaries [61]. By adhering to the substrate, a migrating cell translocates itself by extending membrane protrusions such as lamellipodia, filopodia and membrane blebs. During mitosis, animal cells undergo a complex sequence of transformation, from the retraction of the cell margin

and cell rounding to the later elongation and cytokinesis [62].

The equilibrium shape of a cell has been probed in the light of the shaping of artificial membrane vesicles, which are fluid sacks enclosed by a simple lipid bilayer. The vesicle adopts different shapes in response to the change of temperature and osmotic condition [63]. The vesicle shapes have been largely investigated using the curvature model, in which the equilibrium shape of a vesicle is assumed to obtain the lowest bending energy. The spontaneous curvature model (SC model) proposes that the total bending energy of a vesicle with surface area A and enclosed volume V is [61]

$$\mathcal{F} = \kappa_b/2 \oint (C_1 + C_2 - C_0)^2 \ dA + \kappa_G \oint C_1 C_2 \ dA \tag{7.1}$$

where κ_b and κ_G are the bending rigidity and the Gaussian bending rigidity, respectively. Here, C_0 is the spontaneous curvature of the membrane in the unstressed state, whereas C_1 and C_2 are the two principal curvatures of the curved membrane. The shapes of lowest energy were searched for various spontaneous curvatures and volume-area ratios. Theoretical prediction confirms that many experimentally observed shapes are among the shapes of lowest energy [63]. These include the prolate-dumbbell shapes, the pear-shaped vesicles, the oblate-discocyte shapes, and the stomatocytes. The equilibrium shape is also investigated in another curvature model, the so-called area difference elasticity model (ADE model), which differentiates two leaflets of the lipid bilayer and adds the area-difference-induced energy into the total bending energy of the model [61]. For both models, the shapes with special symmetries have been arranged into a phase diagram which classifies the shape with lowest energy under different conditions. The transitions between different shapes are continuous in the ADE model, whereas most of the transitions are discontinuous in the SC model [64]. The equilibrium and dynamics of the vesicle shape transformation derived from the bending elasticity in the energetic variational approach was numerically simulated by the phase method [65]. The equilibrium shape was extended into non-symmetric shapes in the 3D space.

Although the curvature model predicted the typical biconcave shape of RBC as the equilibrium shape under certain conditions, the contribution of cytoskeleton-membrane interaction and

intracellular pressure in the cell shape formation is not evaluated. The fluid lipid bilayer is often associated with a polymeric network on the cytoplasmic side. This could be a network passively responding to the membrane deformations. For instance, for RBC the membrane is linked to a roughly hexagonal network composed of spectrin tetramers linked at junctional complexes by integral proteins [63]. The spectrin network adds to the rigidity of the RBC membrane, and helps re-establish the biconcave shape after the cell passes through the capillaries. The drastic cell shape changes may be induced under the active forces exerted by the dynamic cytoskeleton. At the leading edge of a migrating cell, actin filaments are organized into cross-linked dendritic networks and/or the bundled finger-like shapes [2]. The membrane is deformed by the elongation of actin filaments in the normal direction of the membrane. In some cases, a thin layer of actin cortex is tangentially attached to the membrane, and the active contraction of embedded acto-myosin machinery could generate a high intracellular pressure. Whenever a pressure gradient arises in the cytoplasm, it leads to the membrane deformation. The cell shape transformation induced by the hydrodynamic pressure gradient has been studied in the motility of algal cells [66] and various cellular blebbing [67]. It remains as a big challenge for any theoretical models to determine which aspect of cell shape is determined by membrane bending energy alone and which arises from other mechanical elements such as the cytoskeleton and cytosol.

The transformation of cell shapes is closely accompanied by membrane flows. Many cells adjust their total membrane area by unfolding the microvilli membrane and invaginated membrane, or by regulating membrane exocytosis and endocytosis [68]. The lipid membrane, as a two dimensional fluid sheet, flows under shear stresses, and the flow relies greatly on the membrane tension and membrane-cytoskeleton adhesion. The membrane flow is extensively studied in membrane tether experiments, where a long, thin cylindrically shaped tether formed by the membrane detaches from the cytoskeleton when forces are exerted at a point of the cell surface. Membrane tethers have been formed for a variety of cell types, such as red blood cell, neutrophils, neurons, outer hair cells and lipid vesicles [69]. The membrane tension and membrane-cytoskeleton adhesion energy could be derived from the tether forces. The static forces of tethers from the renal epithelial cell membrane at the apical and basolateral surface,

and from membrane blebs have been measured [70], and results suggest that the membrane tension is uniform over the cell surface. In addition, the tighter membrane-cytoskeleton attachment at the basolateral portion requires larger tether forces. The tether formation on RBC shows that the elongating speed of a tether is a non-linear function of the exerted force [69]. The theoretical model proposed that different regions around the site of tether formation exhibit distinct membrane dynamics. At the distal regime far away from the site of tether formation, the lipid molecules flow around the integral proteins without affecting their binding to the cytoskeleton. At the proximal region close to the tether, the membrane velocity is high, and the integral proteins are torn out and lead to the sliding of membrane over the cytoskeleton.

7.1.2 Cell blebbing

Cell blebbing is a transient membrane bulging process [67]. In many cases, cells assemble a continuous actin cortex underneath the plasma membrane. The myosin motor molecules are associated with this thin layer of cortex, and could cause active contractions. The resultant cortical tension then leads to the buildup of a pressure difference across the cell membrane. When the cortex is tightly attached to the membrane, a high hydrostatic pressure can be maintained without deforming the cell as in the case of mitotic cells [71]. However, when the cortex is locally disconnected from membrane, the intracellular pressure drives the membrane outward and generates spherical blebs filled with cytosol.

The blebbing is commonly observed in processes such as cytokinesis, cell spreading, and locomotion of walker-carcinosarcoma and embryonic cells. It could also be a cellular response to an acute cell disease, and manifests itself as the execution stage of apoptotic cells [72]. In cell spreading and cytokinesis, the bleb is reversible in that the actin cortex reassembles underneath the bleb membrane and subsequent activation of the actin-myosin contraction machinery retracts the bleb back to the original morphology. In some migrating cells, the newly formed blebs irreversibly develop into lamellipodia to facilitate cell locomotion through the complex extracellular matrix. In apoptotic cells, the blebs eventually burst due to the continual pressure

accumulation. Although the role of blebs in these processes is not fully understood, blebs facilitating cell migration in the extracellular matrix have been discovered (reviewed in [73, 74]).

Experiments have been carefully designed to induce artificial blebs in order to understand the underlying mechanisms. Different cells form blebs of various patterns through distinct mechanisms [75]. Two experiments described below exemplify the main biochemical and mechanical processes involved in the blebbing phenomenon, and reveal two distinct blebbing mechanisms.

7.1.3 Blebbing of M2 cells

In one case, it was observed that filamin-deficient melanoma cells (M2) constitutively bleb for hours [76]. These cells develop many dynamic blebs simultaneously throughout the plasma membrane as shown in Figure 7.1. All blebs display a similar dynamic cycle: namely, bleb nucleation marked by membrane detachment from the underlying cortex, bleb growth with expanding membrane surface, and retraction where reassembled acto-myosin cortex contracts and pulls the bleb back to the cell body (see Figure 7.2).

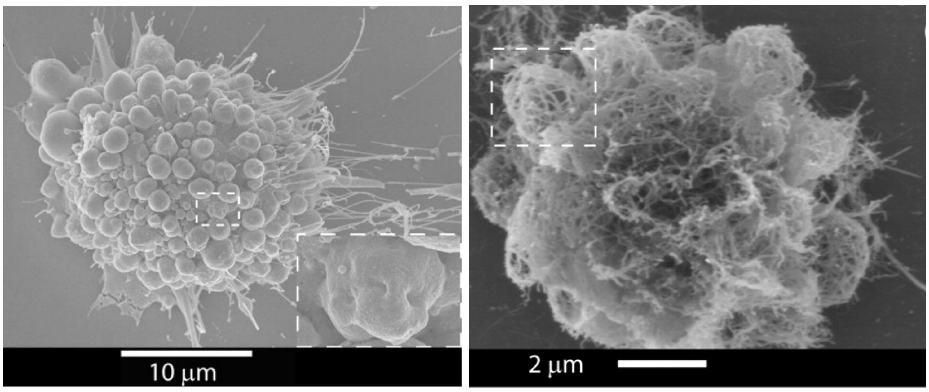

Figure 7.1: The blebs of M2 cells and underlying actin structures (from [77]).

Biochemical manipulations reveal that the following mechanical properties and interactions of component materials are critical for the blebbing [76]. First, the membrane rigidity influences the blebbing since increasing membrane rigidity by crosslinking the glycocalix polysaccharides

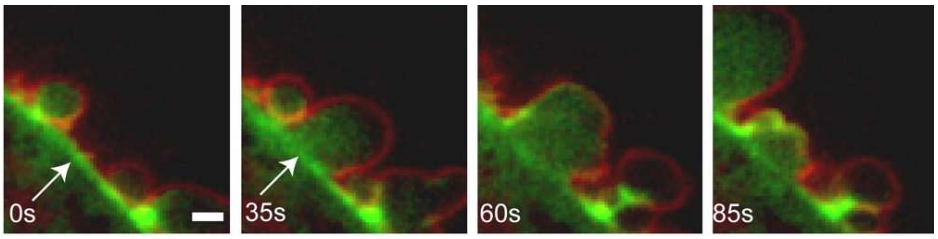

Figure 7.2: A representative blebbing cycle of M2 cells (from [77]).

with wheat germ agglutinin (WGA) inhibits blebbing. Second, the adhesion energy of the actin cortex to the membrane is a great factor for the blebbing, since melanoma cells with filamin exhibit no blebbing. The filamin protein has dual functions: crosslinking actin filaments into orthogonal networks in the cortical cytoplasm, and participating in the anchoring of membrane proteins for the actin cytoskeleton. In addition, it has been reported that the micro-injection of dominant active ezrin-T567D-GFP inhibited blebbing, since this protein enhances the actin-membrane attachment. The membrane-cortex adhesion energy is postulated to directly affect the nucleation and size of blebs. The adhesion tightness also influences the bleb growth indirectly. The tighter the membrane is attached to the cortex, the greater the resistance force the membrane flow needs to overcome. Third, the actin-myosin contraction is the driving force for blebbing. Injecting the blebbing cells with inhibitors of myosin II (blebbistatin) and ROCK1 (Y-27632 and 3-(4-pyridyl)indole) suppresses the blebbing. The F-actin-disrupting agents cytochalasin D and latrunculin B destroy the actin cortex and inhibit the blebbing accordingly.

The bleb can also be induced by the local destruction of the actin cortex in the mitotic animal cells as shown in Figure 7.3. When a cell is blocked in the metaphase, the cell displays a round morphorology due to the high resting intracellular pressure. The local treatment of Latrunculin, an actin monomer sequestration protein, weakens the actin cortex, which locally induces membrane blebs of various sizes in the presence of intracellular pressure.

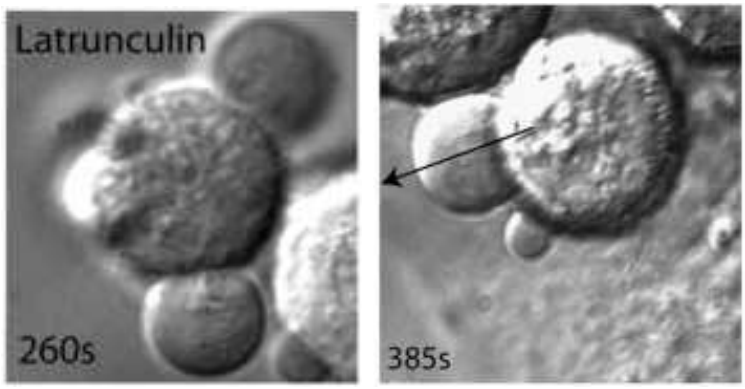

Figure 7.3: The blebs induced by local treatment of Latrunculin in two mitotic cells (from [71]). The times labelled in the figures indicate the time after the drug treatment.

7.1.4 Blebbing of NZ-treated detached fibroblast cells

Another distinct pattern of cell blebbing takes place in Nocodazole(NZ)-treated Murine L929 fibroblast. Similar bleb dynamics is observed in NZ-treated human KE37 lymphoblastic cells. The NZ treatment disassembles microtuble cytoskeleton (MTs), and elevates actomyosin contractility. When the cell is detached from the substrate, the following oscillatory behavior persists for at lease 6 hours as shown in Figure 7.4. The underlying actin cortex is first locally ruptured, and a constriction ring forms along the periphery of the ruptured hole. On one side of the constriction ring, the actin-devoid membrane bulges out and is filled with cytosol. On the other side, the cortex is contracting, and causes continuous surface shrinkage. The cytoplasmic space with actin linings continually contracts until the entire cytosol flows into the bleb. In most cases, as the bleb becomes the main cell body, the contracting part forms only a knot. After a delay, the cortex ruptures at a site close to the birth place of previous constriction ring, new constriction ring forms, and a new cycle repeats. This oscillatory behavior is also observed in enucleated cell fragments from L929 fibroblast cells. However, no development of a lamellipodium is reported for cell fragments. The dynamic profiles of both actin and Myosin II distribution indicate that the actin cortex associated with Myosin II is present in the contracting part of the cell during the entire blebbing cycle, whereas the actomyosin cortex emerges only

at the late stage of blebbing as shown in Figure 7.5 and 7.6. The blebbing oscillation lasts for at least 8 hours. The oscillation is spontaneous behavior of the NZ-treated detached whole cell or cell fragments. Thus it provides us with a well-defined system to investigate the blebbing phenomenon.

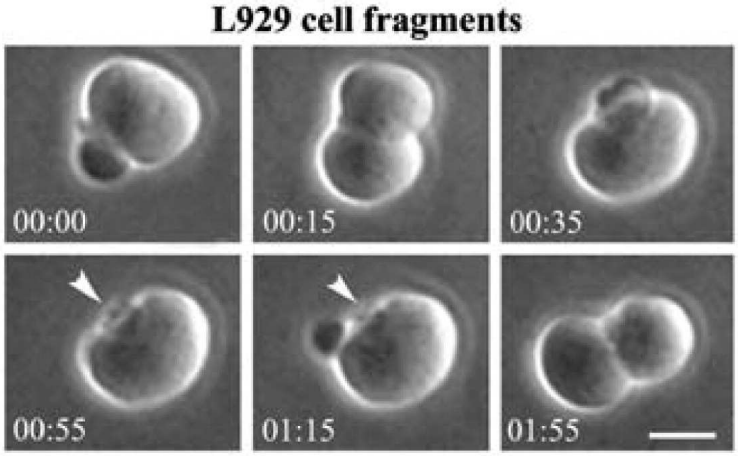

Figure 7.4: The blebbing of L929 cell fragments (from [78]). Scale bar, 5 μm

Blebbing in a L929 cell is distinct from that in a M2 cell in at least two features. First, the morphology of L929 cell bleb differs from M2 cell bleb in that in most cases only one bleb is spotted in the L929 system and it can absorb the entire cytoplasm. The cortex-membrane adhesion and intracellular pressure are thought to be the determining factor to differentiate these bleb types. Second, the bleb is initiated with local rupture of actin cortex in L929 whereas the membrane is peeled off in M2 cells.

7.2 Mechanical elements of cell blebbing

The two experiments described above give us a general working model of cell blebbing: acto-myosin contraction generates intracellular hydrostatic pressure, which in turn drives the actin-void plasma membrane to form blebs. Reassembly of acto-myosin cortex under the bleb membrane retracts the bleb.

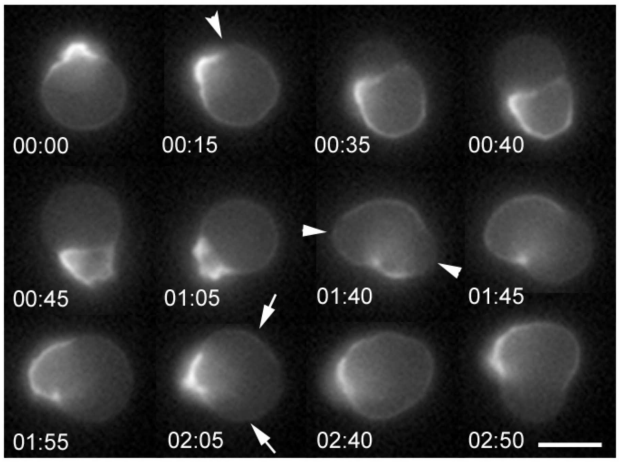

Figure 7.5: The dynamic profile of actin distribution during the blebbing of L929 cell fragments (from [78]). White arrowheads suggest the rupture hole in the actin cortex, whereas the white arrows indicate the place where actin is recruited to the membrane. Scale bar, 5 μm.

In this picture of blebbing, a minimal set of three structural components is required: namely, plasma membrane, acto-myosin cortex and cytosol. The characteristics of materials for each components and their mechanical response to passive/active force are the main focus of the blebbing modelling. We will examine the properties of three component pieces and their mechanical interactions in detail.

7.2.1 Plasma membranes

The cell membrane is a two-dimensional structure composed of lipid molecules. Lipid molecules under tension can flow within the membrane surface, i.e. they exhibit a degree of fluidity [79]. The membrane can sustain a maximal area expansion around 2-5% [61]. In blebbing M2 cells, experimental results indicate an erythrocytic sub-membranous cytoskeleton might exist, which regulates the membrane integrity and modifies the flow viscosity as well. There is no evidence indicating the presence of such membrane-skeleton for all blebbing cells. However, we can always treat the sub-membranous skeleton as an inseparable part, and it only changes the parameters of intrinsic material properties while maintaining the characteristic material behavior.

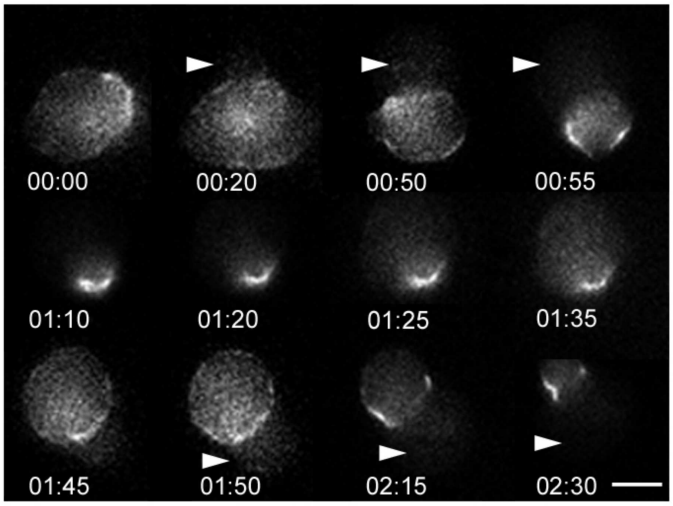

Figure 7.6: The dynamic profile of Myosin II distribution during the blebbing of L929 cell fragments (from [78]). The white arrowheads indicate the growing bleb which is devoid of Myosin II. Scale bar, 5 μm.

The plasma membrane can be modeled as a 2D viscoelastic surface material [79]. How to treat the dynamics of the membrane at the location of constriction ring poses a big challenge. Lipid molecules may flow across the constriction ring from one domain to the other. One approach is to treat the bleb membrane and cell-body membrane as two adjacent but distinct domains. The flow of lipid molecules into or out of a domain is regarded as the positive or negative growth for the membrane within that domain.

7.2.2 Actin-myosin cortex

The actin cortex is a thin layer of actin-rich lining beneath the membrane. Its thickness is on the order of tens of nanometers. The cortex of M2 cell blebs is 10-20 nm thick, whereas the cortex of HeLa cell arrested in metaphase is about 50-100 nm. Strikingly, the actin cortex is assembled in cross-linked layers and is aligned tangentially with the membrane [77]. A rough estimate shows a cortex about 200 nm [78]. It was proposed that the thicker actin cortex produces the higher intracellular pressure [71].

Myosin II motor molecules are aggregated in foci in the actin networks. The action of myosin exerted on the underlying actin structure leads to contraction, observed both *in vivo* and *in vitro* [80, 78]. How the actin cortex deforms according to the myosin contraction remains unknown.

7.2.3 Cytoplasm

Enclosed by the plasma membrane is a gelatinous, semi-transparent fluid, called cytoplasm, and the nucleus surrounded by cytoplasm. The cytoplasm has three major elements; the cytosol, organelles and inclusions. The cytoplasm was simply treated as either a Newtonian or a viscoelastic fluid in most cell models. Other findings suggested, however, that the cytoplasm resembles a poroelastic material, for which the fluid flow is restrained by a porous and elastic solid structure. The postulate is supported by two lines of evidence. In one experiment, the local suppression of acto-myosin contraction inhibits the blebbing only at the treated location [76]. This was interpreted to mean that the pressure propagation in the cytoplasm is far slower than in a Newtonian or a viscoelastic fluid. Other evidence is that locally elevated osmoticity generates a slow drainage of fluid across the cytoplasm [81]. In L929 cell fragments, the cytosol can be modelled as an incompressible Newtonian fluid, because the cell fragment is devoid of its nucleus, and the cytoplasm is simpler than when the nucleus is present. The cytoplasm then simply serves to transduce the force induced by acto-mysoin contraction to the cross-membrane pressure difference for bleb expansion.

7.2.4 Interactions between components

A sucessful blebbing results from the coordinated interactions between the component elements as described above. The cortex-membrane coupling is mediated by the linker proteins, which attach the actin cortex to the membrane. On the subcellular scale, the membrane can be viewed to adhere to the cortex in a continuous manner. A patch of membrane is subjected to a cross-membrane pressure difference in the normal direction and an adhesive force from the cortex.

When the pressure difference reaches a critical level, the attachment is disrupted and the membrane separates from the cortex. In contrast, a firm adhesion prevents the membrane detachment from the underlying cortex. The tearing of membrane off the cortex resembles the fracturing of composite material. The association of membrane with cortex could also impede the flow rate of lipid molecules within the membrane surface. Another important interaction is between the membrane and cytoplasm. In a balanced state, the membrane tension is related to the cross-membrane pressure by the Laplace's law. Any pertubation on the membrane and cortex may lead to the cytoplasm flow and membrane deformation.

7.3 Constraints on the cell configuration during blebbing

The blebbing of L929 cell fragments results in a highly dynamic membrane deformation as shown in Figure 7.4. The total membrane surface area is undergoing significant changes during the blebbing. However, the lipid membrane ruptures when the area expansion is beyond 2-5% [61]. Apart from the mechanics, we first ask the question: how does the cell control its dynamic configuration to aviod the membrane rupture?

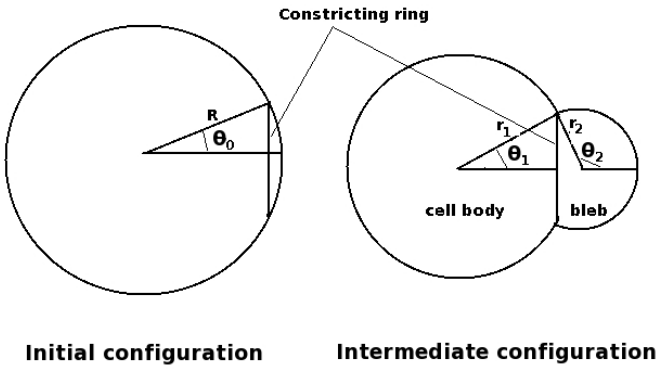

Figure 7.7: The dimensions of a blebbing cell.

The epxerimental results indicated that the cell maintains a constant total volume during the blebbing. The cell is devided into the cell body and bleb domains, which are jointed by

a constriction ring. To get insight into the changes of total membrane surface, we assume a symmetric geometry for the blebbing cells as depicted in Figure 7.7. Suppose that the cell before blebbing is of radius R. Let us first assume that the constriction ring is fixed with radius $R\ \sin\Theta_0$, where Θ_0 is the angle between the zenith direction and the line formed between the cell center and constriction ring as defined in spherical coordinates. We want to examine the changes of total membrane area accompanying the gradual flow of cytoplasm from the cell body into blebs. Suppose the dimensions of the two domains are determined by parameters $\{r_1, \theta_1\}$ and $\{r_2, \theta_2\}$, respectively.

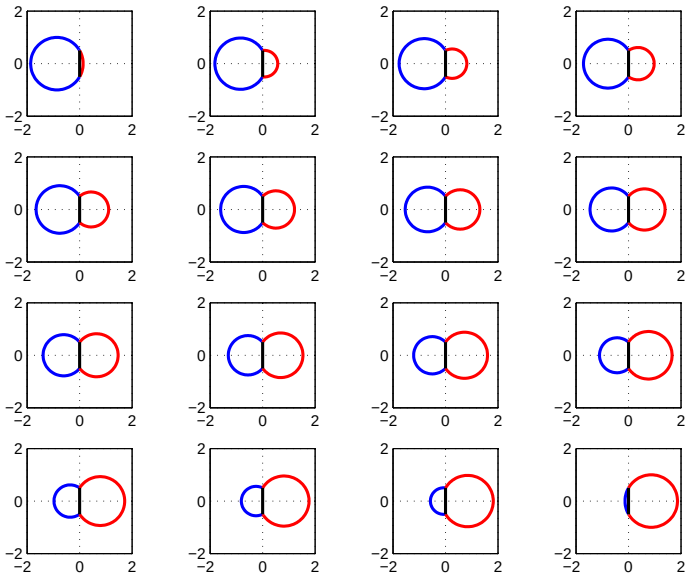

Figure 7.8: An example of the configuration changes accompanying the blebbing. The constriction ring (black) takes place at $\Theta_0 = \pi/6$, dividing the cell into a contracting domain (blue) and blebbing domain (red).

At any instant of time, we have

$$R\sin\Theta_0 = r_1\sin\theta_1 = r_2\sin\theta_2 \tag{7.2}$$

which describes a fixed constriction ring. The conservation of total cellular volume requires that the total cellular space (V_0), as the sum of contracting domain (V_1) and blebbing domain

(V_2), is constant, i.e.

$$\begin{aligned}\frac{4}{3}\pi R^3 &= \left(\frac{2}{3}\pi r_1^3 + \pi r_1^3\cos\theta_1 - \frac{1}{3}\pi r_1^3\cos^3\theta_1\right) \\ &\quad + \left(\frac{2}{3}\pi r_2^3 - \pi r_2^3\cos\theta_2 + \frac{1}{3}\pi r_2^3\cos^3\theta_2\right) \end{aligned} \tag{7.3}$$

The ratio of initial bleb volume over total volume, x_0, is defined as

$$x_0 = \frac{V_2}{V_0} = \frac{2 - 3\cos\Theta_0 + \cos^3\Theta_0}{4} \tag{7.4}$$

The dynamic increase of membrane area is

$$\Delta S = S_1 + S_2 - S_0 = 2\pi r_1^2(1+\cos\theta_1) + 2\pi r_2^2(1-\cos\theta_2) - 4\pi R^2 \tag{7.5}$$

Define the radius ratios as

$$u = r_1/R, \quad v = r_2/R$$

and the volume fraction of the bleb domain, x, as

$$V_1 = (1-x)V_0, \quad V_2 = xV_0 \tag{7.6}$$

The membrane expansion ratio, defined as the ratio of the increase in membrane area over the initial membrane area, becomes

$$\Delta S/S = u^2(1+\cos\theta_1)/2 + v^2(1-\cos\theta_2)/2 - 1 \tag{7.7}$$

The conditions of equations (7.2) and (7.6) imply that the contracting-domain variables solve

$$16(1-x)u^3 - 3u^2\sin^4\Theta_0 - \left(16(1-x)^2 + \sin^6\Theta_0\right) = 0 \tag{7.8}$$

$$\cos\theta_1 = \frac{4(1-x) - 2u^3}{2u^3 + u\sin^2\Theta_0} \tag{7.9}$$

and the blebbing-domain variables satisfy

$$16xv^3 - 3v^2\sin^4\Theta_0 - \left(16x^2 + \sin^6\Theta_0\right) = 0 \tag{7.10}$$

$$\cos\theta_2 = \frac{2v^3 - 4x}{2v^3 + v\sin^2\Theta_0} \tag{7.11}$$

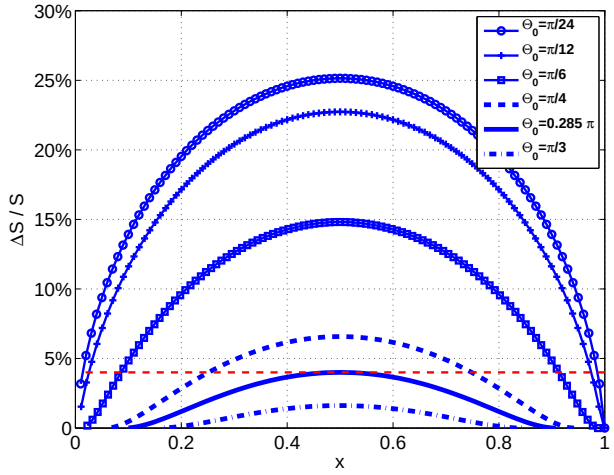

Figure 7.9: The membrane surface expansion over the bleb volume fraction at various constriction ring sizes. The horizontal dashline marks a fixed membrane expansion level $\Delta S/S = 4\ \%$.

Thus, equations (7.7)-(7.11) indicate that the membrane expansion ratio is a function of x, i.e.,

$$\Delta S/S = f(x, \Theta_0) \tag{7.12}$$

We assume that the blebbing cell at both the initial and end states is spherical, and the parameter x ranges from x_0 to $1 - x_0$. A schematic of the blebbing cycle is depicted on Figure 7.8. The increase of total surface area is calculated from (7.7). The membrane expansion is numerically solved as a function of x and the result is shown in Figure 7.9. It shows that the membrane continuously expands as the bleb enlarges, and it achieves a maximal stretching when the bleb takes half of the total volume. As the bleb expands further, the membrane stretching reduces. The membrane activities with varying constriction ring size are compared. For all ring sizes, the maximal membrane expansion occurs at the same configuration state where the bleb takes half of the cell volume. The maximal membrane expansion as a function of the ring size is depicted on Figure 7.10. The maximal membrane stretch decreases as the ring size increases. When the ring is extremely small, the maximal stretch could reach more than 25%.

The above result implies that, by adjusting the constriction ring, the cell can bleb and avoid membrane rupture. We therefore solve the minimal sizes of the constriction ring as the bleb

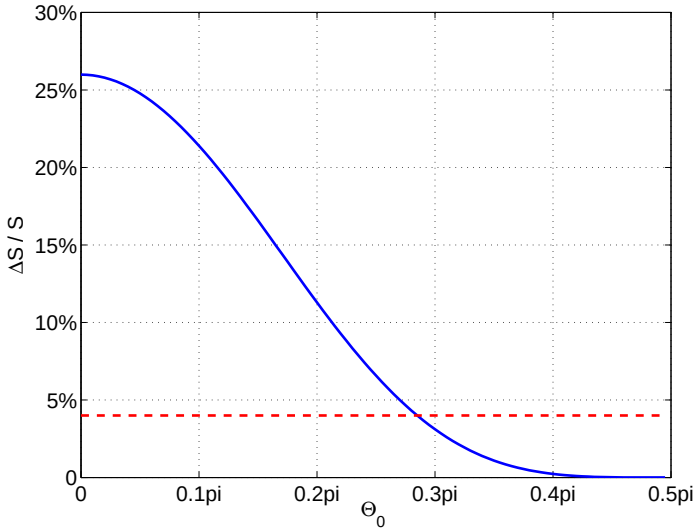

Figure 7.10: The dependence of maximal membrane stretching on the ring sizes. The dashline marks the lysis value of membrane expansion $\Delta S/S = 4\ \%$.

enlarges and the membrane expansion is maintained below a critical level. In our simulations, we take the critical level to be 4%, which lies within the lysis expansion range measured in the lab. As Figure 7.11 shows, the constriction ring should expand as the bleb enlarges to ensure a less-than 4% membrane stretching. In the curve, $\Theta_0^* = \Theta_0^*(x)$ is obtained from the membrane stretch function $f(x, \Theta_0^*) = 4\%$. During the blebbing process, the largest constriction ring is required when the bleb absorbs half of the cytosol, and the maximal ring size is approximately $\Theta_0 = 0.285\pi$.

Our analysis is based on the assumption that the membrane is fully extended during the blebbing. Thus, the membrane unfolding and exocytosis is excluded. We established that the constriction ring must enlarge before the bleb takes half of the cytosol, which is consistent with the experiment result as depicted in Figure 7.4. In vivo, no obvious membrane folding and secretion is observed. Therefore, one can assume that the membrane is fully extended at the outset of blebbing.

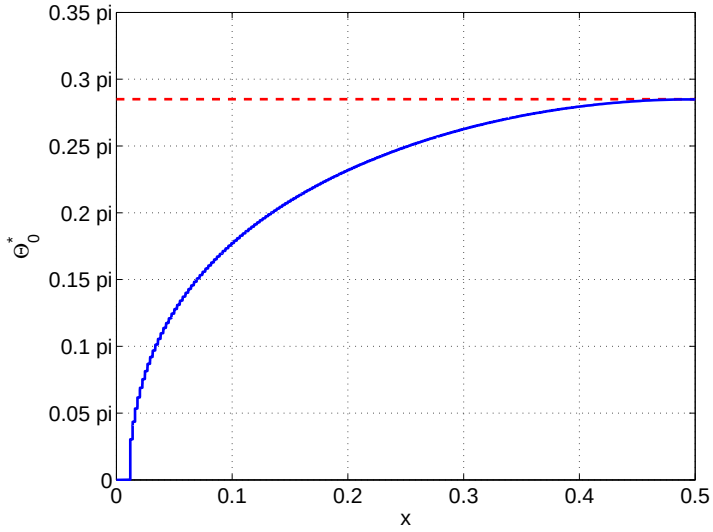

Figure 7.11: The minimal constriction ring size to prevent the membrane rupture during the blebbing. The dashline is $\Theta_0 = 0.285\ \pi$.

7.4 A mechanical model for the equilibrium state of blebbing

In the previous section, we estimated the accessible configurations for a blebbing cell with the constraint that the plasma membrane stretches less than 4% of its initial surface area. No mechanics of the membrane and actin cortex is considered there. In addition, the membranes of cell body and cell bleb are not distinguished. In the following, we investigate how a blebbing cell establishes its equilibrium shape by balancing the intracellular pressure with the tensions of actin cortex and membrane. The model system is the mitotic cell where membrane blebs of various sizes could be induced by local treatment of Latrunculin as shown in Figure 7.3.

7.4.1 Model description

Before the perturbation of membrane-cortex adhesion, the cell is assumed to be spherical with a radius R, and is under mechanical balance whereby the tensions of the actin cortex and membrane maintain a cross-membrane pressure difference as depicted in Figure 7.12 (left). Suppose

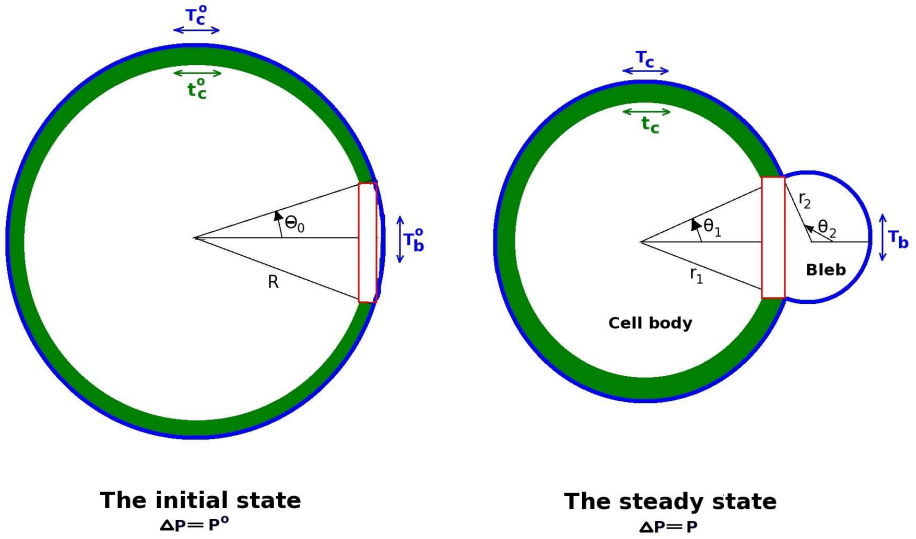

Figure 7.12: The illustration of the shape and mechanics of a blebbing cell. The outer layer of the cell cortex is the very thin lipid bilayer, which in turn is attached to a layer of actin linings from the cytoplasmic side. The red rectangular area represents the constriction ring separating the contracting cell body domain and the blebbing domain. The cross-membrane pressure is denoted by ΔP. The parameters are explained in the text.

the pressure difference is P^0, and the membrane and actin cortex are subjected to uniform tensions of T_c^0 and t_c^0, respectively. The Laplace's law reads

$$T_c^0 + t_c^0 = \frac{R \cdot P^0}{2} \tag{7.13}$$

At the outset of blebbing, a patch of membrane is suddenly detached from its actin lining. Let the size of the bleb membrane be characterized by the angle Θ_0 as defined in Section 7.3. We assume the tension of bleb membrane is initially equal to that of the actin-associated membrane, i.e.

$$T_b^0 = T_c^0 \tag{7.14}$$

The detachment of actin cortex from the membrane triggers the ballooning out of a bleb. Suppose the cell ceases blebbing at a steady state as illustrated in Figure 7.12 (right). We first assume the constriction ring is fixed. The constriction ring separates the cell into two adjacent

domains: namely, the cell body domain of radius r_1, and the bleb domain of radius r_2. The relative size of the constriction ring to each domain is characterized by θ_1 and θ_2, respectively as plotted in Figure 7.12. For the cell body domain, the membrane and actin cortex is under a tension of T_c and t_c, which balances with a cross-membrane pressure difference P. The bleb membrane is under a surface tension T_b. According to the Laplace's law, one has at the steady state

$$T_c + t_c = \frac{r_1 \cdot P}{2} \tag{7.15}$$

$$T_b = \frac{r_2 \cdot P}{2} \tag{7.16}$$

We postulate that at a steady state the acto-myosin complex is under the maximal contractile stress that it can generate, and propose that at the steady state the cortex is under a constant uniform tension, which is determined by the maximal acto-myosin contractile force. Accordingly, we have a constant cortex tension at a steady state as in the initial state, i.e.

$$t_c = t_c^0 \tag{7.17}$$

The membrane tension is generated by the area expansion from its unstressed state. At the steady states, the membranes of the cell body and bleb domains are assumed to be uniformly stretched within each domain. Suppose that in the initial state the membrane of the cell body and the bleb is stretched from the unstressed area of S_C and S_B to the stressed state with area of S_c^0 and S_b^0, respectively. In addition, we assume that the membrane tension is proportional to the membrane expansion ratio with a rigidity constant λ. Therefore,

$$T_c^0 = \lambda \frac{S_c^0 - S_C}{S_C} \tag{7.18}$$

$$T_b^0 = \lambda \frac{S_b^0 - S_B}{S_B} \tag{7.19}$$

where

$$S_c^0 = 2\pi R^2 (1 + \cos\Theta_0) \tag{7.20}$$

$$S_b^0 = 2\pi R^2 (1 - \cos\Theta_0) \tag{7.21}$$

At the steady state, the membrane surface area is S_c and S_b for each domain, and then

$$S_c = 2\pi r_1^2(1+\cos\theta_1) \tag{7.22}$$

$$S_b = 2\pi r_2^2(1-\cos\theta_2) \tag{7.23}$$

To take account of the possible lipid flux across domains, the lipid membrane flows from the cell body domain into the bleb is assumed to be $m * S_C$, where $m \in [0,1)$. Therefore, one relates the tension to the surface expansion at equilbrium as

$$T_c = \lambda \frac{S_c - (1-m)S_C}{(1-m)S_C} \tag{7.24}$$

$$T_b = \lambda \frac{S_b - (S_B + mS_C)}{S_B + mS_C} \tag{7.25}$$

If the volume fraction of bleb over total cell volume is x^* at the steady state, the radius of cell body and bleb can be obtained analytically from (7.8) and (7.10), which are rewritten as

$$16(1-x^*)\left(\frac{r_1}{R}\right)^3 - 3\left(\frac{r_1}{R}\right)^2 \sin^4\Theta_0 - \left(16(1-x^*)^2 + \sin^6\Theta_0\right) = 0 \tag{7.26}$$

$$16x^*\left(\frac{r_2}{R}\right)^3 - 3\left(\frac{r_2}{R}\right)^2 \sin^4\Theta_0 - \left(16x^{*2} + \sin^6\Theta_0\right) = 0 \tag{7.27}$$

7.4.2 The steady state and its stability

In theory, one can solve the steady state from equation (7.13)-(7.27) provided that the initial condition and the parameters (R, Θ_0, λ, m) are given. Observing the high non-linearity of these equations, we instead seek the numerical solutions as follows. We perturb the volume fraction of the bleb while keeping other paramters fixed. The membrane tensions and sizes of the cell body and bleb are uniquely determined by the volume fraction of bleb x. If the membrane tension equilibrates the cross-membrane pressure locally, one has the local pressure for the cell body domain

$$P_c = 2(T_c + t_c)/r_1 \tag{7.28}$$

whereas the cross-membrane pressure for the bleb

$$P_b = 2T_b/r_2 \tag{7.29}$$

We note that the right hand side of (7.28) and (7.29) is a function of x, i.e. $P_c = P_c(x), P_b = P_b(x)$. Since the intracellular pressure is uniform in the cytosol at a steady state, one expects $P_c = P_b$. Thus the volume fraction x^* is a steady state if

$$P_c(x^*) = P_b(x^*) \tag{7.30}$$

Furthermore, the state x^* is stable if, in a neighborhood of x^*, $P_c(x) > P_b(x)$ when $x < x^*$ and $P_c(x) < P_b(x)$ when $x > x^*$. When the bleb volume fraction is slightly less than a stable x^*, the cell-body membrane and cortex generate a higher pressure than the bleb membrane alone since $P_c(x) > P_b(x)$. The pressure gradient would expand the bleb volume until the bleb volume is equal to the stable state. Similarly, the pressure gradient would drive the bleb back to its stable state when the volume is slightly higher than the stable state.

For numerical simulations, we choose the parameters from the blebbing experiment conducted on animal cells arrested in the metaphase [71]. A typical cell used in that experiment has a radius 10 μm. The intracellular hydrostatic pressure is estimated as 45-300 Pa. In our numerical simulations, we choose the default value as $P^0 = 300$ Pa. Since the bilayer lipid membrane is lytic at the expansion around 4% and the tension ~ 0.01 N/m, we use the membrane rigidity as $\lambda = 0.25$ N/m. Thus a pure lipid membrane vesicle of radius 4 μm can sustain a pressure up to $5,000$ Pa. As in equation (7.13), the initial intracellular pressure is maintained by the stretching of both actin cortex and membrane. The relative contributions of these two have not been measured in experiments. So, we arbitrarily choose the contribution of actin cortex to be 75%, i.e. $t_c^0 = 3\, T_c^0$. The default size of constriction ring is $\Theta_0 = \pi/6$.

Due to the unknown lipid flows, we thus investigate the equilibrium state of the blebbing in three cases. First, we suppose that the cell establishes the equilibrium state with no lipid molecules flowing between domains, i.e. $m = 0$. Then, the bleb is probed by assigning a lipid flow from the cell body into blebs, i.e. $m > 0$. Last, we will consider lipid molecules flow so that the blebbing cell maintains a globally uniform membrane tension, i.e. $T_b = T_c$.

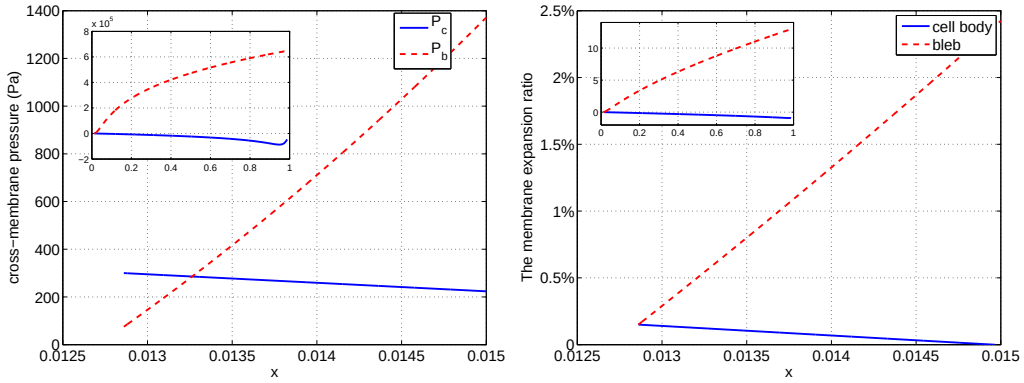

Figure 7.13: The membrane extension and cross-membrane pressure corresponding to bleb growth. No membrane flow is allowed. The constriction ring size is $\Theta_0 = \pi/6$.

7.4.3 The case with no cross-domain membrane flow

We first examine the case where no membrane is allowed to flow across the constriction ring, i.e. $m = 0$. To solve for the steady state, we gradually increase the bleb volume. The putative cross-membrane pressures in the cell-body domain and bleb domain defined as in (7.28) and (7.29) have different behavior as shown in Figure 7.13. It indicates that at the outset of blebbing the cortex and membrane of the cell body produces a higher pressure than the blebbing membrane alone, which would lead to the cytosol flow and membrane deformation. This agrees with the experimental results that interrupting the membrane-cortex attachment triggers the blebbing. As the bleb volume increases, the bleb membrane can sustain a higher pressure, whereas the cell body can endure a reduced pressure. This is because of the increased expansion of bleb membrane and reduced cell-body membrane stretching. Since there is only one intersection for the curves of P_c and P_b, the equilibrium state of the blebbing is unique according to (7.30). As shown in Figure 7.13, the local behavior of P_c and P_b suggests the steady state is stable. A small perturbation on the bleb size would relax unto the steady state. At the steady state, the bleb membrane is stretched more than the cell body membrane, thus it is subjected to larger membrane tension. By observing that the resting intracellular pressure at the steady state is lower than that in the initial state, we conclude that without membrane flow the establishment

of the equilibrium blebbing configuration tends to reduce the intracellular hydrostatic pressure. Our numerical results show that the intracellular pressure is always reduced at the equilibrium configuration after partial cortex detachment if no membrane flow from one domain to the other.

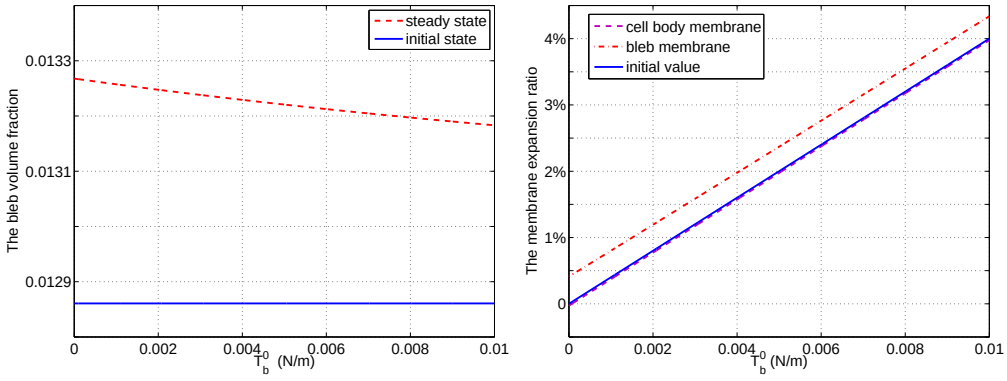

Figure 7.14: The steady-state bleb volume and membrane extension corresponding to elevated initial membrane tensions.

We examined the influence of material properties of cells on the blebbing and compared with *in vivo* observations. We first consider the condition where the initial membrane tension (T_b^0) is elevated but the cortex tension (t_c^0) is fixed, which leads to an increased initial intracellular pressure. This mimics the cell blebbing in osmotic swelling experiments [78], where initially the cell membrane is under higher tension due to increased internal pressure. We observe that the equilibrium bleb volume decreases with the initial membrane tension as shown in Figure 7.14 (left). Therefore, a potential osmotic swelling increases the initial membrane tension, and thus suppresses the bleb activities. The examination of the membrane expansion indicates the equilibrated bleb membrane is always stretching more extensively than the initial state, whereas the cell body membrane is slightly relaxed.

In vivo experiments shows that the increased membrane rigidity would inhibited the blebbing [76]. We modify the membrane rigidity constant λ among a broad range. Results as in Figure 7.15 show that the resting bleb volume is suppressed by increased λ, which is consistent with experimental observation that the blebbing is inhibited by high membrane rigidity. At the steady state, the bleb membrane is under higher tension than the cell body membrane.

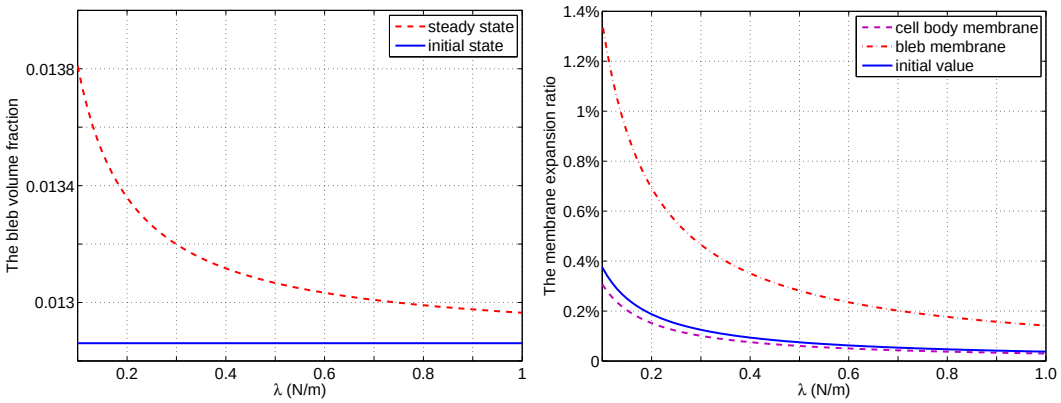

Figure 7.15: The steady-state volume fraction of bleb and membrane expansion corresponding to various membrane rigidity.

Another perturbation is to vary the size of the constriction ring, which is presumably due to the cortex rupture or depolymerization. We observed that increasing the patch size of the membrane detached from the actin cortex results in a increased bleb expansion as shown in Figure 7.16. However, the bleb volume change remains small. With enlarged constriction ring, the resting intracellular pressure is reduced. This suggests that when more membrane is dissociated from actin cortex, the intracellular pressure drops more at the equilibrium state.

In summary, we have investigated the equilibrium states of blebbing with no membrane flow. The bleb membrane is subjected to a higher tension than the cell-body membrane, since the membrane-cortex dissociation drives the cytosol to fill the expanding bleb. One consequence of the blebbing is to relax the intracellular hydrostatic pressure. We also confirm that increasing membrane rigidity and osmotic swelling would suppress the blebbing.

7.4.4 The case with positive cross-domain membrane flow

In the following, we examine the steady state of blebbing by allowing the lipid membrane to flow from the cell body to the bleb, i.e. $m > 0$. Numerical results show that, for a small constriction ring, the steady state of blebs is unique for increasing the membrane flow $m \in [0, 1)$ as displayed in Figure 7.17 (left). The larger the membrane flow is, the greater volume the bleb

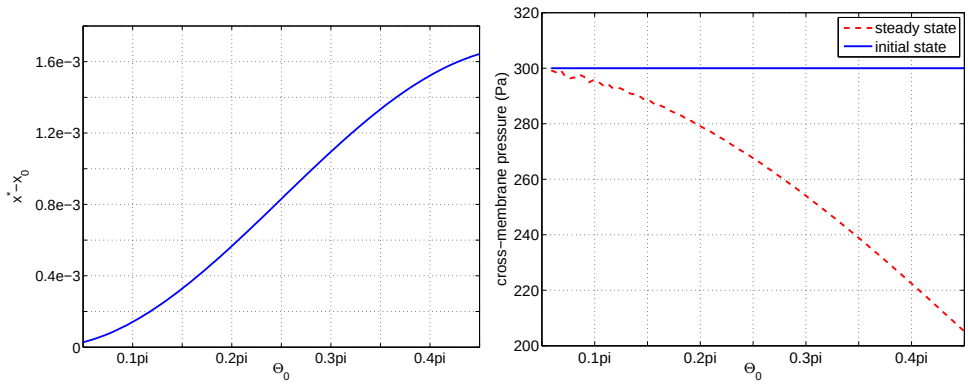

Figure 7.16: The bleb volume changes and intracellular pressure at the steady state corresponding to varying cortex-membrane detachment.

has in equilibrium. At small constriction ring, the resting intracellular pressure is parabolic in terms of membrane flow. The equilibrium pressure is rising first with increased membrane flow, and falling with higher flow as shown in Figure 7.17 (right). It also reveals that with membrane flow, the blebbing process is able to raise the intracellular hydrostatic pressure, compared to the initial pressure in the cytosol, which is 300 Pa in our simulations. The comparison of membrane expansion in the two domains shows that the bleb membrane is under greater tension only in the low and high membrane flow range, whereas the cell-body membrane tension is higher in the intermediate range of m as depicted in Figure 7.18. However, for large constriction ring a steady state of blebs cannot be obtained when the prescribed flow is greater than a critical level, which is seen as the discontinuity at the high m and Θ_0 corner in Figure 7.17.

In summary, for a fixed constriction ring, the magnitude of membrane flow from the cell body into the bleb dictates the equilibrium bleb state. A steady state of cell configuration may not exist for high membrane flow and large constriction rings. The incorporation of membrane flow facilitate to maintain the a higher intracellular pressure after blebbing than before blebbing. The bleb membrane may experience less tension than cell-body membrane in certain range of prescribed membrane flow. In contrast, without membrane flow the bleb membrane is always under higher surface tension.

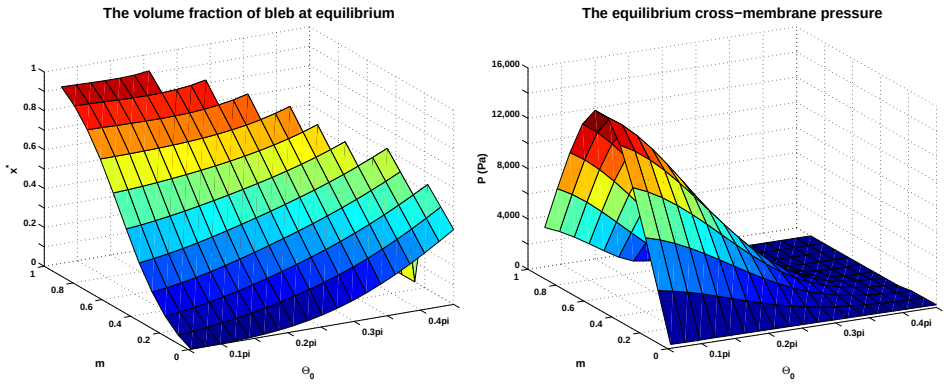

Figure 7.17: The steady-state volume fraction of blebs and intracellular pressure corresponding to various Θ_0 and m. Here Θ_0 denotes the size of the constriction ring, where m stands for the percentage of membrane fluxing from the cell-body membrane to bleb membrane.

7.4.5 The case with uniform membrane tension

In the previous sections, we have considered the steady state of blebbing with predetermined direction and extent of membrane flow between cell domains. In particular, we examined the cases with no membrane flow and with positive membrane flux from the cell body into the bleb. In both cases, the constriction ring serves as a barrier for the possible lipid flow. The prediction shows that the bleb membrane might be subjected to a surface tension different from the cell body membrane at equilibrium in these cases. However, to our best knowledge, the tensions of both the cell-body membrane and bleb membrane have not been directly measured and compared in experiments. There is another possibility that the lipid molecules flow around the cell surface to ensure a globally uniform tension. Acccordingly, at an equilibrium configuration the membrane tension must obey $T_b = T_c$.

To take into account this type of lipid flow, we abandon the prescription of membrane flow (m), and pose instead on the membrane expansion the constraint of $T_b = T_c$. In particular, at the steady state, the tensions T_c and T_b are not determined by (7.24) and (7.25), but they are derived from (7.7) as

$$T_c = T_b = \lambda \, \Delta S/S \tag{7.31}$$

We obtained the numerical solution of the steady state of the blebbing in the same procedure

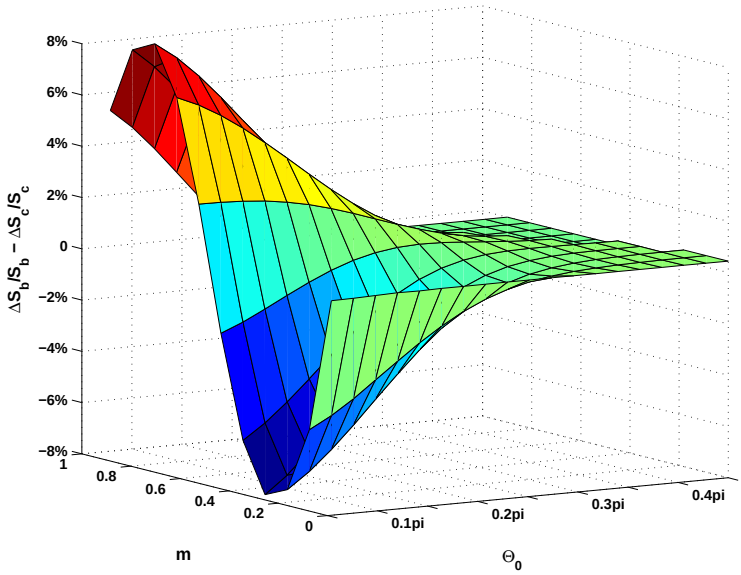

Figure 7.18: The difference of membrane expansion in the cell body and blebs corresponding to various Θ_0 and m.

as applied in previous sections. First, we examined the case with a small fixed constriction ring, where $\Theta_0 = \pi/6$. The numerical result shows that as the bleb enlarges, the membrane expansion ratio is a bell-shape function of the bleb volume, and the curve is symmetric with repect to $x = 0.5$ as displayed in Figure 7.19 (right). As the bleb size changes, the membrane tension is modified accordingly. The numerical result shows that the cross-membrane pressure differences P_c and P_b as defined in (7.28) and (7.29) are both bell-shape function of the bleb volume x as depicted in Figure 7.19 (left). The curves of P_c and P_b intersects twice, which suggests two steady states according to (7.30). For $\Theta_0 = \pi/6$, one equilibrium state occurs when the bleb volume is around 3% of the total cytoplasm. The resting pressure for this equilibrium state is 554 Pa, which is higher than the initial pressure of 300 Pa. Furthermore, the local behavior of P_c and P_b indicates that this steady state is stable according to the discussion in Section 7.4.2. On te contrary, the other equilibrium state occurs at $x \approx 47\%$, and is unstable. In addition, the membrane is stretched beyong 14% at this state, which is well beyond the maximal membrane stretch a membrane can sustain. Therefore, for a samll constriction ring with $\Theta_0 = \pi/6$, the

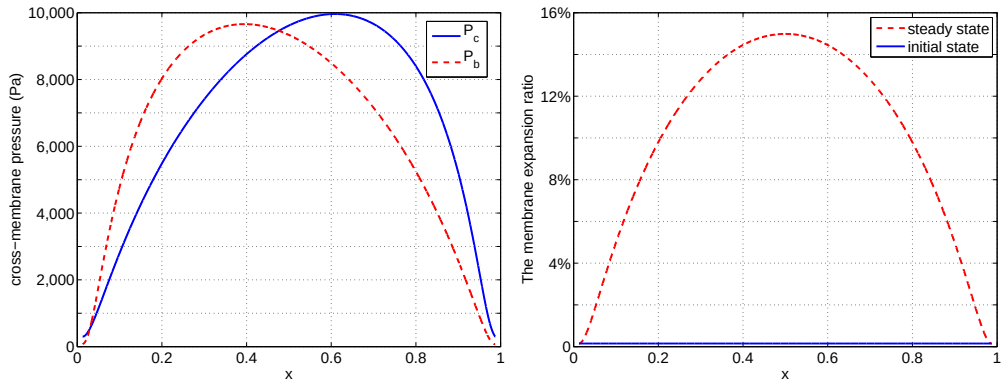

Figure 7.19: The cross-membrane pressure and membrane expansion corresponding to varying bleb volume. The membrane is assumed to obtain a uniform global tension, i.e. $T_b = T_c$. The size of constriction ring is $\Theta_0 = \pi/6$.

blebbing cell would rest at a stable steady state when the membrane tension is constrained to be uniform.

We next investigate the steady state of blebbing by varying the size of the constriction ring. As depicted in Figure 7.20, two steady states exist for the blebbing cell only when the size of the constriction ring is below a critical value, which is around 0.29π in our numerical setting. The stable equilibrium states occur at a smaller bleb size than the unstable one. Furthermore, the blebbing cell would maintain a higher cross-membrane pressure different at the stable equilibrium when the constriction ring is enlarging as illustrated in Figure 7.21. Similarly, it is observed that the extention of the plasma membrane is higher when the size constriction ring increases. In addition, at the stable equilibrium state the membrane is stretched below the lysis expansion ratio of 4%.

In summary, when the steady state tension of plasma membrane is globally uniform, the cell may rest at a stable equilibrium configuration when the constriction ring is smaller than a critical size. At this equilibrium state, the intracellular pressure is increased, compared to the initial state before the blebbing. The larger the constriction ring is, the higher the pressure difference will be at the equilibrium state. The membrane is stretching more than at the outset of blebbing.

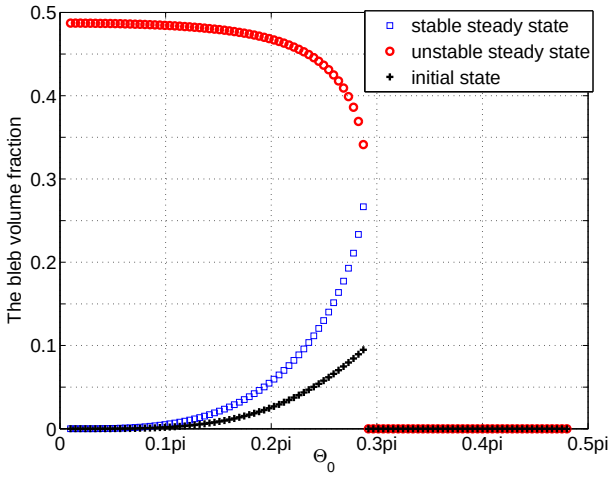

Figure 7.20: The volume fraction of bleb at the initial and steady state corresponding to various constriction ring, where $T_b = T_c$. The volume fraction of bleb at the initial state is plotted in triangle line, where those of stable and unstable equilibrium states are depicted in the square and circle lines, respectively. Note that there is no steady state when $\Theta_0 > 0.29\pi$.

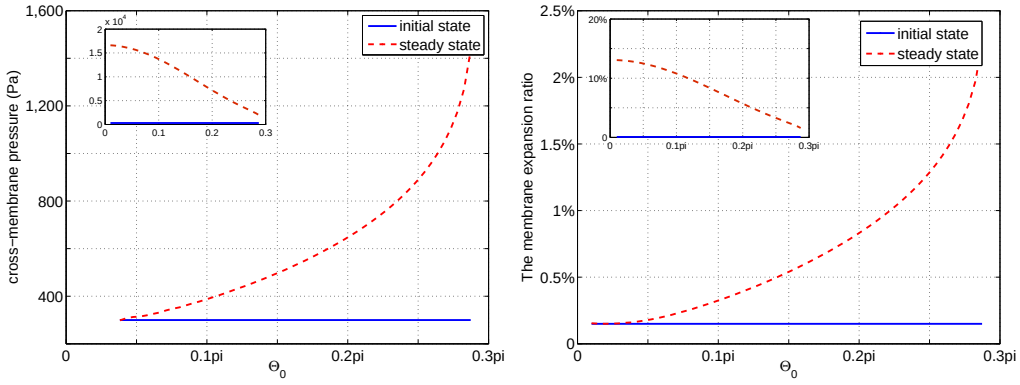

Figure 7.21: The intracellular pressure and membrane expansion rate at the stable equilibrium states corresponding to various constriction ring size Θ_0. The insets represent those for the unstable equilibrium state. Both the intracellular pressure and membrane stretching are higher at the unstable equilibrium state than at the stable one.

Chapter 8

Conclusions and future work

In a physiological environment, motile cells translocate themselves by extending various shapes of membrane protrusion. A thin layer of actin networks are formed transiently beneath the plasmic membrane with the aid of a variety of accessory proteins. The actin cortex, when powered by myosin motor molecules, contracts and deforms the associated membranes. The actin-driven cell motility received extensive investigation in the passing decades. It roughly falls into two classes: one is to apply the kinetic models to investigate the actin filament lengths in the presence of actin-binding proteins, and the other is aimed to understand the mechanical response of cells to growth and/or active contraction of actin structures as a continuum.

Many kinetic models were proposed to predict the filament lengths, and most focused on either the mean length or equilibrium length distribution. However, we have been able to investigate the temporal evolution of the filament length distribution by distinguishing individual filament by its length. We first proposed a deterministic kinetic model for pure filament polymerization, which includes only the modes of filament nucleation and endwise polymerization. Results indicate that the polymerization is favored over filament nucleation and produces an exponentially distributed lengths at equilibrium. The intermediate state is a slowly-evolved length redistribution, which is characterized as a Gaussian diffusive process. This diffusive

regime results from the slow random walking of actin monomers among filament ends. However, introducing uniform fragmentation on the filaments dramatically changes the redistribution regime while leaving the early growth stage intact. Our analysis predicts that the intermediate Gaussian-like distribution evolves to the steady state faster with fragmentation activities, and the higher fragmentation establishes the steady state sooner. Strikingly, fragmentation generate a universal Bessel-type equilibrium distribution, and the mean length is inversely related to a power of fragmentation rate. In solution, filament fragmentation is triggered by the binding of nucleotide-specific actin binding proteins. In the future, we can extend the kinetic model by assuming a non-uniform fragmentation, which depends both the nucleotide types and binding of severing proteins.

We recognize the polymerization of single filament is stochastic rather than deterministic, since F-actin associated with distinct nucleotides displays different kinetics. In a stochastic model, we incorporate the process of random nucleotide hydrolysis accompanying the F-actin polymerization. By implementing a modified Gillespie stochastic simulation algorithm [50], we are able, for the first time, to visualize the time evolution of nucleotide composition within filaments. On average, filaments exhibit an exponentially decaying profile of ATP/ADP-Pi emerges at the steady state. Furthermore, the intermitten binding of ADP- and ATP-actin at the barbed end could lead to a large length fluctuation as observed *in vitro*. The length fluctuation may jump by 30-45 folds when the monomer pool is around the barbed-end critical concentration of G-ATP. This has great potential implication in modelling the polymerization-driven force generation, where the mechanical load is shared only between filaments touching the obstacle surface. In the stochastic model, we also examined the effect of profilin proteins, which facilitate the nucleotide exchange on G-ADP and modify the barbed-end kinetics. We confirms that profilin diminishes the G-ADP accumulation in the solution, slowers filament elongation, and accelerates the filament treadmilling. In the future, with the framework of our stochastic model we would like to introduce the filament-nucleating proteins and filament cross-linker proteins to the filament polymerization. This would enable us to link the individual filament dynamics to the formation of higher dimensional actin network. In order to model the network dynamics,

one has to consider the spatial aspect of actin dynamics. This will introduce a spatial diffusion process into the model, whereby the actin monomers and other unbinded proteins diffuse in the solution but not for the network.

Cell blebbing is a typical membrane protrusion driven by acto-myosin contraction, and observed in many biological processes. It becomes more appreciated that blebbing can facilitate the cell to migrate through the complex extracellular matrix without massive membrane-substrate adhesion [73]. In our preliminary work, we recognize the major component processes occurring in the blebbing, and each individual component is examined. Before the blebbing, a thin layer of uniform actin cortex is formed and attached to membrane. The acto-myosin contraction creates surface tension both in the cortex and in associated membrane, and generates a high pressure difference across the membrane. At the outset of blebbing, cortex is locally destroyed or detached from the membrane; the intracellular pressure gradient thus propel the cortex-detached membrane to balloon outward. In the lab, it is discovered that the membrane ruptures at an expansion rate beyond 4%. This membrane property posed a constraint on the blebbing configuration, and results shows that as bleb expands, the constriction ring must enlarge accordingly. The steady state of blebs is analyzed by explicitly considering the cortex and membrane tensions. The cortex is assumed under constant tension, which might be related to the strength of actin-myosin contraction. The membrane tension is dynamically changing and depends only on the area expansion rate. The membrane flow is complicated in real blebbing, and has not been measured in experiments. We compared the blebbing equilibrium state in three pre-determined membrane flow simulations. If membrane is restricted within each domain, local destruction of membrane-cortex adhesion tends to deform the cell toward a stable equilibrium configuration, where the intracellular pressure is lowered, and the bleb membrane is under higher tension than the cell-body membrane. By prescribing a positive membrane flow from cell body to bleb, we instead observed an elevated cross-membrane pressure at equilibrium state. The relative tension for cell-body and bleb membranes is complicated and dependent of the flow rate. The third type of membrane flow we considered is that membrane crosses the constriction ring freely to maintain a uniform tension globally. Under this membrane flow, the

blebbing has two potential equilibrium states. One steady state is unstable, and the membrane expansion is well beyond the maximal rate 4%. The other equilibrium state is stable, and the resting pressure is higher than the initial one. The membrane is stretching more than at the outset of blebbing.

We analyzed the equilibrium state of blebbing mainly based on the Laplace law. The next step will be to consider the dynamics of cell blebbing. The materials of membrane, cortex and cytosol will be treated in the framework of continuum mechanics. The membrane can be modeled as a two-dimensional elastic or viscoelastic material as suggested in [79]. The layer of actin cortex is more like a thin shell of active material, which contracts in the presence of myosin motor molecules. In the future, the dynamics of individual and bulk filaments will be incorporated into the assembly and disassembly of actin cortex. In both cell body and bleb domains, the cytosol interacts directly with membrane, and is fit in the framework of fluid-structure interface. We realize the most difficult part of the model is the membrane-cortex adhesion. The membrane tearing off the cortex and dynamics of constriction ring remain open problems at this step.

Bibliography

[1] C. Starr and R. Taggart. Biology: the unity and diversity of life. *Wadsworth Publishing Company*, 1998.

[2] S.M. Rafelski and J.A. Theriot. Crawling toward a unified model of cell motility: spatial and temporal regulation of actin dynamics. *Annu Rev Biochem*, 73:209–239, 2004.

[3] D A Lauffenburger and A F Horwitz. Cell migration: a physically integrated molecular process. *Cell*, 84:359–69, 1996.

[4] T.D. Pollard, L. Blanchoin, and R.D. Mullins. Molecular mechanisms controlling actin filament dynamics in nonmuscle cells. *Annu Rev Biophys Biomol Struct*, 29:545–76, 2000.

[5] D Sept and J A McCammon. Thermodynamics and kinetics of actin filament nucleation. *Biophys J*, 81:667–674, 2001.

[6] Jonathon Howard. Mechanics of Motor Proteins and the Cytoskeleton. *Sinauer Associates, Inc.*, 2001.

[7] T.D. Pollard and G.G. Borisy. Cellular motility driven by assembly and disassembly of actin filaments. *Cell*, 112:453–465, 2003.

[8] I. Fujiwara, D. Vavylonis, and T.D. Pollard. Polymerization kinetics of adp- and adp-pi-actin determined by fluorescence microscopy. *PNAS*, 104(21):8827–8832, 2007.

[9] A. Berheim-Groswasser, S. Wiesner, R.M. Golsteyn, M.F. Carlier, and C. Sykes. The dynamics of actin-based motility depend on surface parameters. *Nature*, 417:308–311, 2002.

[10] T. P. Loisel, R. Boujemaa, D. Pantaloni, and M. F. Carlier. Reconstitution of actin-based motility of listeria and shigella using pure proteins. *Nature*, 401:613–616, 1999.

[11] S. Wiesner, E. Helfer, D. Didry, G. Ducouret, F. Lafuma, M.F. Carlier, and D. Pantaloni. A biomimetic motility assay provides insight into the mechanism of actin-based motility. *J Cell Biol*, 160(3):387–398, 2003.

[12] HG Othmer. Lecture notes.

[13] F. Oosawa and S. Asakura. *Thermodynamics of the Polymerization of Protein*. Academic Press, 1975.

[14] M Kawamura and K Karuyama. A further study of electron microscopic particle length of f-actin polymerized in vitro. *J Biochem*, 72:179–188, 1972.

[15] A. Wegner. Spontaneous fragmentation of actin filaments in physiological conditions. *Nature*, 286:266–267, 1982.

[16] HP Erickson. Co-operativity in protein-protein association, the structure and stability of the actin filament. *J Mol Biol*, 206:465–474, 1989.

[17] P. Olesen, J. Ferkinghoff-Borg, M.H. Jensen, and J. Mathiesen. Diffusion, fragmentation, and coagulation processes: analytic and numerical results. *Physical Review E*, 72:1–13, 2005.

[18] J. Roland, J. Berro, A. Michelot, L. Blanchoin, and J.L. Martiel. Stochastic severing of actin filaments by actin depolymerizing factor/cofilin controls the emergence of a steady dynamical regime. *Biophys J*, 94(6):2082–2094, 2008.

[19] D. Sept, J. Xu, T.D. Pollard, and J.A. McCammon. Annealing accounts for the length of actin filaments formed by spontaneous polymerization. *Biophys J*, 77:2911–2919, 1999.

[20] P. A. Janmey, J. X. Tang, and C. F. Schmidt. Actin filaments. *Biophysics Textbook Online*, 2001.

[21] E. Andrianantoandro, L. Blanchoin1, D. Sept, J. A. McCammon, and T. D. Pollard. Kinetic mechanism of end-to-end annealing of actin filaments. *J Mol Biol*, 312(4):721–730, 2001.

[22] D. Popp, A. Yamamoto, and Y. Maeda. Crowded surfaces change annealing dynamics of actin filaments. *J Mol Biol*, 368(2):365–374, 2007.

[23] D. Biron, E. Moses, I. Borukhov, and S. A. Safran. Inter-filament attractions narrow the length distribution of actin filaments. *Europhys Lett*, 73(3):464–470, 2006.

[24] I. Fujiwara, S. Takahashi, H. Tadakuma, and S. Ishiwata. Microscopic analysis of polymerization dynamics with individual actin filaments. *Nat Cell Biol*, 4:666–673, 2002.

[25] Jeffrey R. Kuhn and Thomas D. Pollard. Real-time measurements of actin filament polymerization by total internal reflection fluorescence microscopy. *Biophys J*, 88:1387–1402, 2005.

[26] D Vavylonis, Q Yang, and B O'Shaughnessy. Actin polymerization kinetics, cap structure, and fluctuations. *PNAS*, 102:8543–8548, 2005.

[27] EB Stukalin and AB Kolomeisky. ATP hydrolysis stimulates large length fluctuations in single actin filaments. *Biophys J*, 90:2673–85, 2006.

[28] J. Fass, C. Pak, J. Bamburg, and A. Mogilner. Stochastic simulation of actin dynamics reveals the role of annealing and fragmentation. *J Theor Biol*, 252(1):173–183, 2008.

[29] M. Bindschadler, E. A. Osborn, C. F. Dewey, and J. L. McGrath. A mechanistic model of the actin cycle. *Biophys J*, 86:2720–2739, 2004.

[30] J. Xu, W.H. Schwarz, J.A. Kas, T.P. Stossel, P.A. Janmey, and T.D. Pollard. Mechanical properties of actin filament networks depend on preparation, polymerization conditions, and storage of actin monomers. *Biophys J*, 74(5):2731–2740, 1998.

[31] J. Hu, A. Matzavinos, and H.G. Othmer. A theoretical approach to actin filament dynamics. *J Stat Phys*, 128:111–138, 2006.

[32] HG Othmer and LE Scriven. Instability and dynamic pattern in cellular networks. *J Theor Biol*, 32:507–537, 1971.

[33] T Kato. Perturbation Theory for Linear Operators. *Springer-Verlag*, 1966.

[34] L. Limozin, M. Barmann, and E. Sackmann. On the organization of self-assembled actin networks in giant vesicles. *Europ Phys J E*, 10:319–330, 2003.

[35] V DesMarais, M Ghosh, R Eddy, and J S Condeelis. Cofilin takes the lead. *J Cell Sci*, 118:19–26, 2005.

[36] W. Witke. The role of profilin complexes in cell motility and other cellular processes. *Trends Cell Biol*, 14:461–469, 2004.

[37] L Blanchoin, T D Pollard, and R D Mullins. Interactions of adf/cofilin, arp2/3 complex, capping protein and profilin in remodeling of branched actin filament networks. *Curr Biol*, 10(20):1273–82, 2000.

[38] H I Balcer, A L Goodman, A A Rodal, E Smith, J Kugler, J E Heuser, and B L Goode. Coordinated regulation of actin filament turnover by a high-molecular-weight srv2/cap complex, cofilin, profilin, and aip1. *Curr Biol*, 13(24):2159–69, 2003.

[39] S. Grenklo, M. Geese, U. Lindberg, J. Wehland, R. Karlsson, and A.S. Sechi. A crucial role for profilin-actin in the intracellular motility of listeria monocytogenes. *EMBO reports*, 4(5):523–529, 2003.

[40] T. Nyman, R. Pages, C.E. Schutt, R. Karlsson, and U. Lindberg. A cross-linked profilin-actin heterodimer interferes with elongation at the fast-growing end of f-actin. *J Biol Chem*, 227(18):15828–15833, 2002.

[41] F Kang, D L Purich, and F S Southwick. Profilin promotes barbed-end actin filament assembly without lowering the critical concentration. *J Biol Chem*, 274:36963–36972, 1999.

[42] M R. Bubb, E G Yarmola, B G Gibson, and F S Southwick. Depolymerization of actin filaments by profilin: effects of profilin on capping protein function. *J Biol Chem*, 278:24629–24635, 2003.

[43] E G Yarmola and M R Bubb. Effects of profilin and thymosin beta4 on the critical concentration of actin demonstrated in vitro and in cell extracts with a novel direct assay. *J Biol Chem*, 279:33519–33527, 2004.

[44] E. G. Yarmola and M. R. Bubb. Profilin: emerging concepts and lingering misconceptions. *Trends Biochem Sci.*, 31:197–205, 2006.

[45] L.A. Selden, H.J. Kinosian, J.E. Estes, and L.C. Gershman. Impact of profilin on actin-bound nucleotide exchange and actin polymerization dynamics. *Biochemistry*, 38(9):2769–2778, 1999.

[46] H J Kinosian, L A Selden, L C Gershman, and J E Estes. Actin filament barbed end elongation with nonmuscle mgatp-actin and mgadp-actin in the presence of profilin. *Biochemistry*, 41(21):6734–6743, 2002.

[47] L Blanchoin and T D Pollard. Hydrolysis of atp by polymerized actin depends on the bound divalent cation but not profilin. *Biochemistry*, 41:597–602, 2002.

[48] S Romero, D Didry, E Larquet, N Boisset, D Pantaloni, and M-F Carlier. How atp hydrolysis controls filament assembly from profilin-actin. *J Biol Chem*, 282(11):8435–8445, 2007.

[49] M. Lorenz, D. Popp, and K. C. Holmes. Refinement of the f-actin model against x-ray fiber diffraction data by the use of a directed mutation algorithm. *J Mol Biol*, 234:826–836, 1993.

[50] A. Matzavinos and H.G. Othmer. A stochastic analysis of actin polymerization in the presence of twinfilin and gelsolin. *J Theor Biol*, 249:723–736, 2007.

[51] A.E. Carlsson. Model of reduction of actin polymerization forces by atp hydrolysis. *Phys Biol*, 5(3), 2008.

[52] R Dickinson, L Caro, and D Purich. Force generation by cytoskeletal filament end-tracking proteins. *Biophys J*, 87:2838–2854, 2004.

[53] H J Kinosian, L A Selden, L C Gershman, and J E Estes. Interdependence of profilin, cation, and nucleotide binding to vertebrate non-muscle actin. *Biochemistry*, 39(43):13176–13188, 2000.

[54] Daniel T. Gillespie. A general method for numerically simulating the stochastic time evolution of coupled chemical reactions. *J Comput Phys.*, 22:403–434, 1976.

[55] Y. Marcy, J. prost, M.F. Carlier, and C. Sykes. Forces generated during actin-based propulsion: a direct measurement by micromanipulation. *PNAS*, 101(16):5992–5997, 2004.

[56] MF Carlier, D Pantaloni, and ED Korn. The effects of Mg2+ at the high-affinity and low-affinity sites on the polymerization of actin and associated ATP hydrolysis. *J Biol Chem*, 261:10785–10792, 1986.

[57] C. H. Lee, C. Gadgil, and H. G. Othmer. A stochastic analysis of first-order reaction networks. *Bull Math Biol*, 67:901–946, 2005.

[58] D.R. Cox and H.D. Miller. The theory of stochastic processes. *Wiley, New York*, 1965.

[59] S. Karlin and J. McGregor. Many server queueing processes with poisson input and exponential service times. *Pacific J Math*, 8:87–118, 1958.

[60] T.L. Hill. Linear aggregation theory in cell biology. *Springer-Verlag*, 1987.

[61] D. H. Boal. Mechanics of the cell. *Cambridge University Press*, 2002.

[62] P. Kunda, A.E. Pelling, T. Liu, and B. Baum. Moesin controls cortical rigidity, cell rounding, and spindle morphogenesis during mitosis. *Curr Biol*, 18:91–101, 2008.

[63] U. Seifert. Configurations of fluid membranes and vesicles. *Advances in Physics*, 46:13–137, 1997.

[64] U. Seifert, K. Berndl, and R. Lipowsky. Shape transformations of vesicles: Phase diagram for spontaneous- curvature and bilayer-coupling models. *Phys Rev A*, 44:1182–1202, 1991.

[65] Q. Du, C. Liu, and X. Wang. Simulating the deformation of vesicle membranes under elastic bending energy in three dimensions. *J Comput Phys*, 212:757–777, 2006.

[66] N. Kamiya. Cytoplasmic streaming in giant algal cells: A historical survey of experimental approaches. *J Plant Res*, 99:441–467, 1986.

[67] G.T. Charras. A short history of blebbing. *J Microsc*, 231:466–478, 2008.

[68] M.P. Sheetz and J. Dai. Modulation of membrane dynamics and cell motility by membrane tension. *Trends Cell Biol*, 6(3):85–89, 1996.

[69] N. Borghi and F. Brochard-Wyart. Tether extrusion from red blood cells: integral proteins unbinding from cytoskeleton. *Biophys J*, 93:1369–1379, 2007.

[70] J. Dai and M.P. Sheetz. Membrane tether formation from blebbing cells. *Biophys J*, 77:3363–3370, 1999.

[71] G.T. Charras, M. Coughlin, T.J. Mitchison, and L. Mahadevan. Life and times of a cellular bleb. *Biophys J*, 94:1836–1853, 2008.

[72] G. Majno and I. Joris. Cells, tissues, and diseases. *Oxford University Press*, 2004.

[73] G.T. Charras and E. Paluch. Blebs lead the way: how to migrate without lamellipodia. *Nat Rev Mol Cell Biol*, 9:730–736, 2008.

[74] O.T. Fackler and R. Grosse. Cell motility through plasma membrane blebbing. *J Cell Biol*, 181:879–884, 2008.

[75] H. Keller, P. Rentsch, and J. Hagmann. Differences in cortical actin structure and dynamics document that different types of blebs are formed by distinct mechanisms. *Exp Cell Res*, 277:161–172, 2002.

[76] G.T. Charras, J.C. Yarrow, M.A. Horton, L. Mahadevan, and T.J. Mitchison. Non-equilibration of hydrostatic pressure in blebbing cells. *Nature*, 435:365–369, 2005.

[77] G.T. Charras, C. Hu, M. Coughlin, and T.J. Mitchison. Reassembly of contractile actin cortex in cell blebs. *J Cell Biol*, 175:477–490, 2006.

[78] E. Paluch, M. Piel, J. Prost, M. Bornens, and C. Sykes. Cortical actomyosin breakage triggers shape oscillations in cells and cell fragments. *Biophys J*, 89:724–733, 2005.

[79] E.A. Evans and R. Skalak. Mechanics and thermodynamics of biomembranes. *CRC Press, Inc.*, 1980.

[80] P.M. Bendix, G.H. Koenderink, D. Cuvelier, Z. Dogic, B.N. Koeleman, W.M. Brieher, C.M. Field, L. Mahadevan, and D.A. Wietz. A quantitative analysis of contractility in active cytoskeletal protein networks. *Biophys J*, 94:3126–3136, 2008.

[81] T.J. Mitchison, G.T. Charras, and L. Mahadevan. Implications of a poroelastic cytoplasm for the dynamics of animal cell shape. *Semin Cell Dev Biol*, 19:215–223, 2008.